Bernhard Neumayer

# NMR techniques for the characterisation of tissue remodelling

**Ph.D. Thesis**

Graz University of Technology

Institute of Medical Engineering
Head: Univ.-Prof. Dipl-Ing. Dr.techn. Rudolf Stollberger

Supervisor: Univ.-Prof. Dipl-Ing. Dr.techn. Rudolf Stollberger

Graz, March 2018

## Statutory Declaration

I declare that I have authored this thesis independently, that I have not used other than the declared sources/resources, and that I have explicitly marked all material which has been quoted either literally or by content from the used sources.

Graz, _____ _____

Date Signature

## Eidesstattliche Erklärung[1]

Ich erkläre an Eides statt, dass ich die vorliegende Arbeit selbstständig verfasst, andere als die angegebenen Quellen/Hilfsmittel nicht benutzt, und die den benutzten Quellen wörtlich und inhaltlich entnommenen Stellen als solche kenntlich gemacht habe.

Graz, _____ _____

Datum Unterschrift

[1] Beschluss der Curricula-Kommission für Bachelor-, Master- und Diplomstudien vom 10.11.2008; Genehmigung des Senates am 1.12.2008

# Acknowledgements

At this point, I want to take the opportunity to express my gratitude to all the people who accompanied and supported me throughout the time of my PhD thesis.

First, I want to thank Prof. Rudolf Stollberger for giving me the opportunity to work in this interesting research area and for his guidance throughout the course of this thesis.
My sincerest gratitude goes to Prof. Eva Scheurer and Dr. Martin Urschler who both encouraged the advancement of this thesis and also played an important role in its completion.
I gratefully thank Alexandra Lipfert and Thomas Widek for all their support in imaging at the Institute of Medical Engineering and the Ludwig Boltzmann Institute for Clinical Forensic Imaging and Eva Amerstorfer for her continuing assistance.
My sincere thanks go to Lukas Schmuckermair who kept tabs on the language component of this thesis.
I want to thank all my colleagues at the Institute of Medical Engineering, especially my long-term PhD colleagues Florian Knoll, Clemens Diwoky, Manuel Freiberger, Andreas Petrovic, Peter Opriessnig, Christian Langkammer and Christoph Aigner for numerous MR and non-MR related discussions during working hours and – at least as often – after that. I also want to express my gratitude to my colleagues at the Ludwig Boltzmann Institute for Clinical Forensic Imaging, especially to Johannes Höller, Simone Leski and Naira Martínez Vera for many discussions directly and indirectly related to this thesis.
Very special thanks go to all of my friends who always were there when I needed to reflect on my thesis but also helped to get some distance to it at the right time. Also, I want to thank Angela and Hermann Göschl and the guys at S.K.U.S.I. for their recent support and boundless altruism in general.
Deep and sincere thanks go to my sisters Angela and Clara and to my parents Gerda and Matthias Neumayer for their life-long support without which this thesis would not have been possible.
Last but not least, I want to thank my wife Caroline for her love and support during all these years and my children Matilda and Elias who brighten up my day and my life.

# Abstract

Since its introduction into clinical routine, magnetic resonance imaging (MRI) has become an essential imaging technique due to a distinguished soft tissue contrast and the absence of ionizing radiation. The quantitative analysis of MRI data permits to study tissue composition and to investigate tissue changes over time. Thereby it can be based on endogenous MR parameters like relaxation times or proton density but also on quantities inherently influenced by these parameters, like image contrast information.

This thesis presents different approaches of quantitative analysis of magnetic resonance data to address currently unsolved problems in the field of medical and clinical forensic imaging. For this purpose biomarkers linked to tissue changes are measured or newly derived using magnetic resonance to characterize tissue changes.

A study on estimating the age of subcutaneous soft tissue haematomas was solely based on image contrast information, which was analysed to create a model and provide an objective age estimation.

For the observation of bone bridge formation, contrast enhanced MRI data of fractures in an animal model were investigated. This information was then put into a model to derive pharmacokinetic parameters which led to an early detection of bone bridge formation before it was visible in morphologic imaging data.

In a spectroscopy-based study the age-related conversion of red to yellow bone marrow is investigated. By applying a dedicated acquisition protocol, relaxation times of human lumbar vertebrae are derived and analysed for their reproducibility and for their correlation with age.

Ultimately, the contrast of epiphyseal gaps in MR images of the hand is investigated in a study on the potential acceleration of MRI for forensic age estimation. In this study image raw data is undersampled retrospectively. The reconstructed images are then analysed by radiologists and a fully automatic method to derive the limit of acceleration that can safely be applied to MR imaging for forensic age estimation without influencing the outcome.

Keywords: NMR, MRI, biomarkers, contrast agent, DCE

# Zusammenfassung

Die Magnetresonanztomographie (MRT) hat sich seit ihrer Einführung in die klinische Routine zu einem der wichtigsten medizinischen Bildgebungsverfahren entwickelt. Gründe dafür sind ihr herausragender Weichteilkontrast sowie die Tatsache, dass keine ionisierende Strahlung zum Einsatz kommt. Die quantitative Analyse von MRT-Daten erlaubt eine Untersuchung von Gewebszusammensetzungen beziehungsweise auch von Änderungen von Gewebe über die Zeit. Eine solche Analyse kann dabei sowohl auf der Auswertung endogener MR-Parameter wie Relaxationszeiten oder Protonendichte, als auch auf durch diese Parameter beeinflusster Größen wie Bildkontrast-Information basieren.

Im Rahmen dieser Arbeit werden unterschiedliche Ansätze für die quantitative Analyse von Magnetresonanz-Daten verwendet, um Fragestellungen aus dem Bereich der medizinischen und klinisch-forensischen Bildgebung zu beantworten. Zu diesem Zweck wurden für Gewebsveränderungen charakteristische Biomarker mittels Magnetresonanz dargestellt oder neu identifiziert.

Für eine Studie zur Altersschätzung von subkutanen Hämatomen wurde deren Kontrastverhalten untersucht. Dabei wurde der Kontrastverlauf über die Zeit analysiert und modelliert, um so eine objektive Altersschätzung zu ermöglichen.

Eine weitere Studie beschäftigte sich mit der Bildung von Knochenbrücken. Hierbei wurden für ein Tiermodell kontrastmittelunterstützte MRT-Daten erhoben, um pharmakokinetische Parameter zu ermitteln, die letztendlich eine Früherkennung einer Knochenbrückenbildung ermöglichten.

In einer MR-Spektroskopie-Studie wurde die altersabhängige Umwandlung von gelbem zu rotem Knochenmark untersucht. Mittels eines speziell dafür zusammengestellten Messprotokolls wurden Relaxationszeiten für menschliche Lendenwirbel ermittelt und auf Reproduzierbarkeit und Altersabhängigkeit hin untersucht.

In einer Studie über die potenzielle Beschleunigung der MR-Bildgebung für forensische Altersschätzung wurde der Kontrast von Wachstumsfugen in Handknochen untersucht. In dieser Studie wurden MR-Rohdaten retrospektiv unterabgetastet. Anschließend wurden die rekonstruierten Bilder von Radiologen und einer automatischen Methoden untersucht, um zu ermitteln

welcher Grad der Unterabtastung appliziert werden kann ohne das Ergebnis einer Altersschätzung zu verändern.

Keywords: NMR, MRI, biomarkers, contrast agent, DCE

# Contents

# List of Figures

# List of Tables

# Constants and Abbreviations

| | |
|---|---|
| AIF | arterial input function |
| CA | contrast agent |
| CAIPIRINHA | Controlled Aliasing In Parallel Imaging Results IN Higher Acceleration |
| CNR | contrast-to-noise ratio |
| DCE | dynamic contrast enhanced |
| DESPOT1 | driven-equilibrium single-pulse observation of T1 |
| DESPOT2 | driven-equilibrium single-pulse observation of $T_2$ |
| EES | extravascular extracelluar space |
| EPI | echo planar imaging |
| FF | fat fraction |
| FLASH | fast low angle shot |
| FXL | fast exchange limit |
| FXR | fast exchange regime |
| GF | generatig function |
| IR | inversion recovery |
| $K^{trans}$ | transfer coefficient |
| LL | Look-Locker |
| MRI | magnetic resonance imaging |
| MRS | magnetic resonance spectroscopy |
| NMR | nuclear magnetic resonance |
| PET | positron emission tomography |
| RF | radio frequency |
| RR(M) | reference region (model) |
| $S^2M$ | shutter speed model |
| SE | single-echo spin-echo |
| SNR | signal-to-noise ratio |
| $T_1$ | longitudinal relaxation time constant |
| $T_2$ | transverse relaxation time constant |
| TGV | total generalized variation |
| TSE | turbo spin echo |
| $v_e$ | extravascular extracellular volume |

# 1 Introduction

The effect of nuclear magnetic resonance (NMR) was discovered independently by Purcell, Torrey and Pound and Bloch, Hansen and Packard [1–3] in 1946. It was Lauterbur who first used NMR to create images using gradients [4] and provided the first *in vivo* image [5] in 1974.
Since its introduction into clinical routine in the early 1980s, magnetic resonance imaging (MRI) became one of the most important imaging techniques in diagnostic radiology. Compared to other tomographic imaging techniques, such as computed tomography, MRI bears the advantages of not using ionizing radiation and providing superior soft tissue contrast and high resolution images in any plane [6].

This thesis summarizes work dedicated to imaging and analysis of biomarkers related to tissue remodelling using magnetic resonance techniques. Chapter 1 of this thesis gives an overview of magnetic resonance parameters, their determination and their sensitivity to tissue alterations. Chapter 2 introduces publications written during the course of the thesis and Chapter 3 discusses how much progress the different publications achieved in advancing towards the initial goal.

In this chapter the basic principles of NMR are explained. The following sections cover the basic concepts of the origin and formation of the NMR signal. Furthermore, the concept of relaxation and approaches to determine the relaxation parameters will be discussed. The purpose of this chapter is to provide a basic knowledge of topics needed for the understanding of the main topics examined in this paper and will only focus on selected subjects. Therefore, the principles of MR signal acquisition, for example, will not be explained here.
The basic concepts of signal acquisition are extensively described by Haacke et al. [7] and Bernstein et al. give an elaborate overview of MRI pulse sequences [8]. The basic concepts of NMR, however with a strong focus on spectroscopy, are discussed in [9, 10] and for further information on relaxometry the reader is referred to [11].

## 1.1 Quantum Mechanical Description

In quantum mechanics, the angular momentum of elementary particles cannot take arbitrary values but is bound to quantization. The amplitude of $\hat{\vec{P}}$[2] is defined as [10]

$$P = \sqrt{s(s+1)}\,\hbar. \tag{1.1}$$

In equation (1.1) $s$ is the spin quantum number which can either be integer or half-integer and $\hbar$ is the reduced Planck's constant $\hbar = h/(2\pi)$. Equation (1.1) only defines the amplitude of the vector quantitiy $\hat{\vec{P}}$; the direction is specified by a second quantum number $m$ which can take $2s+1$ values given by $m = s, s-1, s-2, \ldots, -s$. The component of $\hat{\vec{P}}$ in z-direction is given by [10]

$$P_z = \hbar\, m. \tag{1.2}$$

Elementary particles have a magnetic moment $\mu$ which is related to the angular momentum by the *gyromagnetic moment* $\gamma$ [10]

$$\hat{\vec{\mu}} = \gamma \hat{\vec{P}}. \tag{1.3}$$

It is now straightforward that – since the angular momentum is quantized – the magnetic moment is quantized too. By analogy of equation (1.2) the z-component of the magnetic moment is given by [10]

$$\mu_z = \gamma\, \hbar\, m. \tag{1.4}$$

When placed in an external magnetic field $\vec{B}_0$, a particle obtains magnetic energy. In the quantum mechanical case the term for the angle between the external field and the magnetic moment is determined by $m$ [10]

$$E = -\mu_z\, B_0 = -\gamma\, \hbar\, m\, B_0 \tag{1.5}$$

Again, since $m$ is quantized, the energy levels can also only obtain certain values. For protons (hydrogen), the spin quantum number is $s = 1/2$ which only permits two orientations: $m = 1/2$ and $m = -1/2$. For brevity and since this thesis will only focus on spins with spin quantum number $s = 1/2$, they will be designated as spins-1/2 from here on.
The energy difference between the two possible states of spins-1/2 is [10]

$$\Delta E = -\gamma\, \hbar\, B_0 \tag{1.6}$$

This energy defines the frequency of the oscillating magnetic field that is required for the resonance phenomenon in NMR. The magnetic field is applied perpendicular to $\mu_z$ and requires a frequency, so that [10]

$$E = -h\, \nu_0. \tag{1.7}$$

[2] The notation with the ˆ symbol is used to mark quantum mechanical operators.

Eventually, when combining equations (1.6) and (1.7), this leads to the *Larmor equation* [10]

$$\nu = -\left(\frac{\gamma}{2\pi}\right) B_0. \tag{1.8}$$

This resonance condition can only be explained using the quantum mechanic description.

A classical description, on the other hand, is more useful when explaining the interaction between excitation pulses and the magnetization vector. In fact, while proton spin is a quantum effect, magnetic resonance is not, as it is accurately described by classical mechanics, which was already pointed out by Feynman et al. in 1957 [12].

## 1.2 Relaxation

Once a sample is put in a static magnetic field and left undisturbed for a sufficient amount of time, all coherences disappear, the spin populations obey the *Boltzmann distribution* and the sample reaches its thermal equilibrium [7, 10]

$$M_0 = \frac{\rho_0 \hbar^2 \gamma^2}{4 k_B T} B_0, \tag{1.9}$$

where $\rho_0$ is the number of spins in the sample, $\hbar$ is the reduced Planck's constant $\hbar = h/(2\pi)$, $\gamma$ is the *gyromagnetic moment*, $k_B = 1.380\,66 \times 10^{-23}\,\mathrm{J\,K^{-1}}$ is the *Boltzmann constant* and $T$ is the absolute temperature.
Radiofrequency (RF) pulses can affect this equilibrium by changing population distributions and/or creating coherences, e.g.: a $\pi$ (or 180°) pulse inverts the population distribution (i.e. the magnetization in z-direction), whereas a $\pi/2$ (or 90°) pulse equalizes the spin state populations and generates coherences[3]. Relaxation is the process of returning to the thermal equilibrium and can be divided into two types: the return of the spin populations back to their Boltzmann distribution and the loss of potentially existing coherences. The return to the Boltzmann distribution is called the *spin–lattice*[4] or *longitudinal relaxation*, the loss of coherence is termed *spin–spin* or *transverse relaxation*. For isolated spins-1/2 these two processes are described by two constants, namely the *longitudinal relaxation time constant* $T_1$ and the *transverse relaxation time constant* $T_2$. Different tissues will exhibit

[3] The tip angle of an RF pulse is determined by the duration of the RF pulse, $\tau_{RF}$, and the nutation frequency $\omega_1$: $\beta_{RF} = \omega_1 \tau_{RF}$. The nutation frequency is defined by $B_1$, the peak value of the oscillating RF field, and $\theta_{RF}$, the angle between the main magnetic field and the RF field: $\omega_1 = |\frac{1}{2}\gamma B_1 \sin\theta_{RF}|$.

[4] The term 'lattice' is a remainder of the times when NMR research focused on solids, investigating the interaction between nuclear spins and the crystal lattice. Liquids and gases do not possess a lattice; however, the term was kept.

different values for the time constants leading to a difference in signal intensity and thereby to tissue contrast.
Relaxation involves the thermal motion of molecules and fluctuating local magnetic fields. A comprehensive analysis of the relaxation processes requires a thorough investigation of random field relaxation, correlation times and spectral densities. This chapter presents the results of these considerations.

### 1.2.1 Longitudinal Relaxation

The longitudinal relaxation is the result of a change of spin populations which in turn is determined by transition probabilities. The reason for the relaxation lies within the movement of the water molecules carrying the water protons. While the nuclear spins are almost completely independent of the molecular movement in its immediate environment, the molecular environment does influence the nuclear magnets. This is due to the fact that molecules consist of electrons and nuclei which all contribute to the local magnetic field experienced by each spin. And these contributions do fluctuate rapidly as a result of the molecular motion. This "wobbling" of the local magnetic fields interrupts the isotropy of the nuclear spin polarization and the spins will – with a certain probability – favour an orientation with low magnetic energy. This finally leads to a slightly increased orientation of magnetic moments parallel to the external magnetic field and thereby to a longitudinal relaxation as well as the thermal equilibrium magnetization.

The time dependence of the longitudinal magnetization is generally described by [7]

$$M_z(t) = M_0 \left(1 - e^{\frac{t}{T_1}}\right), \tag{1.10}$$

in which $T_1$ is the longitudinal relaxation time.

### 1.2.2 Transverse Relaxation

As the name implies, transverse relaxation occurs for transverse magnetization, i.e. perpendicular to the field. However, there is no net transverse magnetization for a sample in a magnetic field since the magnetization distribution is cylindrically symmetrical. As mentioned above, the application of a $\pi/2$ pulse equalizes spin state populations and creates coherences, which is tantamount with a rotation of the net magnetization to the transverse plane.

The source of transverse relaxation is the decay of the coherences created in the transverse plane towards zero. This is caused by varying local magnetic

fields and the thereby created loss of synchronization. The speed of the loss of synchronization is related to the frequency of the field fluctuations which can be described by the *autocorrelation function* [9]

$$\begin{aligned} \mathbb{G}_x(\tau) &= \langle B_x(t) B_x(t+\tau) \rangle \\ \mathbb{G}_y(\tau) &= \langle B_y(t) B_y(t+\tau) \rangle \end{aligned} \tag{1.11}$$

for fluctuations of the local magnetic fields in x-direction and y-direction, respectively.
The autocorrelation function decreases fast (with respect to $\tau$) for rapid fluctuations and slow for a slowly fluctuating field. Due to its appearance $\mathbb{G}$ is assumed to be exponential, which seems qualitatively correct, "but is difficult to justify on the basis of a deeper theory" [9, Chapter 20.3.1]. This lead to the phenomenological assumption of an exponential decay of the magnetization in the x-y plane

$$M_{xy}(t) \propto M_0 \cdot e^{-\frac{t}{T_2}} \tag{1.12}$$

with the transverse relaxation time $T_2$. The signal decay as described by equation (1.12), however, is only valid for isolated spins-1/2. For real NMR experiments the transverse magnetization is influenced by spin interactions as well as imperfections of the measuring system.
The main influence of the measuring system on the transverse relaxation is a decrease of the apparent $T_2$ due to inhomogeneities of the main magnetic field. The relation between $T_2$ and the apparent, shorter $T_2^*$ is [10]

$$M_{xy}(t) = M_{xy}(0) e^{-\frac{t}{T_2}} \int_r e^{+i\gamma \Delta B_0(r) t} dr = M_{xy}(0) e^{-\frac{t}{T_2^*}}, \tag{1.13}$$

in which $\Delta B_0(r)$ are the inhomogeneities of the main magnetic field.
While the transverse relaxation is irreversible, the consequences of inhomogeneities can be revoked by applying a $\pi$ pulse, which reverses the additional loss of coherence caused by the inhomogeneities. This is done in spin-echo acquisitions which thereby are not prone to inhomogeneities of the main magnetic field[5].
Spin interactions can occur intramolecular or intermolecular. Intramolecular spin interactions comprise chemical shift, spin–rotation, dipole–dipole, and J-coupling as well as quadrupole coupling, which, however, has no effect on spins-1/2. Intermolecular spin interactions only occur via chemical shift and dipole–dipole and quadrupole coupling. The influence of each interaction on the actual measurement depends on the acquisition approach, the time scale of the measurement, and the tissue under investigation. A detailed analysis of these effects demands cumbersome calculations of the spin Hamiltonian and will not be investigated any further in this thesis.

[5] However, due to the additional pulse and the duration needed for the echo formation, the acquisition time of spin-echo measurements is increased compared to gradient echo acquisitions.

### 1.2.3 The Bloch Equations

The Bloch equations, named after Felix Bloch, are a set of three differential equations describing the three components of the magnetization vector [13]. Defining $\Omega^0$ as the frequency offset, and setting the thermal equilibrium magnetization of the z-value $M_z = 1$, they can be written [9]

$$\frac{d}{dt}\begin{pmatrix} M_x \\ M_y \\ M_z \end{pmatrix} = \begin{pmatrix} 0 & -\Omega^0 & \omega_1 \sin\phi \\ \Omega^0 & 0 & -\omega_1 \cos\phi \\ -\omega_1 \sin\phi & \omega_1 \cos\phi & 0 \end{pmatrix} \begin{pmatrix} M_x \\ M_y \\ M_z \end{pmatrix} - \begin{pmatrix} \frac{M_x}{T_2} \\ \frac{M_y}{T_2} \\ \frac{M_z - 1}{T_1} \end{pmatrix}. \tag{1.14}$$

In equation (1.14) $\omega_1$ is the nutation frequency of the irradiation pulse and $\phi$ is the phase of the RF field. The Bloch equations thereby allow for a simultaneous observation of relaxation and resonance offset effects as well as modulations due to RF pulses.

## 1.3 Relaxometry

Relaxometry is the determination of relaxation parameters. Since these parameters provide a quantitative measure of an investigated sample, their determination is of special interest in order to categorize tissue properties or to detect changes over time in a quantitative and reproducible manner. The following chapters will give an overview of currently applied sequences and alternative, faster approaches for the determination of $T_1$ and $T_2$ and discuss their advantages and disadvantages compared to the gold standard method.

### 1.3.1 Longitudinal Relaxation Time

The longitudinal relaxation time $T_1$ is an intrinsic biophysical property of tissue and linked to macromolecule concentration, water binding and water content. Furthermore, it may change upon pathology: for example, $T_1$ increases in oedema around tumors or decreases at the rim of active multiple sclerosis lesions. Therefore, an accurate determination of $T_1$ is important for tissue characterization and also – and this will become more obvious in chapter 1.4 – for contrast agent uptake studies [11].

The gold standard experiment for the measurement of $T_1$ is an inversion recovery (IR) sequence being the most accurate technique [14]. For this

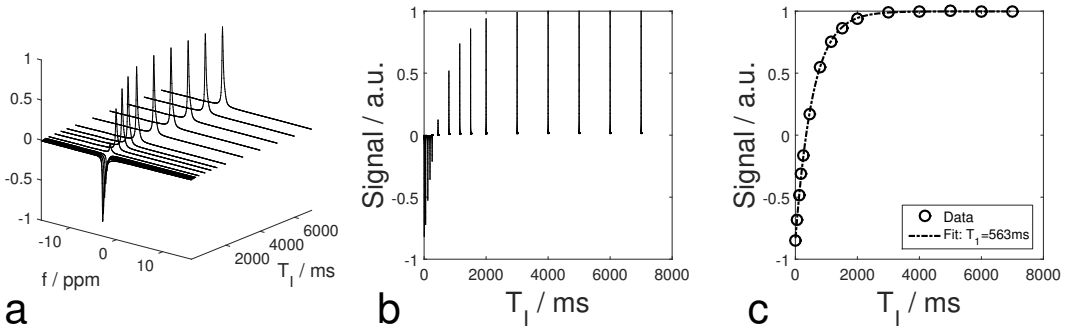


Figure 1.1: $T_1$ determination applying an inversion recovery approach. (a) MR spectra acquired after magnetization inversion using different inversion times $T_I$, (b) side view of the spectra visualizing the exponential nature of the signal recovery, and (c) determination of $T_1$ applying a mono-exponential fit to the data.

approach the longitudinal magnetization in equilibrium state is inverted applying a $\pi$ pulse. Following the inversion, the magnetization will recover exponentially and after an inversion time $T_I$ a $\pi/2$ is applied to tilt the magnetization to the transverse plane for read-out. Repeating the measurement for different values of $T_I$, the signal intensity $S$ can then be described as a function of $T_I$ according to equation (1.15)

$$S(T_I) = S_0 \left(1 - 2 \cdot e^{-\frac{T_I}{T_1}}\right), \tag{1.15}$$

where $S_0$ is the signal which would be generated by the magnetization in equilibrium state. This simple description only applies to a spectroscopic acquisition, i.e. in the absence of any imaging gradients. This is, however, adequate for the explanation of the principle which is additionally shown in figure 1.1. For the determination of $T_1$ in figure 1.1c the factor 2 in equation (1.15) was replaced with an additional fitting parameter to account for incomplete inversions due to inhomogeneities of the irradiating field (B1). The reliability of this extension, i.e. of three-parameter fits applied to IR data, was shown in 1984 by Ejchart et al. [15].
Since an IR experiment starts with the longitudinal magnetization in its equilibrium state, a repetition for different inversion times demands a considerable amount of time between the acquisitions to allow the magnetization to return to its starting point. Generally, it is assumed that a repetition time of at least $T_R \gg 5T_1$ is required for a correct determination of $T_1$; regarding equation (1.15) a repetition time of $5T_1$ is tantamount with a return to 98.65 % of its initial value. Depending on the value of $T_1$ this can lead to long acquisition times even for spectroscopic measurements. For imaging experiments not implementing accelerated imaging each measurement has to be repeated for each image line, too, which usually makes this approach useless for *in vivo* applications.
This demands a decrease of imaging time, which can be achieved 1) by using rapid imaging techniques after an initial magnetization preparation like in

echo planar imaging (EPI) or turbo spin echo (TSE) acquisitions, 2) with in-plane acceleration methods like parallel imaging [16–18] or compressed sensing [19–21], respectively, through-plane acceleration using simultaneous multi-slice excitation [22–24] or 3) by applying a different method of measuring the longitudinal relaxation time. This section will address commonly used approaches of measuring $T_1$.

A straightforward approach to decreasing the time demanded by an IR acquisition is to reduce $T_R$ to a value much shorter than $5T_1$. This prevents the longitudinal magnetization from returning to its initial value and forces it into a *steady-state* [25]. The acquired data must then be modelled by equation 1.16.

$$S(T_I) = S_0 \left(1 - 2 \cdot e^{-\frac{T_I}{T_1}} + e^{-\frac{T_R}{T_1}}\right) \tag{1.16}$$

A different approach – but still a sort of inversion recovery technique – is to sample the recovery of the longitudinal magnetization using multiple low-angle readout pulses after an initial inversion. Such techniques are termed Look-Locker (LL) sequences to refer to the original developers of this approach [26].
The multiple readout pulses of LL sequences lead to a speed-up of the signal recovery, which causes an apparent longitudinal relaxation time $T_1^*$ depending on the interval between the read-out pulses and the flip angle applied for read-out [27, 28]. While this change in signal behavior can be described mathematically for the original approach, things get more complex when a further speed-up is attempted, e.g. using a snapshot FLASH (Fast Low Angle SHot) imaging module which introduces additional RF pulses [29–31]. Also, LL sequences are sensitive to RF pulse errors in general due to the multiply applied read-out pulses.
Generally, whenever variations of the irradiating field are expected to significantly influence the outcome of the estimates for $T_1$ a mapping of $B_1$ will be required. Such methods can be based on image magnitude [32–36] or image phase [37–39]. Thereby, the simplest to implement is the double-angle method [32, 33] while techniques based on the Bloch–Siegert shift are least time demanding [38, 40–42]. A comprehensive comparison between currently applied methods for $B_1$ mapping can be found in a recent review by Pohmann and Scheffler [43].

A different technique for the determination of $T_1$ uses the inherent $T_1$ weighting of stimulated echoes [44, 45]. This approach suffers from a reduced dynamic range and low SNR [14], which can, for example, be tackled by combining initial spin echo and later stimulated echo information [46]. Another way to combine spin echo and stimulated echo information is to determine the phase between these two signals acquired as a composite echo, which was shown to be related to $T_1$ [47, 48].

For fast imaging applications, the inherent $T_1$ weighting of FLASH sequences can be exploited to derive $T_1$ values. The signal acquired with a FLASH sequence is defined as [8]

$$S = S_0 \frac{1 - e^{-\frac{T_R}{T_1}}}{1 - \cos\theta \cdot e^{-\frac{T_R}{T_1}}} \sin\theta \cdot e^{-\frac{T_E}{T_2^*}} \tag{1.17}$$

with flip angle $\theta$. For short echo times $T_E \ll T_2^*$ the term $e^{-\frac{T_E}{T_2^*}}$ can be ignored and $T_1$ can then be determined by varying either $T_R$ or $\theta$ [49, 50]. A well-known technique using this approach is DESPOT1 (Driven-Equilibrium Single-Pulse Observation of $T_1$) [51–53], which uses at least two different flip angles for the determination of $T_1$. The drawback of these methods is that the scanning parameters have to be optimized for a certain range of $T_1$; the accuracy of a quantitative analysis therefore decreases with increasing distance to this pre-defined range.
For DCE measurements the method proposed by Hittmair et al. [54] is especially suitable. For this technique a proton density weighted image is acquired prior to contrast-enhanced measurement using a low flip angle. At low flip angles the proton density images can be acquired using short repetition times which allows for an acceptable acquisition time. Furthermore, the low flip angles allow for additional simplifications and the relaxation time can then be calculated using equation (1.18) [55]

$$T_1(t) = -\frac{T_{R,DCE}}{\ln\left(\frac{S_{REF}\sin(\theta_{DCE}) - S_{DCE}(t)\sin(\theta_{REF})}{S_{REF}\sin(\theta_{DCE}) - S_{DCE}(t)\sin(\theta_{REF})\cos(\theta_{DCE})}\right)}, \tag{1.18}$$

where the subscripts $_{REF}$ and $_{DCE}$ denote reference scan and dynamic scan, respectively.

The purpose of this chapter is to provide a useful collection of methods to determine the longitudinal relaxation time. However, the overview given in this chapter is not complete and a more thorough collection of methods can, for example, be found in the extensive overview of methods for the determination of $T_1$ by Kingsley [56] comprising 283 references. Additionally, recent publications provide comparisons of clinically applied $T_1$ mapping methods and their accuracy and precision [57, 58].

### 1.3.2 Transverse Relaxation Time

The quantification of the transverse relaxation time is not utilized for the investigations described in this thesis. However, for the sake of completeness, the principle for the determination of $T_2$ is briefly described in this chapter. The numerous influences on the acquired transverse signal discussed in

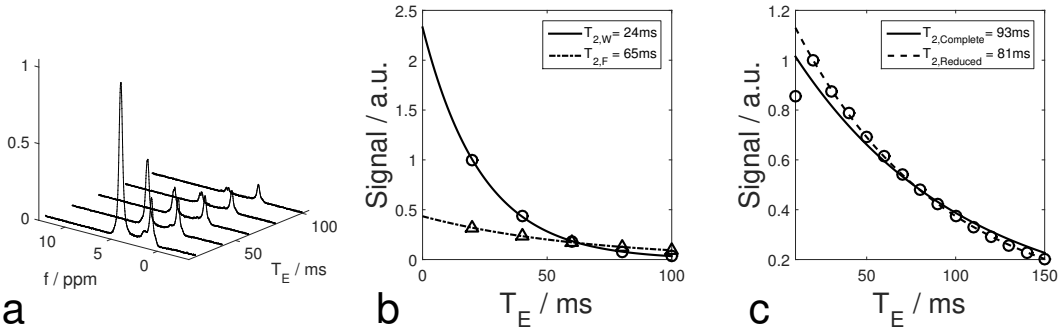


Figure 1.2: $T_2$ determination applying a single-echo and a multiple-echo approach. (a) MR spectra of a human lumbar vertebrae acquired for different echo times $T_E$, (b) determination of $T_2$ applying a mono-exponential fit to the separated data of the spectra, and (c) MSE data affected by stimulated echoes. Discarding the first echo leaves an exponential decay; however, affected by stimulated echoes.

chapter 1.2.2 must be considered when analysing the acquired signal in order to derive $T_2$ values. The gold standard for a $T_2$ quantification is an acquisition of a single-echo spin-echo (SE) signal, which is repeated for different values of the echo time $T_E$. This is visualized in figure 1.2 using *in vivo* spectroscopy data acquired in a lumbar vertebra.
Figure 1.2a shows spectral data with a water peak at approximately 4.7 ppm and a fat signal consisting of several peaks with its maximum at approximately 1.3 ppm ($CH_2$ peak). Figure 1.2b shows the results of separate mono-exponential fits to water and fat data. The results show a pronounced difference between $T_2$ of the two different compartments and emphasize the importance of the determination of the transverse relaxation time for quantitative analyses [59]. A calculation of the fat content of the investigated vertebra using the water and fat signal values of the spectrum with the shortest echo time would yield 24.19 % but a determination of $T_2$ and using extrapolated signal values of the acquired data results in a fat content of 15.72 %. This difference is caused by the large difference in $T_2$ between water and fat and shows that a correct determination of $T_2$ demands a spectroscopic analysis as soon as multiple frequency components are present.
As expected, a repeated acquisition of single-echo spin-echo measurements demands a notable amount of time. Therefore, multiple-echo spin-echo (MSE) sequences are usually applied to achieve faster acquisitions. Using a short echo spacing an MSE approach even bears the advantage of suppressing J-coupling, chemical exchange, and diffusion effects [60–62] compared to an SE acquisition. However, due to a repeated application of $\pi$ pulses, MSE acquisitions are subject to $B_1$ inhomogeneities causing incorrect flip angles and thereby leading to stimulated echoes adding up to the spin-echo signal. This leads to results as shown in figure 1.2c where the second data point shows a higher amplitude than the first echo due to an overlapped stimulated echo. In fact, all remaining data points will be influenced by stimulated echoes.

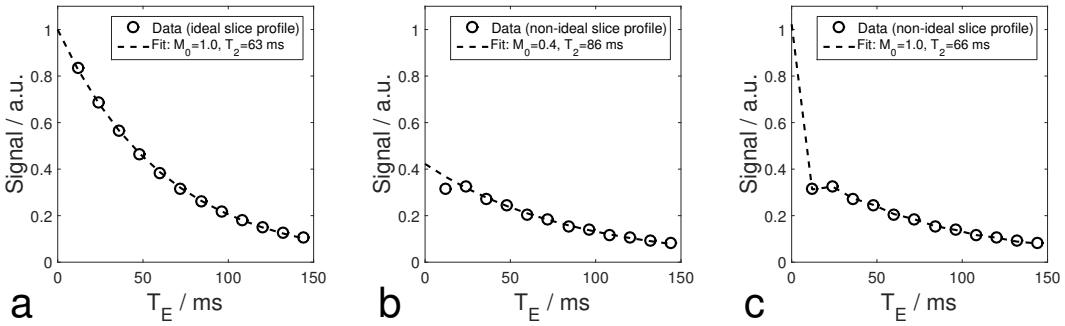


Figure 1.3: $T_2$ determination using the generating function approach proposed by Petrovic et al. [72]. Signal propagation was simulated for $M_0$=1, $T_2$=60 ms adding 5 % noise and (a) an ideal slice profile applying the standard method, (b) a non-ideal slice profile applying the standard method, and (c) a non-ideal slice profile applying the GF approach to determine $T_2$.

The influences of $B_1$ and $B_0$ inhomogeneities on the determination of $T_2$ are extensively discussed elsewhere [63–67]. The influence of the stimulated echoes can either be addressed by introducing a phase shift between the initial RF pulse and the subsequent refocusing pulses [68] or using composite refocusing pulses [69]. Phase cycling can be applied to cancel spurious echoes but it will also double the acquisition time [70].
A different approach to improve $T_2$ mapping is to calculate the actual signal behavior of a multiple-echo spin-echo sequence analytically instead of suppressing signal propagations. The approach proposed by Lukzen and Savelov [71] allows for an analytical calculation of the MSE signal for arbitrary flip angles and is termed the generating function (GF) formalism. This approach can be further enhanced by including non-ideal slice profiles into the equation [72] (see figure 1.3).
Alternatively, the DESPOT technique [51–53] mentioned in chapter 1.3.1 can also be applied for $T_2$ determination and is then termed DESPOT2 (Driven-Equilibrium Single-Pulse Observation of $T_2$). The results of this approach can be further enhanced by a reduction of artifacts by means of incorporating RF phase-cycling [73].

The usual analysis of MSE data includes discarding the value of the first echo and fitting an exponential curve to the remaining data as shown in figure 1.2c. It can be seen that a fit to the reduced data set seems more plausible than a fit to the complete data; however, it was shown that this method does not provide sufficiently accurate results [72].
Figure 1.3 illustrates the limited applicability of the standard method. As long as the slice profile is perfectly rectangular this approach will provide accurate results (figure 1.3a); however, as soon as the slice profile deviates from a rectangular shape, the standard method will overestimate $T_2$ and underestimate $M_0$ (figure 1.3b). The GF approach on the other hand uses the complete data set provided by the measurement and – with the slice profile

provided as additional parameter – is able to model the signal loss due to the non-ideal irradiation (figure 1.3c). This will provide better estimates for $M_0$ and $T_2$ (i.e. closer to the real values) which will usually differ considerably from the results provided by the standard method. Therefore, a comparison of quantitative $T_2$ data found in the literature must always be performed with caution.

### 1.3.3 Multi-Exponential Relaxation

The data in figures 1.2a and 1.2b show a potential problem for relaxometry of MR data. Different relaxation times of multiple signal compartments can be identified using MR spectroscopy; however, they will lead to multi-exponential signal curves for imaging experiments where usually[6] only the sum of all signals in a voxel can be acquired.
Multi-exponential signal relaxation is the result of different tissues being present in a voxel (see e.g. [11, Chapter 6.8] for details) but the extent of the effect additionally depends on exchange speed between involved compartments. The influence of the exchange speed becomes especially important when pronounced changes of relaxation times can occur, which is the case for dynamic contrast enhanced measurements (see section 1.4). The influence of the water exchange on MR measurements utilizing contrast agents is discussed in section 1.4.4.
Multi-exponential relaxation occurs for longitudinal and transverse magnetization alike. With sufficient temporal resolution relaxation times of multiple compartments can be extracted by applying multi-exponential fits to measured data; however, care must be taken that relaxation times of all involved compartments are covered by the applied measurement parameters. The results of multi-exponential fits can then be used to derive additional parameters like, for example, the density of cell populations [74].

## 1.4 Dynamic Contrast Enhanced Magnetic Resonance Imaging

MR contrast agents can be used to observe angiogenesis and microvasculature of a certain tissue of interest. This can be achieved by determining physiological characteristics like perfusion, blood volume, permeability of blood vessels and the fraction of the interstitium or extravascular extracellular space (EES). The determination of these parameters requires a

[6] Unless additonal precautions like, for example, a saturation of off-resonant signals are taken.

consecutive acquisition of MR images to observe the contrast agent concentration as the contrast agent enters and exits the tissue of interest. The acquisition technique for this observation of the contrast agent behaviour over time is termed dynamic contrast enhanced MRI, or DCE-MRI. DCE-MRI allows to characterize angiogenesis and microvasculature and therefore is mainly used to gain information on tumour microvessel structure and function [75–77, and references therein]; however, it is not restricted to the analysis of tumourous tissue but can, for example, also be applied to injured growth plates as shown in [78].

For clinical applications mostly gadolinium-based contrast agents are used. These lead to changes of the tissue's native $T_1$, $T_2$, and $T_2^*$ as the CA passes and their effect is exploited by using an appropriate weighting. One can either exploit the decrease in $T_1$ leading to an increase in signal intensity or the change in $T_2$ or $T_2^*$ which produces a decrease of the signal intensity as CA concentration rises. In analogy to the previous section, only $T_1$ effects will be addressed here. Furthermore, the following descriptions only apply to contrast agents that are small enough to extravasate out of a blood vessel but still large enough to remain extracellular, also termed type 2 agents [79]. The exploitation of the $T_1$ effect of an administered contrast agent requires the acquisition of a series of $T_1$-weighted images to observe the kinetics of the CA. To derive the aforementioned physiological parameters from the acquired data it will be necessary to know the current concentration of contrast agent in a blood vessel preferably near the tissue of interest. An appropriate model, that allows the interpretation of the extravasation of contrast agent from the vessel into the tissue under observation, is also essential.
The most commonly used model was developed by Kety in 1951, which was originally developed for the case of breathing an inert gas [80]. This model divides the body into two compartments: the blood/plasma and the tissue space. In an attempt to establish an international standard for MR applications Tofts et al. unified existing studies introducing a new standard set of quantity names in an excellent review which in fact became a standard work for DCE-MRI [81]. Therefore, the model is usually referred to as the Kety/Tofts model or simply the Tofts model.

### 1.4.1 Tofts Model

The standardized terms proposed by Tofts et al. are the transfer constant from plasma space to tissue space, $K^{\text{trans}}$, the volume of the EES, $v_e$, and the rate constant $k_{ep}$, which equals

$$k_{ep} = \frac{K^{\text{trans}}}{v_e}. \tag{1.19}$$

The determination of $K^{\text{trans}}$ and $v_e$ requires knowledge of the absolute values of tracer concentration while the rate constant can be derived from the shape of the tracer concentration versus time [81].
The definition of the transfer constant depends on the composition of the tissue of interest. In tissue with high permeability[7] the transfer constant equals [81]

$$K^{\text{trans}} = F\rho(1 - \text{Hct}), \tag{1.20}$$

in a situation with low permeability[8] it is [81]

$$K^{\text{trans}} = PS\rho. \tag{1.21}$$

In equation (1.20) $F$ is the flow (or perfusion) of whole blood per unit mass of tissue in $\text{ml}\,\text{g}^{-1}\,\text{min}^{-1}$, $\rho$ is the density of the tissue in $\text{g}\,\text{ml}^{-1}$, and Hct is the hematocrit ($1 - \text{Hct}$ therefore is tantamount with the plasma space). In equation (1.21) $P$ is the total permeability of the capillary wall in $\text{cm}\,\text{min}^{-1}$, $S$ is the surface area per unit mass of tissue in $\text{cm}^2\,\text{g}^{-1}$, and since it often occurs in this combination, the product $PS$ is known as the permeability surface area product per unit mass of tissue in $\text{ml}\,\text{min}^{-1}\,\text{g}^{-1}$. Due to their appearances equations (1.20) and (1.21) are often termed the flow-limited and PS-limited case, respectively.
In addition to these two cases, a mixed flow and PS case exists. For the mixed model $K^{\text{trans}}$ is defined as the product of the flow-limited case and the *extraction fraction* $E$ [82]:

$$K^{\text{trans}} = EF\rho(1 - \text{Hct}) \text{ with } E = 1 - e^{-\frac{PS}{F(1-\text{Hct})}} \tag{1.22}$$

The different definitions of $K^{\text{trans}}$ for different tissue compositions will also lead to different interpretations of this constant. Depending on the situation, the transfer constant can reflect a formation of new vasculature, an increase in size of existing vessels or a rise of vessel permeability. For tumours, for example, the leaky vasculature is best described by PS-limited or mixed models [83].

Regardless of the tissue composition or the permeability situation, all models show the form of the *Generalized Kinetic Model* defined by Tofts et al. which relates the tissue concentration $C_t$ to the arterial plasma concentration $C_p$ according to equation (1.23) [81].

$$\frac{d}{dt}C_t(t) = K^{\text{trans}} \cdot C_P(t) - k_{\text{ep}} \cdot C_t(t) \tag{1.23}$$

The arterial plasma concentration is usually referred to as the AIF, the tissue concentration is also known as the *tissue residue function*, and introducing an

[7] High permeability is defined as $PS \gg F$, where $PS$ is the permeability surface area product per unit mass of tissue and F is the perfusion of whole blood per unit mass.
[8] Low permeability is defined as $PS \ll F$

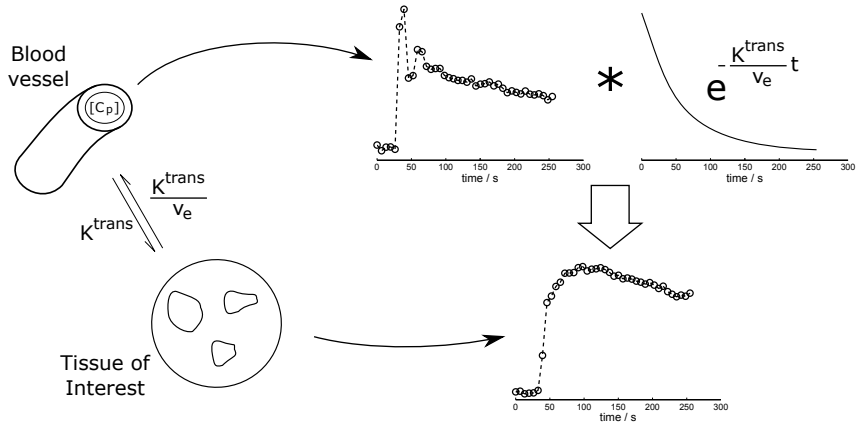


Figure 1.4: Tissue uptake for DCE measurements. The exchange of contrast agent between a vessel and the tissue of interest results in a convolution (marked by the asterisk) of the arterial input function and the characteristic residue function of the tissue described by $K^{\text{trans}}$ and $v_e$ (see equations (1.24)–(1.25)).

*impulse residue function* [84, 85]

$$R = e^{-k_{ep}t} \tag{1.24}$$

the solution of equation (1.23), with initial conditions $C_p$=$C_t$=0 at $t$=0, is

$$C_t(T) = K^{\text{trans}} \int_0^T R(T-t) \cdot C_p(t) dt. \tag{1.25}$$

This means, that the tissue residue function is the result of a convolution of the arterial input function and the impulse residue function, which is depicted in figure 1.4.

### 1.4.2 Arterial Input Function

Figure 1.4 shows real data for the arterial input function and a tissue of interest. Since the contrast agent is usually administered as bolus injection – most reliable estimations for $K^{\text{trans}}$ are expected for fast and high volume injections [86] – the typical form of an AIF comprises a short but high concentration peak, a second increase due to a second pass of the contrast agent, which is not always visible, and a washout period. It is a critical task to capture the peak of the AIF since only a certain temporal resolution can be accomplished. Therefore, it is also important to optimize the timing between injection and image acquisition.
The most accurate method to determine the AIF is to simultaneously acquire image data and draw arterial blood samples [87, 88]. However, this method requires considerable additional efforts for taking the blood samples and is

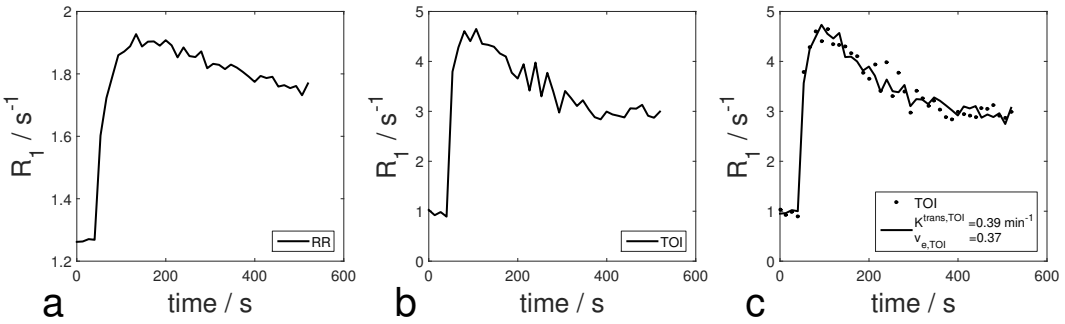


Figure 1.5: Example for a reference region model analysis. (a) Course of $R_1$ in the reference region (RR), (b) course of $R_1$ in the region of interest (ROI), and (c) result of the fit using RR and ROI data as input for a reference region model.

far from being non-invasive. Furthermore, for preclinical studies the blood volume to be drawn is strongly limited and the duration of the AIF is even shorter due to the increased heart rate of small animals.

Although the temporal resolution of the measurement results in figure 1.4 is acceptably high with 6.5 s, only 3 data points define the peak of the first pass. Thus, it cannot be assured that the peak value could be acquired. Additionally, as mentioned above, this peak is even shorter for small animals, and, as a consequence, a large vessel is needed in the field of view to determine the AIF.
These problems can be addressed in different ways. The temporal resolution can be increased at the expense of resolution and/or SNR; however, in many cases this is not acceptable. Approaches without decreasing the resolution are to use population-based averaged arterial input functions [89–94] or model-based AIFs [95]. But an obvious drawback of these methods is that inter-individual variations between subjects cannot be covered. A different approach is to measure the contrast agent concentration in a tissue with constant and known pharmacokinetic parameters. If the transfer constant of the reference tissue is low enough, the course of the CA concentration can be acquired with a significantly lower temporal resolution allowing for an acquisition of higher resolved image data. Such models are referred to as *reference region models*.

### 1.4.3 Reference Region Model

Several studies implemented reference region models [96–98] which were thoroughly investigated for their reliability and repeatability [99–101].

The basic principle of a reference region model is quite simple. Recalling equation (1.23) of Tofts' generalized kinetic model and defining it for a reference region (RR) and for a tissue of interest (TOI) leads to equations (1.26),

in which $k_{ep,RR}$ and $k_{ep,TOI}$ equal $K^{trans,RR}/v_{e,RR}$ and $K^{trans,TOI}/v_{e,TOI}$ and $C_{RR}(t)$ and $C_{TOI}(t)$ are the tissue residue functions of the reference region and the tissue of interest, respectively.

$$\begin{aligned}\frac{d}{dt}C_{RR}(t) &= K^{trans,RR}\cdot C_P(t) - k_{ep,RR}\cdot C_{RR}(t)\\ \frac{d}{dt}C_{TOI}(t) &= K^{trans,TOI}\cdot C_P(t) - k_{ep,TOI}\cdot C_{TOI}(t)\end{aligned} \tag{1.26}$$

Eliminating $C_P(t)$, the contrast agent concentration in the tissue of interest can be described by the contrast agent concentration in the reference region according to equation (1.27).

$$\begin{aligned}C_{TOI}(T) = R\cdot C_{RR}(T) + R\cdot(k_{ep,RR} - k_{ep,TOI})\\ \cdot\int_0^T C_{RR}(t)\cdot e^{-k_{ep,RR}}\cdot(T-t)dt\end{aligned} \tag{1.27}$$

The relationship between measured $R_1$, the tissue's inherent $R_{10}$ and contrast agent concentration is

$$R_1 = R_{10} + r_1\cdot[CA]. \tag{1.28}$$

Defining an additional constant

$$K = \frac{K^{trans,TOI}}{K^{trans,RR}} \tag{1.29}$$

leads to the definition of the relaxation rate of the tissue of interest, $R_{1,TOI}(T)$, according to equation (1.30).

$$\begin{aligned}R_{1,TOI}(T) = {} & K\cdot(R_{1,RR}(T) - R_{10,RR}(T)) + K\cdot\left[k_{ep,RR} - k_{ep,TOI}\right]\\ & \cdot\int_0^T\left[\left(R_{1,RR}(T) - R_{10,RR}(T)\right)e^{-k_{ep,TOI}(T-t)}dt\right] + R_{10,TOI}\end{aligned} \tag{1.30}$$

As mentioned above, the validity of equation (1.30) strongly depends on the reliability of the assumed pharmacokinetic parameters of the reference region. Several studies showed that skeletal muscle is a valid reference region with values of $K^{trans,RR} = 0.045\,min^{-1}$ and $v_{e,RR} = 0.08$ [102–105]. Still, it must be ensured that a constant muscle region is chosen. A region as large as possible will also increase the SNR and thereby the reliability of the results.

Using a reference region model allows for an analysis as shown in figure 1.5, where the data of a reference region (figure 1.5a) is fitted to the data of a region of interest (figure 1.5b). The resulting curve and the identified

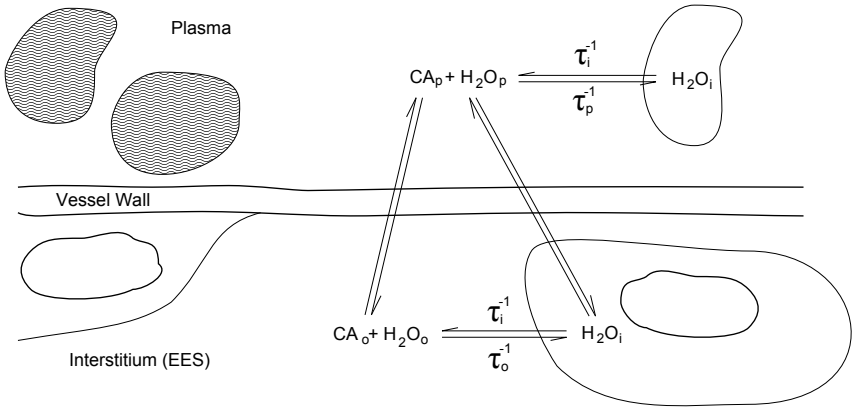


Figure 1.6: Tissue compartments involved in water exchange. The letters i, o, and p denote inside the cell, outside the cell, and plasma, respectively. The quantity $\tau$ is the lifetime of a water molecule in the respective compartment [106, 107].

pharmacokinetic parameters are shown in figure 1.5c. In this example the tissue of interest is an artificially created physeal lesion in a rat model and the reference region is a skeletal muscle near to the lesion. The influence of the SNR of the reference region signal becomes obvious since the RR data is directly put into equation (1.30) and not modeled.

### 1.4.4 Transcytolemmal Water Exchange

Since MR contrast agents influence water molecules in close proximity, the water diffusion between different compartments can potentially influence the effect of the contrast agent. Here, four compartments have to be taken into account, namely the intra- and extracellular compartments of the intra- and the extravascular space, as depicted in figure 1.6. Many studies have shown that the water lifetime within erythrocyte suspensions is rather short[9] ($\tau_i \sim 10\,\text{ms}$), which further led to the assumption that the exchange via the cell membrane (*cytolemma*, thus transcytolemmal water exchange) is fast and usually can be neglected [103, 108].
However, to evaluate the influence of water exchange, the exchange speed must always be seen relative to the relaxation times of the involved compartments, which change considerably upon administration of contrast agents [109, 110]. Landis et al. further investigated the exchange kinetics in skeletal muscle [103] and the influence on the determination of the contrast agent concentration [107]. Depending on the assumptions on the water exchange between specific compartments, different models are applied. Additionally to the Tofts model so-called shutter speed models ($S^2M$)

[9] The internal lifetime for a erythrocyte is defined as $\tau_i^{-1} = P \cdot A/V$ where $P$ is the the permeability, $A$ the surface and $V$ the volume. Erythrocytes possess high permeability and a small volume, thus the fast exchange.

were proposed [111, 112]. However, the necessity of an inclusion of water exchange effects in clinically relevant DCE-MRI acquisitions is still a controversial issue [102, 104, 113].

The linear relationship between relaxation rate and CA concentration

$$R_1 = R_{10} + r_1 \cdot [\mathrm{CA}]. \tag{1.31}$$

demands an infinitely fast water exchange and is termed the fast exchange limit (FXL). A more concrete definition of the exchange speed uses the *relaxographic NMR shutter speed*[10]. This definition compares the exchange speed

$$\tau^{-1} = \frac{1}{\tau_i} + \frac{1}{\tau_o} \tag{1.32}$$

to the relaxographic shutter speed

$$v_s = |R_{1i} - R_{1o}| \tag{1.33}$$

and the FXL is defined as

$$\tau^{-1} \gg v_s. \tag{1.34}$$

A deviation from this requirement causes a non-linear relationship between relaxation rate and CA concentration (the relaxivity is partially "quenched" [115]). This will lead to an underestimation of the transfer constant and the EES if an infinitely fast exchange is assumed for the analysis of the acquired data.
The slow exchange regime, where the water exchange will cause a strong non-linear behaviour, is defined as

$$\tau^{-1} < v_s. \tag{1.35}$$

Additionally, a fast exchange regime (FXR) is defined as

$$\tau^{-1} > v_s \tag{1.36}$$

for a range in which the exchange rate is still fast compared to the shutter speed but non-linearities are already present in the relationship between relaxation rate and CA concentration [102, 103]. In equations (1.32)–(1.36) the letters $i$ and $o$ denote inside and outside the cell, respectively and $\tau$ is the lifetime of a water molecule in the respective compartment.
While details can be found elsewhere [107, 111, 113], the non-linear relationship between the relaxation rate and the contrast agent concentration due

[10] The term *relaxography* describes the determination of the distribution of relaxation times and was introduced by Labadie et al. [114].

to transcytolemmal water exchange is shown in equation (1.37).

$$\begin{aligned} R_1 = \frac{1}{2}\left[2 \cdot R_{1i} + r_1 \cdot C(t) + \left(R_{1o} - R_{1i} + \frac{1}{\tau_i}\right) \cdot \frac{f_w}{v_e}\right] \\ - \frac{1}{2}\left\{\left[\frac{2}{\tau_i} - r_1 \cdot C(t) - \left(R_{1o} - R_{1i} + \frac{1}{\tau_i}\right) \cdot \frac{f_w}{v_e}\right]^2 \right. \\ \left. + 4 \cdot \frac{\frac{f_w}{v_e} - 1}{\tau_i^2}\right\}^{\frac{1}{2}} \end{aligned} \tag{1.37}$$

## 1.5 MR Properties of Biological Tissue

This thesis is dedicated to measuring and determining biomarkers for tissue remodelling. Therefore, it is necessary to investigate the influence of tissue properties on MR parameters respectively on the acquired MR signal.

Proton density and relaxation times are sensitive to a wide range of water interactions such as the water content [116, 117], macromolecular concentration [118], structure of macromolecules [119] or bulk organization of the extracellular matrix [120, 121].
Many of these influences can be shown by a rather simple experiment using raw and cooked eggs and MR imaging as well as MR spectroscopy as performed by Jayasundar et al. [122]. Assuming the short correlation-time limit, where the rotational correlation time is much shorter than the Larmor period $2\pi/\omega$, the dipole–dipole mechanism can be simplified to [122]

$$\frac{1}{T_1^{DD}} = B\tau_R + \frac{C}{D}, \tag{1.38}$$

where $B$ and $C$ are constants and $D$ is the self diffusion constant. For free water $\tau_R$ is short and $D$ is large compared to bound water. This will lead to a reduced $T_1$ in a cooked egg compared to a raw egg due to water molecules being bound to macromolecules, which increases $\tau_R$ and decreases $D$.

$T_2$ and $\tau_R$ are related by [122]

$$\frac{1}{T_2} \simeq K\frac{\tau_R}{1 + \omega^2\tau_R^2} \tag{1.39}$$

with $K$ being a constant. Equation (1.39) explains a shortening of $T_2$ of water in a boiled egg compared to a raw egg. Above that, faster $T_2$ relaxation can be observed in the egg yolk, where water protons are bound to macromolecules causing a lengthening of $\tau_R$.

| Tissue | 3 T | | 1.5 T | |
|---|---|---|---|---|
| | $T_2$ (ms) | $T_1$ (ms) | $T_2$ (ms) | $T_1$ (ms) |
| Liver | 42±3 | 812±64 | 46±6 | 576±30 |
| Skeletal muscle | 50±4 | 1412±13 | 44±6 | 1008±20 |
| Heart | 47±11 | 1471±31 | 40±6 | 1030±34 |
| Kidney | 56±4 | 1194±27 | 55±3 | 690±30 |
| White matter | 69±3 | 1084±45 | 72±4 | 884±50 |
| Gray matter | 99±7 | 1820±114 | 95±8 | 1124±50 |
| Optic nerve | 78±5 | 1083±39 | 77±9 | 815±30 |
| Spinal cord | 78±2 | 993±47 | 74±6 | 745±37 |
| Blood | 275±50 | 1932±85 | 290±30 | 1441±120 |

Table 1.1: $T_2$ and $T_1$ relaxation times at 3 T and 1.5 T, measured at 37 °C [123].

As a result of the numerous influences on water interactions, different biological tissues exhibit different MR parameters [123] (see table 1.1) and tissue remodelling due to, for example, ageing or healing can be anticipated to lead to measurable changes of these parameters.

In fact, for intracranial haemorrhage contrast changes have been reported to be dependent on the age of the respective trauma. These contrast changes are connected to oxidative denaturation of haemoglobin molecules [124]. This led to the classification of intracranial haemorrhages into the stages *hyperacute* (<24h), *acute* (1–3d), *early subacute* (>3d), *late subacute* (>7d) and *chronic* (>14d) connected to the presence of intracellular oxyhaemoglobin, intracellular deoxyhaemoglobin, intracellular methaemoglobin, extracellular methaemoglobin and extracellular haemichromes, respectively [125]. Corresponding changes of $T_1$ and $T_2$ of blood over time were shown in *in vitro* studies [126–129].
Contrast information can also be exploited for the topic of age estimation in living persons. The age of children and adolescents can be derived from the bone age, which can be estimated from the fusion stages of the epiphyseal gap located between epiphysis and metaphysis of the hand bones [130–132]. In $T_1$-weighted MR images, these epiphyseal gaps can be identified as hyperintensities and can further be used for age estimation [133, 134]. Such an estimation can also be performed automatically using regression random forests [135, 136] or deep learning methods [137].
A well-known tissue transformation is the conversion of red to yellow bone marrow with age [138]. The conversion process changes the ratio of water and fat compartments, which makes the fat fraction of bones a potential biomarker for age – visible in both MR imaging [139–143] and MR spectroscopy [144–148].

## 1.6 Aim of This Thesis

The aim of this thesis is the quantitative analysis of magnetic resonance data to image, measure or derive biomarkers linked to tissue remodelling. The distinguished soft tissue contrast provided by MR imaging as well as the sensitivity of MR parameters to tissues changes form a fundamental basis for such an analysis. Modelling the behaviour of the MR signal over time therefore can be anticipated to provide information on tissue composition and allow to derive biomarkers connected to formation of newly formed structures or changes induced by remodelling of tissue.

The first approach is based on the analysis of contrast information to infer information on haematoma resorption by using contrast information as an estimator for the healing process. For this study artificial soft tissue haematomas were created in 20 healthy volunteers. To estimate the age of the haematomas, data of standard commercially available image sequences were investigated over a time period of two weeks. Contrast changes were determined and a model describing these changes over time for the different sequences was created. This model was then used to estimate the age of the haematomas.

The formation of bone bridges was documented in a longitudinal animal study acquiring highly-resolved MR images as well as DCE data of physeal lesions. To analyse the vascularity in the injured areas, pharmacokinetic parameters were obtained by applying a reference region model (RRM) [97] to the acquired DCE data. The imaging results and the change of the pharmacokinetic parameters over time were compared to histologic and gene expression analyses, which gave an insight into the creation process of bone bridges.

The reproducibility of relaxometry in human lumbar vertebrae was investigated in a spectroscopy study. For this study 46 healthy volunteers underwent three consecutive multi-$T_E$/multi-$T_R$ MRS protocols. Following spectral fitting, relaxation times $T_1$ and $T_2$ as well as the fat fraction of lumbar vertebrae L2 and L3 were calculated from the MRS data. Ultimately, the data was analysed for reproducibility and their correlations with age.

Finally, the potential reduction of the acquisition time for MRI-based age estimation has been investigated in a simulation study. For 15 healthy volunteers MR raw data was retrospectively undersampled with varying acceleration factors. To evaluate the quality of the reconstructed images, two radiologists as well as an automatic method performed age estimation for original images and the images reconstructed from undersampled data. The difference between the estimates was evaluated to determine the maximum acceleration that can be applied to MR acquisitions while still maintaining adequate image quality for age estimation.

## 1.7 Outline of This Thesis

Chapter 1 of this thesis covers the basic theoretical principles of NMR. The requirements for the formation of a magnetic resonance signal as well as relaxation effects are described and thereby the origin of contrast in MR images will be explained. The information provided by this chapter will be sufficient for the comprehension of the topic of this thesis but it is not exhaustive. The interested reader is provided with further reading suggestions.

Chapter 2 includes short summaries and the final versions of the publications written in the course of this thesis.

The discussion in chapter 3 summarizes the results of this thesis. It provides conclusions for each publication relevant for this thesis and evaluates the scientific significance of the outcome.

# 2 Studies

## 2.1 Age Determination of Soft Tissue Hematomas

[149] Neumayer B., Hassler E., Petrovic A., Widek T., Ogris K., and Scheurer E. "Age Determination of Soft Tissue Hematomas." In: *NMR Biomed.* 27.11 (Sept. 2014), pp. 1397–1402. DOI: 10.1002/nbm.3202

### 2.1.1 Summary

In clinical forensic medicine it is often important to determine the time of the origin of soft tissue injuries. The age of a haematoma can define or, at least, set limits to the period of time in which an accident or a crime including blunt force took place. This leads to an inclusion or exclusion of possible offenders as well as a differentiation of multiple events. The current standard for the evaluation of haematoma age is the visual assessment of external haematoma colour [150, 151]. However, this method is unreliable as the results show a great inter-observer variability as well as a poor accuracy compared to the real age of haematomas [152, 153]. Additionally, it was shown that a reliable determination is hindered by the individually varying colour perception of examiners [154].
Novel attempts for haematoma age estimation aiming at a greater reliability and objectivity were proposed and mainly focused on the visible properties of bruises [147, 155–157] investigating the spectral information of the light reflected from a haematoma.

To estimate the age of soft tissue haematomas, MR images of artificially created haematomas acquired with standard commercially available image sequences were investigated over two weeks for 20 healthy volunteers. The contrast between haematoma and muscle tissue was determined and a model was created to describe the contrast changes over time for the different sequences. This model was then used to estimate the age of the haematomas to show the potential of MRI for haematoma age estimation due to its excellent contrast in soft tissues.

### 2.1.2 Author Contribution

In this study Bernhard Neumayer's contribution comprised the analysis of the available data and the development of an adequate signal model. Furthermore, he implemented the model and tested its applicability using cross-validation. Finally, the manuscript was mainly written by Bernhard Neumayer.

### 2.1.3 Additional Relevant Publications

[158] Hassler E. M., Ogris K., Petrovic A., Neumayer B., Widek T., Yen K., and Scheurer E. "Contrast of artificial subcutaneous hematomas in MRI over time." In: *Int J Legal Med* 129.2 (Nov. 2014), pp. 317–324. DOI: 10.1007/s00414-014-1124-8

In this radiological study the signal model implemented for the primary publication was applied to generally estimate a transition from hyperintensity to hypointensity for subcutaneous hematomas compared to muscle tissue. Furthermore, the difference between compact and diffuse hematomas was analyzed.

Research article

NMR IN BIOMEDICINE

Received: 2 July 2013, Revised: 29 July 2014, Accepted: 13 August 2014, Published online in Wiley Online Library: 11 September 2014

(wileyonlinelibrary.com) DOI: 10.1002/nbm.3202

# Age determination of soft tissue hematomas

**Bernhard Neumayer[a], Eva Hassler[a,b], Andreas Petrovic[a], Thomas Widek[a], Kathrin Ogris[a,c] and Eva Scheurer[a,c]***

**In clinical forensic medicine, the estimation of the age of injuries such as externally visible subcutaneous hematomas is important for the reconstruction of violent events, particularly to include or exclude potential suspects. Since the estimation of the time of origin based on external inspection is unreliable, the aim of this study was to use contrast in MRI to develop an easy-to-use model for hematoma age estimation.**

**In a longitudinal study, artificially created subcutaneous hematomas were repetitively imaged using MRI over a period of two weeks. The hemorrhages were created by injecting autologous blood into the subcutaneous tissue of the thigh in 20 healthy volunteers. For MRI, standard commercially available sequences, namely proton-density-weighted, $T_2$-weighted and inversion recovery sequences, were used. The hematomas' MRI data were analyzed regarding their contrast behavior using the most suitable sequences to derive a model allowing an objective estimation of the age of soft tissue hematomas.**

**The Michelson contrast between hematoma and muscle in the proton-density-weighted sequence showed an exponentially decreasing behavior with a dynamic range of 0.6 and a maximum standard deviation of 0.1. The contrast of the inversion recovery sequences showed increasing characteristics and was hypointense for $T_I$ = 200ms and hyperintense for $T_I$ =1000ms. These sequences were used to create a contrast model. The cross-validation of the model finally yielded limits of agreement for hematoma age determination (corresponding to ±1.96 SD) of ±38.7h during the first three days and ±54 h for the entire investigation period.**

**The developed model provides lookup tables which allow for the estimation of a hematoma's age given a single contrast measurement applicable by a radiologist or a forensic physician. This is a first step towards an accurate and objective dating method for subcutaneous hematomas, which will be particularly useful in child abuse. Copyright © 2014 John Wiley & Sons, Ltd.**

**Keywords:** hematoma; age estimation; forensic; soft tissue; subcutaneous; contrast; MRI

## INTRODUCTION

In clinical forensic medicine, it is often important to determine the time of origin of soft tissue injuries. The age of a hematoma can define or at least set limits on the period of time during which an accident or a crime including blunt force, e.g. in child abuse, took place. This leads to an inclusion or exclusion of possible offenders, as well as a differentiation of multiple events.

The current standard for the evaluation of hematoma age is the visual assessment of external hematoma color (1,2). However, this method is unreliable, as the results show great interobserver variability as well as poor accuracy compared with the real age of hematomas (3,4). Additionally, it was shown that a reliable determination is hindered by the individually varying color perception of examiners (5).

Novel attempts at hematoma age estimation, aiming at a greater reliability and objectivity, were proposed and focused mainly on the visible properties of bruises (6–9), investigating the spectral information of the light reflected from the hematoma. However, while most authors concentrated on general principles, only Randeberg et al. (7) attempted to estimate the exact age of bruises in living subjects using reflectance spectroscopy. The authors concluded that they could achieve an accuracy of 1d for recent hematomas but the variance of the age of the investigated hematomas did not allow for a statistical analysis. Also, the method required an assumption on or the additional determination of skin parameters. Furthermore, as a main limitation, the subjects investigated in that study were not healthy and took anticoagulants.

In MR images, hematomas can be identified well using an adequate contrast and initial results showed that the contrast of hematomas in MRI could be used to obtain objective information on hematomas (10,11) without the determination or assumption of additional parameters, such as skin thickness

* *Correspondence to: E. Scheurer, Ludwig Boltzmann Institute for Clinical Forensic Imaging, Universitätsplatz 4, A-8010 Graz, Austria. E-mail: Eva.Scheurer@cfi.lbg.ac.at*

a *B. Neumayer, E. Hassler, A. Petrovic, T. Widek, K. Ogris, E. Scheurer Ludwig Boltzmann Institute for Clinical Forensic Imaging, Universitätsplatz 4, A-8010, Graz, Austria*

b *E. Hassler Department of Radiology, Division of General Radiological Diagnostics, Medical University of Graz, Auenbruggerplatz 9, A-8036, Graz, Austria*

c *K. Ogris, E. Scheurer Medical University Graz, Department of Forensic Medicine, Universitätsplatz 4, A-8010, Graz, Austria*

**Abbreviations used:** *$C_M$, Michelson contrast; CPC, cloth pin coil; ctHb, hemoglobin concentration; FHHb, fraction of deoxyhemoglobin; $FO_2Hb$, fraction of oxyhemoglobin; Hct, blood hematocrit; IR, inversion recovery; LOOM, leave-one-out method; MetHb, methemoglobin fraction; PDw, proton-density-weighted; SNR, signal-to-noise ratio; $sO_2$, oxygen saturation; SPAIR, spatially adiabatic inversion recovery; T2w, $T_2$-weighted; TF, turbo factor; TSE, turbo spin echo.*

or scattering properties, as required by reflectance spectroscopy methods. This approach bears the advantage that it can be easily applied by radiologists or forensic physicians without additional calculations, as needed for volume determinations or relaxometry.

Temporal changes of brain hemorrhages have been extensively investigated using MRI (12–15, and references therein). Based on these data, the age of an intracranial hemorrhage can be estimated. However, MR studies on extracranial hematomas are scarce (16–19) and none have focused on the determination of hematoma age.

The aim of this study was to model the temporal behavior of different MRI contrast parameters in artificial subcutaneous hemorrhages over time, in order to establish an objective method for the estimation of the age of soft tissue hematomas.

## MATERIALS AND METHODS

### Subjects

In 20 healthy volunteers (11 female, 9 male, mean age ± standard deviation [SD]: 26.84 ± 3.53y) without coagulation disorders or medication influencing blood clotting, 10ml of venous blood was drawn from the cubital vein after an initial basic MRI scan of the thigh. Four milliliter of the blood was immediately injected into the subcutaneous tissue of their thigh and 6ml blood was used for blood gas analysis (pH, oxygen saturation [$sO_2$], blood hematocrit [Hct], fraction of deoxyhemoglobin [FHHb], methemoglobin fraction [MetHb], fraction of oxyhemoglobin [$FO_2Hb$]), hemoglobin concentration [ctHb]). The study was approved by the local medical university ethics committee and written informed consent was obtained from all subjects.

### MRI

The artificial hematomas of the thigh were examined repetitively with MRI in oblique orientation, i.e. directly after the injection and after 3h, 1d, 3d, 1week and 2 weeks, on a clinical 3T scanner (TimTrio, Siemens AG, Germany) using a superficial receive-only cloth pin coil (CPC, Noras GmbH, Germany) and three sequences: proton-density-weighted, fat-saturated TSE SPAIR (PDw, $T_R/T_E$ = 3400/11 ms, turbo factor [TF]=7, flip angle [FA]=90/150, bandwidth [BW] = 223 Hz/pixel), turbo inversion recovery (IR, $T_R/T_E/T_I$ = 7000/11/50, 200, 500, 1000 and 2000 ms, TF = 9, FA = 180/90/180, BW = 250Hz/pixel) and multi-echo spin-echo ($T_R/\tau$ = 5000/12ms, 16 echoes, FA=90/180, BW=250Hz/pixel) without fat suppression. The time points for the measurements were chosen to document adequately the hyperacute (<24 h), acute (1–3d), early subacute (>3 d), late subacute (>7 d) and chronic (>14 d) stages, as defined by Bradley (13). Due to the length of the entire protocol, an explicit $T_1$-weighted sequence was omitted and the different $T_1$-related weightings of the IR sequence were analyzed for their usefulness instead. For the analysis of $T_2$-weighted (T2w) images, echo 9 of the multi-echo spin-echo sequence was used. The field of view for all scans was 100 × 100 $mm^2$, with a resolution of 192 x 192 and a slice thickness of 1.5 mm.

For all sequences, prescan normalize and distortion correction filters were applied. For the IR sequence, noise cancelling (image filter medium) was used in addition.

### Data analysis

Data for 12 persons (6 female, 6 male, mean age 26.91 ± 3.98y) were analyzed for model creation (two persons were excluded due to severe motion artefacts, two due to strong $B_1$ inhomogeneities, for two volunteers venules were perforated during injection and two were statistical outliers). After creation, the model was also applied to the excluded statistical outliers to account for this variability, which would also be expected to occur in a larger human population. Signal intensities were measured in the hematoma, muscle and subcutaneous fat, respectively, by placing three circular regions of interest (ROI, area range 0.4–0.55$cm^2$) in each of these areas and calculating the average of the signal intensities. The ROIs were defined in the PDw images, since they provided the best contrast of the hematoma versus subcutaneous fat and muscle tissue. It was ensured that all ROIs lay well within the high signal-to-noise ratio (SNR) range of the surface coil (60 mm). The size of the ROI was defined for the initial measurement and then kept constant for the entire analysis of one volunteer. To minimize contrast variations due to unsteady degradation of a hematoma within a defined ROI, care was taken that the regions were placed centrally in large, homogeneous signal regions. Since the data analysis was performed at the end of the study, this ensured that the ROIs included hematoma tissue for all measurements. Therefore, the contrast changes are mainly produced by the decreasing fraction of blood in the subcutaneous fatty tissue.

The contrast between two tissues was determined using the Michelson contrast (20), $C_M = (I_1 - I_2)/(|I_1| + |I_2|)$, which allows for a comparison of the contrast in different volunteers by normalizing to the sum of the signal intensities.

### Model creation

Prior to the creation of the model, the data for all sequences were analyzed and those results with a characteristic behavior over time were identified. A model was created using the contrast measurements between hematoma ($I_1$) and muscle ($I_2$) of the PDw sequence and the IR sequence for $T_I$ =200 ms and $T_I$ =1000 ms, respectively; the data of the T2w sequence were not included in the model.

For each sequence, the data of all volunteers were averaged and approximated by a monoexponential fit according to equation [1]:

$$C_M(T) = C_0 \times e^{-T/(C_T)} + C_B \qquad [1]$$

where $C_M(T)$ is the Michelson contrast at a certain time, $C_0$ is the starting value of the Michelson contrast at $T = 0$, $T$ is the hematoma age in hours, $C_T$ is the time constant for the decrease of contrast in hours and $C_B$ is the baseline value.

Since the hematoma is located in the subcutaneous fat, the signal intensity of the hematoma region will return to that of fat when completely decomposed. Therefore, the baselines of the monoexponential fits were determined by calculating the contrast between fat and muscle; thus, only two free parameters remained for the fitting routines.

The resulting mathematical functions of the monoexponential fits were then used to calculate lookup tables with a temporal resolution of 0.1 h between 0 and 336 h (=2 weeks). For the calculation of age estimates, the lookup table was searched for the closest contrast value, with the corresponding value of $T$ being the estimated age. As the curves were only defined for a

temporal range between 0 and 336 h, age estimates were restricted to this range. Contrast values beyond the lookup values therefore result in age estimates of either 0 h or 336 h, respectively.

The age estimates of the three lookup tables for the different sequences were averaged to provide one final result per volunteer and measurement. Additionally, the influence of a different weighting of the results was investigated by evaluating the limits of agreement as a function of the weights.

The reliability of the method was tested by cross-validation using the leave-one-out method (LOOM), i.e. the monoexponential fits were applied to the data of all but one volunteer and the resulting lookup tables were then used to estimate the age of the remaining volunteer's hematoma.

This method is strongly influenced by the variation between the volunteers and is therefore very useful in finding the weaknesses of an applied model. The results of the cross-validation were analyzed using Bland–Altman plots to reveal possible systematic errors and by evaluating the 95 % confidence interval of the final age estimates as limits of agreement (±1.96 SD).

## RESULTS

Figure 1 shows the aspect of an artificial hematoma in one volunteer in three sequences over time. The hematoma can be distinguished easily from the fatty tissue in the $T_2$-weighted images as being hypointense compared with the surrounding subcutaneous fatty tissue. After one week the contrast between the two tissues is strongly reduced and after two weeks the hematoma cannot be seen any more.

The proton-density-weighted images show a steady decrease of the hematoma's signal intensity from the beginning to the end of the interval investigated; however, a hyperintense area is still slightly visible after two weeks.

In the IR images for $T_I$ =200 ms the hematoma is hypointense compared with the subcutaneous fat. In the course of the following two weeks, this hypointensity becomes weaker and the hematoma becomes almost isointense. At the end of the investigated interval, some remnants of the hematoma can still be seen. For $T_I$ =1000ms (images not shown) the hematoma could only be delineated for the first three days after hematoma creation. The contrast was hyperintense compared with subcutaneous fat and the increase was markedly steeper than that for $T_I$ =200 ms.

In Figure 2, the averaged Michelson contrast values for the hematoma versus muscle tissue of all volunteers are shown for the three different sequences. The curves in Figure 2(b) and (c) are the monoexponential fits defined by Equations [2].

The averaged curve of the T2w results (Fig. 2a) shows a small dynamic range <0.1. The standard deviation between 0.031 (at 168 h) and 0.060 (directly after injection) is large compared with this dynamic range, particularly in the first few days after the injection of the blood.

The PDw results (Fig. 2b) show a large dynamic range of 0.615 from +0.3 to -0.315 for the averaged curve. In relation to this range, the standard deviation between 0.056 (3 h) and 0.1 (24 h) is much smaller, while the absolute values are higher compared with the T2w results.

The Michelson contrast for the IR sequence with two different inversion times $T_I$ is shown in Figure 2(c). The contrast curve for $T_I$ = 200 ms depicts a steady increase from –0.54 to –0.095 with a minimum SD of 0.054 (168 h) and a maximum value of 0.1 for the standard deviation after 72 h. The results for $T_I$ = 1000 ms show a sharp increase of 0.15 within the first day and a slight increase between day 1 and day 3. Standard deviations for this contrast were between 0.11 (24 h) and 0.19 (directly after injection) and after day 3 the hematomas could no longer be outlined clearly.

Equations [2] show the results of the monoexponential fits to the complete data:

$$\begin{aligned} C_{M,PD} &= 1.00\times e^{-T/356.73h} - 0.71 \\ C_{M,IR200} &= -0.48\times e^{-T/182.64h} - 0.05 \\ C_{M,IR1000} &= -0.35\times e^{-T/83.81h} + 0.75 \end{aligned} \quad [2]$$

in which $T$ is the age of the hematoma in hours and $C_{M,PD}$, $C_{M,IR200}$ and $C_{M,IR1000}$ are the Michelson contrast coefficients for PDw, $IR_{200}$ and $IR_{1000}$, respectively. Due to the high standard deviation in the T2w results, no curve was fitted to these data.

Figure 3(a) shows a comparison between true hematoma age and the values estimated by the model in all volunteers and measurements using the LOOM approach. The linear regression yields the equation

$$T_{lookup} = 0.88\times T_{real} + 12.41 \text{ h}$$

with $R^2$ =0.95, where $T_{lookup}$ is the estimated hematoma age and $T_{real}$ is the true hematoma age in hours. This result shows a slight

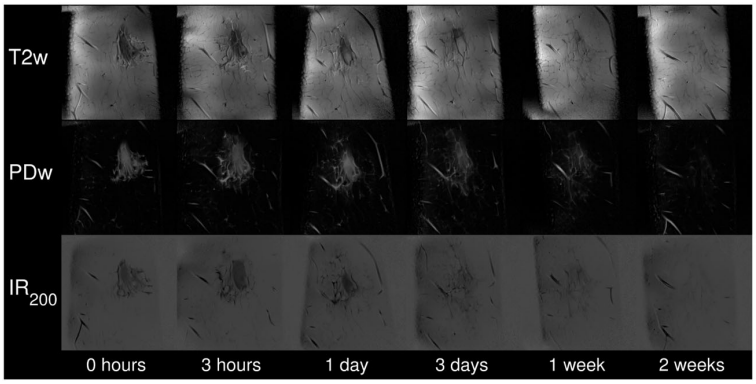


**Figure 1**. MRI data of an artificial subcutaneous hematoma in the oblique plane for one volunteer (f, 29y): T2w, proton-density-weighted and an inversion recovery sequence using $T_I$ =200ms over two weeks.

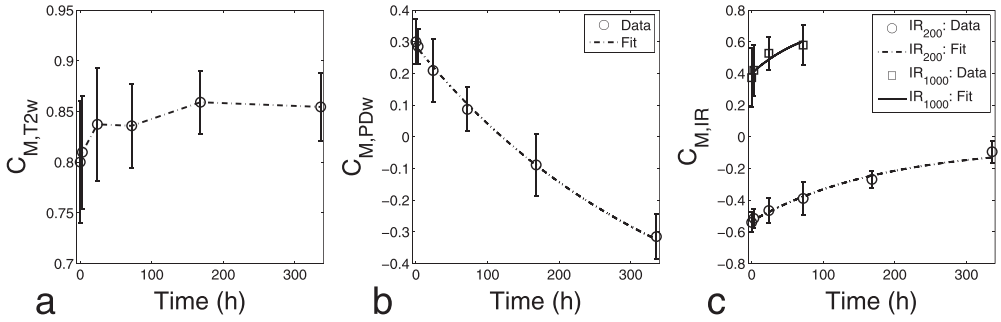


**Figure 2**. Averaged Michelson contrast between hematoma and muscle for all volunteers. The error bars represent the standard deviation for (a) $T_2$ -weighted, (b) PD-weighted and (c) IR data. Curves in (b) and (c) are the monoexponential fits used for calculating the lookup tables. Note the different scalings of the plots.

underestimation (24 h after two weeks) of the hematoma age, particularly with increasing time.

The Bland–Altman plot for the model (Fig. 3b) shows no systematic offset of the estimated times compared with the true hematoma age ($\mu$ =-0.38 h) and the slight underestimation with increasing time can be seen as a decrease of the average values depicted by the dash–dotted line in this plot. For the first three days, the limits of agreement corresponding to ±1.96SD are ±38.7 h ($\mu$ =8.6 h); they increase to ±54.04 h for the entire investigation period of two weeks. Figure 3(c) shows the Bland–Altman plot for one week when the model is applied to all data, i.e. including those volunteers that had been excluded for model creation. This analysis yields limits of agreement of ± 52.91 h ($\mu$ = 6.27 h).

Figure 4 shows the influence of a weighting of the results on the age estimates. The weighting is shown for PDw and $IR_{200}$ data, since these data exist for the entire measurement period of two weeks. The optimum weighting is defined by the minimum of the limits of agreement, which occurs for a ratio of $PDW/IR_{200}$ = 0.62/0.38 (Fig. 4a), corresponding approximately to the ratio of the dynamic ranges of these data. Using the optimum weighting, the limits of agreement can be decreased by 1.65 h compared with averaging the results. Figure 4(b) shows the Bland–Altman plot for optimum weighting, for which the 95% confidence interval is higher than an average of the results of the three lookup tables. Using all lookup tables, an optimum weighting decreases the limits of agreement by 3.12 h for the first three days ($PDw/IR_{200}/IR_{1000}$ =0.54/0.08/0.38) and by 0.33 h for the entire two weeks (only PDw and $IR_{200}$ data).

Investigating the strong variability of the T2w data, a weak correlation ($R^2$ = 0.27) of the average signal intensity of each measurement with the pH value of the respective fresh venous blood sample was found (not shown).

## DISCUSSION

In order to estimate the age of subcutaneous hematomas, which is important in clinical forensic medicine, e.g. in child abuse, the contrast of such hematomas in MRI was investigated over a period of two weeks and a model that describes the contrast behavior in proton-density-weighted and inversion recovery data over time was created.

The model is based on standard commercially available sequences and allows for an estimation of hematoma age with limits of agreement of ±38.7 h within the first three days and ±54.04 h during the entire investigation period of two weeks since its origin, which according to our practical experience corresponds to the approximate interval during which subcutaneous hematomas are usually visible.

The small dynamic range and large variation of the averaged T2w curves were surprising, since a notable change in $T_2$ and with it a change in the contrast behavior was expected from the literature (13,21). These characteristics suggest that subcutaneous hematomas behave differently from intracranial

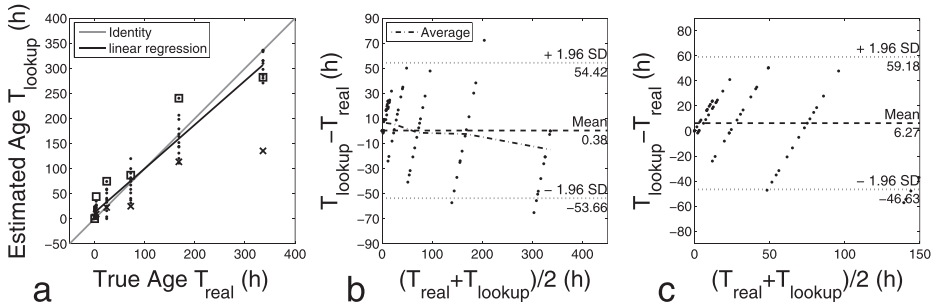


**Figure 3**. (a) Estimated results versus true hematoma age. The squares and crosses show the hematoma age estimates for those volunteers who were excluded from the model creation and the linear regression. (b) Bland–Altman plot of the results of model age estimation. (c) Bland–Altman plot for one week, including results for those volunteers excluded for model creation.

NMR IN BIOMEDICINE

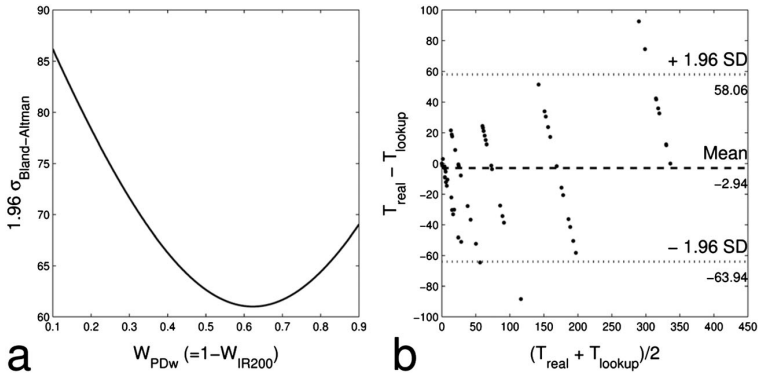


**Figure 4**. Optimum weighting of PDw and $IR_{200}$ results. (a) Bland–Altman 95% confidence interval as a function of $\mathbf{W_{PDw}}$, the weight for the PDw data. $\mathbf{W_{PDw}}$ is defined as $\mathbf{W_{PDw}}=\mathbf{1}-\mathbf{W_{IR200}}$, where $\mathbf{W_{IR200}}$ is the weighting for $IR_{200}$ data. (b) Bland–Altman plot for optimum weighting when only using PDw and $IR_{200}$ data.

hematomas and that *in vitro* results cannot simply be adopted for *in vivo* settings. One reason could be that the $T_2$ - weighted contrast of soft tissue hematomas is influenced by the pH of the extravasated blood.

This assumption, however, is based only on the weak relationship that could be seen between the average signal intensity and the pH value of the fresh venous blood. As this parameter is usually not known and, in addition, appears to show great interindividual variation, the use of T2w data – at this moment – does not seem to be suitable for the age determination of subcutaneous hematomas.

The fat-saturated proton-density-weighted sequence has been shown to be suited for the imaging of soft tissue hematomas, providing high contrast for new bruises and a maximum change over time up to two weeks. The exponential decrease could be the result of an increasing hematocrit proportion and a decreasing water content in the hematoma with ongoing resorption (22).

The Michelson contrast curves of the inversion recovery sequence are the result of the declining proton density and a steady decrease of hematoma $T_1$. Especially at the beginning of the investigation period, this decrease was much faster than expected from intracranial hematomas (13) and from *in vitro* results (21), which both indicate that $T_1$ remains constant in the beginning and does not decline during the first three days. The strong increase of $C_M$ during the first days for $T_I$ = 1000 ms bears additional information, especially for new bruises, that led to the incorporation of this contrast into the model.

The different dynamic ranges of the acquired data suggested an investigation of a possible enhancement of the age estimation using a certain weighting of the individual results. In fact, when using only PDw and $IR_{200}$ as input, the optimum weighting of these data accords approximately with the ratio of the dynamic ranges of the two curves. However, the simple averaging of all three curves provides better overall results than the optimum weighting of PDw and $IR_{200}$ data. When investigating the optimum weighting of all three curves, only small improvements can be achieved. The optimum weighting for the first 72 h suggested that PDw and $IR_{1000}$ are sufficient to describe the behaviour of recent hematomas.

However, since the improvement provided by the weighting is small and a reliable determination of the optimum weights needs more data, averaging was chosen over weighting.

The underlying degradation processes of the hematomas were assumed to be exponential. The small bias in the Bland–Altman plot supports this assumption for a period of up to two weeks. However, the linear regression of the estimated results, which could serve as a simple calibration of the model, shows a slight overestimation for recent hematomas and an underestimation in the later period of the two weeks.

As the valid temporal range of the model is currently limited to the period between 0 and 336 h, lookup tables were chosen to avoid truncation of the results to this range when using inverted functions. Additionally, the use of lookup tables has the advantage that contrast results can be compared directly with the plotted lookup table in the same diagram, giving quick feedback on how well the results correlate with the model.

Due to different study designs, our results cannot easily be compared with those published by Randeberg et al. (7). The authors concluded that they could achieve a 1 d accuracy for bruises less than 10d old. However, most of the measured hematomas were less than 4 d old and the authors admitted that the significance for older hematomas still needed to be investigated.

An advantage of the model described in this work is that no additional parameters are needed, while the method of reflectance spectroscopy requires volume fractions of the chromophores, blood oxygenation, scattering properties and skin thickness, which must be measured or derived from mathematical models.

The most important limitation of this study is the difference of blood injections in contrast to real bruises, as they do not include a contusional component. However, the setting used has the advantage that it allowed for a highly reproducible creation of hematomas. The model equations must be verified using data for real bruises created by blunt force. It is expected that the constitution of the surrounding tissue will also influence the signal characteristics. This is underlined by the observation that the two statistical outliers excluded in model creation were both high-performance athletes with markedly reduced fatty tissue (thickness of the subcutaneous fat layer was reduced by a factor of up to 5) compared with the remaining volunteers of the same sex.

It was, however, shown that the created model is also applicable to these volunteers for a hematoma age of up to 1 week. For



  

further investigation of the connection between athleticism and hematoma healing, more data are needed.

The aim of this study was the implementation of a simple model that can be easily adopted and applied and is, thus, completely based on contrast information of standard commercially available MRI sequences. However, a more complex model incorporating additional information such as e.g. relaxometric parameters may enhance accuracy additionally.

Another simple approach, such as a volume determination as is done for intracranial hemorrhage, did not allow for a reliable quantitative analysis, due to the diffuse borders of the blood volumes.

This also is a notable difference between intra- and extracranial hematomas.

The created model allows for an objective estimation of hematoma age, underlining the importance of radiologic methods in forensic medicine. An important advantage of the implemented approach compared with existing methods is the complete independence in relation to color information and hence skin color or skin thickness. Therefore, this method shows the potential to overcome the still unsolved problem of hematoma age determination in forensics.

## Acknowledgements

The authors thank Bridgette Webb for the critical review of the manuscript.

## REFERENCES

1. Langlois N, Gresham G. The ageing of bruises: A review and study of the colour changes with time. Forensic Sci. Int. 1991; 50(2): 227–238.
2. Stephenson T, Bialas Y. Estimation of the age of bruising. Arch. Dis. Child. 1996; 74(1): 53–55.
3. Pilling M, Vanezis P, Perrett D, Johnston A. Visual assessment of the timing of bruising by forensic experts. J. Forensic Legal Med. 2010; 17(3): 143–149.
4. Grossman S, Johnston A, Vanezis P, Perrett D. Can we assess the age of bruises? An attempt to develop an objective technique. Med. Sci. Law 2011; 51(3): 170.
5. Hughes V, Ellis P, Langlois N. The perception of yellow in bruises. J. Clin. Forensic Med.. 2004; 11(5): 257–259.
6. Hughes VK. The practical application of reflectance spectrophotometry for the demonstration of haemoglobin and its degradation in bruises. J. Clin. Pathol. 2004; 57(4): 355–359.
7. Randeberg LL, Haugen OA, Haaverstad R, Svaasand LO. A novel approach to age determination of traumatic injuries by reflectance spectroscopy. Lasers Surg. Med. 2006; 38(4): 277–289.
8. Yajima Y, Funayama M. Spectrophotometric and tristimulus analysis of the colors of subcutaneous bleeding in living persons. Forensic Sci. Int. 2006; 156: 131–137.
9. Li B, Beveridge P, O'Hare WT, Islam M. The estimation of the age of a blood stain using reflectance spectroscopy with a microspectrophotometer, spectral pre-processing and linear discriminant analysis. Forensic Sci. Int. 2011; 212: 198–204.
10. Hassler E, Neumayer B, Petrovic A, Widek T, Ogris K, Yen K, Scheurer E. Contrast of artificial subcutaneous hematomas in different MRI sequences over time. In *29th Annual Meeting of the ESMRMB*. Springer-Verlag: Lisbon, Portugal; 2012; 281.
11. Neumayer B, Hassler E, Widek T, Petrovic A, Scheurer E. Modelling of contrast changes in soft tissue hematomas. In *29th Annual Meeting of the ESMRMB*. Springer-Verlag: Lisbon, Portugal; 2012; 481.
12. Hayman LA, Taber KH, Ford JJ, Bryan RN. Mechanisms of MR signal alteration by acute intracerebral blood: old concepts and new theories. Am. J. Neuroradiol. 1991; 12(5): 899–907.
13. Bradley WG. MR appearance of hemorrhage in the brain. Radiol. 1993; 189(1): 15–26.
14. Linfante I, Llinas RH, Caplan LR, Warach S. MRI features of intracerebral hemorrhage within 2 hours from symptom onset. Stroke 1999; 30(11): 2263–2267.
15. Gomori JM, Grossman RI, Goldberg HI, Zimmerman RA, Bilaniuk LT. Intracranial hematomas: imaging by high-field MR. Radiol. 1985; 157(1): 87–93.
16. Swensen SJ, Keller PL, Berquist TH, McLeod RA, Stephens DH. Magnetic resonance imaging of hemorrhage. Am. J. Roentgenol. 1985; 145(5): 921–927.
17. Rubin JI, Gomori JM, Grossman RI, Gefter WB, Kressel HY. High-field MR imaging of extracranial hematomas. Am. J. Roentgenol. 1987; 148(4): 813–817.
18. Spielmann R, Maas R, Neumann C, Dallek M, Nicolas V, Heller M, Bücheler E. MRT akuter Weichteilhämatome bei 1,5 T: Tierexperimentelle Ergebnisse. Fortschritte auf dem Gebiet der Röntgenstrahlen und der bildgebenden Verfahren 2008; 153 (10): 395–399.
19. Bush CH. The magnetic resonance imaging of musculoskeletal hemorrhage. Skelet. Radiol. 2000; 29(1): 1–9.
20. Michelson AA. *Studies in Optics*. Chicago Press: Chicago; 1927.
21. Petrovic A, Ogris K, Hassler E, Yen K, Stollberger R, Scheurer E. In-vitro blood. In *28th Annual Meeting of the ESMRMB*. Leipzig, Germany; 2011; 566, 398.
22. Hayman LA, Pagani JJ, Kirkpatrick JB, Hinck VC. Pathophysiology of acute intracerebral and subarachnoid hemorrhage: applications to MR imaging. Am. J. Roentgenol. 1989; 153(1): 135–139.

## 2.2 Assessment of Pharmacokinetics for Microvessel Proliferation by DCE-MRI for Early Detection of Physeal Bone Bridge Formation in an Animal Model

[78] Neumayer B., Amerstorfer E., Diwoky C., Lindtner R. A., Wadl E., Scheurer E., Weinberg A.-M., and Stollberger R. "Assessment of Pharmacokinetics for Microvessel Proliferation by DCE-MRI for Early Detection of Physeal Bone Bridge Formation in an Animal Model." In: *Magnetic Resonance Materials in Physics, Biology and Medicine* 30.5 (Oct. 2017), pp. 417–427. DOI: 10.1007/s10334-017-0615-2

### 2.2.1 Summary

When utilizing contrast agents (CA) to increase the signal-to-noise (SNR) respectively contrast-to-noise ratio (CNR) or to investigate vascular characteristics, MR techniques do not require radio-active markers which are necessary for other tomographic techniques like positron emission tomography (PET) or single-photon emission computed tomography. MRI is also sensitive to small-vessel functions for dynamic measurements, which provide information on the condition and functionality of organs, while PET is dominated by large-vessel structures [75]. This makes magnetic resonance a tool to characterize angiogenesis and microvasculature and is therefore used to gain information on tumour microvessel structure and function [75–77, and references therein].

Although it is a main field of application, the analysis of angiogenesis is not limited to tumor research. It can also, for example, be applied to the investigation of healing physeal lesions, where strongly increased vascularity (hypervascularity) is one hypothesized underlying mechanism of the formation of bone bridges.
The formation of bone bridges is reportedly initiated by physeal lesions induced either by trauma or – as a consequence of treatment – intraoperatively by implants advanced through the growth plate in order to stabilize fractures [159]. Bone bridges, usually reversible, can precipitate full or partial premature physeal closure due to incomplete decomposition and therefore lead to full or partial growth arrest [160] causing bone length discrepancy, axis deviation or joint deformity [161]. A severe problem of bone bridges is their concealed formation, which means they are not apparent before the perception of implications, i.e. a disruption of the continued growth of the limb.
The underlying mechanisms involved in the formation of these structures

still remain unclear. However, as blood vessels and vascular invasion are fundamental for the development of bone tissue, strongly increased vascularity may be connected to the synthesis of bone bridges. An early detection of bone bridge formation would allow to enhance healing processes and help avoiding potential complications. Of course, a minimally invasive imaging method like dynamic contrast-enhanced MRI (DCE-MRI) would be preferred in these cases.

The formation of bone bridges was documented in a longitudinal animal study acquiring highly-resolved MR images as well as DCE data of physeal lesions. To analyse the vascularity in the injured areas the pharmacokinetic parameters $K^{trans}$ and $v_e$ were obtained by applying a reference region model (RRM) [97] to the acquired DCE data. The imaging results and the change of the pharmacokinetic parameters over time were compared to histologic and gene expression analyses.

### 2.2.2 Author Contribution

Bernhard Neumayer was involved in MR data collection and responsible for data analysis. He implemented, tested and applied the pharmacokinetic model and performed pre-processing for quantification. The manuscript was mainly written by Bernhard Neumayer.

### 2.2.3 Additional Relevant Publications

[162] Fischerauer E., Heidari N., Neumayer B., Deutsch A., and Weinberg A. M. "The spatial and temporal expression of VEGF and its receptors 1 and 2 in post-traumatic bone bridge formation of the growth plate." In: *Journal of Molecular Histology* 42.6 (Sept. 2011), pp. 513–522. DOI: 10.1007/s10735-011-9359-x

This study used imaging results of the primary publication to show the alleged closing of the physeal lesion followed by a new rupture. These results were compared to histological findings and results of qRT-PCR data.

[163] Baron K., Neumayer B., Amerstorfer E., Scheurer E., Diwoky C., Stollberger R., Sprenger H., and Weinberg A. M. "Time-Dependent Changes in T1 during Fracture Healing in Juvenile Rats: A Quantitative MR Approach." In: *PLOS ONE* 11.11 (Nov. 2016). Ed. by Wallace J. M., e0164284. DOI: 10.1371/journal.pone.0164284

This study investigated the ageing of fractures using quantitative relaxometry data derived from the DCE data acquired for the primary publication.

Magn Reson Mater Phy (2017) 30:417–427
DOI 10.1007/s10334-017-0615-2

RESEARCH ARTICLE

# Assessment of pharmacokinetics for microvessel proliferation by DCE-MRI for early detection of physeal bone bridge formation in an animal model

**Bernhard Neumayer[1,2] · Eva Amerstorfer[3] · Clemens Diwoky[2,4] · Richard A. Lindtner[5] · Elisabeth Wadl[6] · Eva Scheurer[7] · Annelie-Martina Weinberg[8] · Rudolf Stollberger[2,9]**

Received: 19 October 2016 / Revised: 26 February 2017 / Accepted: 7 March 2017 / Published online: 30 March 2017


**Abstract**
*Objectives* Bone bridge formation occurs after physeal lesions and can lead to growth arrest if not reversed. Previous investigations on the underlying mechanisms of this formation used histological methods. Therefore, this study aimed to apply a minimally invasive method using dynamic contrast-enhanced MRI (DCE-MRI).
*Materials and methods* Changes in functional parameters related to the microvessel system were assessed in a longitudinal study of a cohort of an animal model applying a reference region model. The development of morphology of the injured physis was investigated with 3D high-resolution MRI. To acquire complementary information for MRI-related findings qRT-PCR and immunohistochemical data were acquired for a second cohort of the animal model.
*Results* The evaluation of the pharmacokinetic parameters showed a first rise of the transfer coefficient 7 days post-lesion and a maximum 42 days after operation. The analysis of the complementary data showed a connection of the first rise to microvessel proliferation while the maximum value was linked to bone remodeling.
*Conclusion* The pharmacokinetic analysis of DCE-MRI provides information on a proliferation of microvessels during the healing process as a sign for bone bridge formation. Thereby, DCE-MRI could identify details, which up to now required analyses of highly invasive methods.

**Keywords** Contrast agents · Animal model · Physis

**Abbreviations**

| | |
|---|---|
| $K^{trans}$ | Transfer coefficient |
| $v_e$ | Extravascular extracellular volume |
| AIF | Arterial input function |
| CA | Contrast agent |
| DCE | Dynamic contrast enhanced |
| FA | Flip angle |
| FLASH | Fast low angle shot |
| FOV | Field of view |
| Hif1a | Hypoxia-inducible factor 1a |
| PD | Proton density |
| RARE | Rapid acquisition with relaxation enhancement |
| RNA | Ribonucleic acid |
| RR(M) | Reference region (model) |
| SNR | Signal-to-noise ratio |
| TOI | Tissue of interest |
| VEGFa | Vascular endothelial growth factor a |

✉ Rudolf Stollberger
rudolf.stollberger@tugraz.at

[1] Ludwig Boltzmann Institute for Clinical Forensic Imaging, Universitätsplatz 4, 8010 Graz, Austria

[2] BioTechMed, University of Graz, Universitaetsplatz 3, 8010 Graz, Austria

[3] Department of Paediatric and Adolescent Surgery, Medical University of Graz, Auenbruggerplatz 34, 8036 Graz, Austria

[4] Institute of Molecular Biosciences, University of Graz, Humboldtstraße 50, 8010 Graz, Austria

[5] Department of Trauma Surgery, Medical University of Innsbruck, Anichstrasse 35, 6020 Innsbruck, Austria

[6] Department of Pathology, Clinical Center Klagenfurt, Feschnigstraße 11, 9020 Klagenfurt, Austria

[7] Institute of Forensic Medicine, University of Basel, Pestalozzistraße 22, 4056 Basel, Switzerland

[8] Department of Orthopedics and Orthopedic Surgery, Medical University of Graz, Auenbruggerplatz 5, 8036 Graz, Austria

[9] Institute of Medical Engineering, Graz University of Technology, Stremayrgasse 16/III, 8010 Graz, Austria

## Introduction

Premature physeal bone bridge formation can be induced by a variety of physeal insults including trauma, infection, radiation, ischemia, thermal injury, Blount disease, steroid use, as well as, iatrogenic and unknown etiologies [1]. Trauma in general including iatrogenic trauma from metal implantation is considered as the leading cause for formation of a physeal bone bridge [2, 3]. Bone bridges may be reversible when they are small, but can also trigger full or partial premature physeal closure due to incomplete decomposition and therefore may lead to full or partial growth arrest causing bone length discrepancy, axis deviation or joint deformity [4–7]. Clinically, they are detected by X-ray examinations, which are either routinely conducted to document fracture healing or initiated in patients with posttraumatic bone length alterations or deformities. MRI is then used to document the full size of the bridge and help in defining further management [1, 4, 8, 9].

A severe physeal bone bridge alters normal longitudinal bone growth and requires either surgical resection and filling up the lesion with autologous fat tissue as remedial measure or it is managed by contralateral epiphysiodesis or corrective osteotomy [1, 5, 6, 9]. Furthermore, stem cell therapy [10] and autogenous cultured physeal chondrocyte transplantation [11] have been recently investigated experimentally as novel therapeutic option. In contrast, minor bone bridges usually remain concealed and disappear during further growth, without impairing normal longitudinal growth [6, 7, 12]. Physeal bone bridge formation has been documented histologically [13–18] and by MRI [15, 16, 18] in various experimental animal models. Vascularization of the physeal lesion has been reported to precede physeal bone bridge formation [15, 19]. Along with invading vessels from surrounding epiphyseal and metaphyseal bone, mesenchymal osteoprogenitor cells emerge into the physeal lesion site and are attributed to deposit bone which eventually leads to bone bridge formation [15, 19]. The hypothesis that increased blood supply at the injury site is connected to the creation of physeal bone bridges as blood vessels and vascular invasion are fundamental for the development of bone tissue was further recently supported by the detection of increased angiogenic factor expression within the physeal injury site prior to bone bridge development [13, 20]. However, the underlying pathomechanism inducing angiogenesis followed by formation of a physeal bone bridge remains unexplored. The detection of an increase in blood supply in a physeal lesion could therefore allow an early identification of bone bridge formation and while the determination of angiogenic expression factors requires tissue samples, magnetic resonance imaging is potentially capable of providing this information non-invasively.

Dynamic contrast enhanced MRI (DCE-MRI) is sensitive to functional parameters of the microvessel system. It is therefore a tool to characterize angiogenesis and microvasculature and is widely used for the analysis of tumors [21–23]. The identification of pharmacokinetic parameters should therefore allow following the time course of microvessel-related functional changes during tissue remodeling on an injured physis.

Typical models for the identification of pharmacokinetic parameters [24] require information on the time course of tissue contrast agent (CA) concentration and on the CA concentration within a feeding artery—the arterial input function (AIF). The simultaneous acquisition of both characteristics, i.e. the coverage of the AIF and, in this case, the physeal lesion in the same field of view (FOV), is very challenging and determines the limits for signal-to-noise ratio (SNR), contrast behavior and temporal or spatial resolution [25–27].

For investigations where no adequate arterial input function is available in the field of view population-based averaged AIFs [28–30] or model-based arterial input functions [31] can be applied to avoid a decrease in SNR or temporal resolution by modifying the FOV. A drawback of these methods is, however, that inter-individual variations between subjects or variations of the AIF due to manual CA administration cannot be covered. A different approach is to determine the CA dynamics of a reference tissue with known pharmacokinetic behaviour within the field of view. These dynamic data can then be used to apply a reference region model (RRM) which allows for the quantification of the pharmacokinetic parameters of a tissue of interest without the direct measurement of or assumptions on the AIF [32, 33].

The aim of this study was to investigate pharmacokinetic parameters of the microvessel system of a physeal lesion in correlation to bone bridge formation. These parameters are typically increased in tissues with enhanced metabolism and related to permeability surface product, blood flow and also blood volume. The investigation of these parameters should support the hypothesis that changes of the microvessel system are basic mechanisms associated with bone bridge formation and can provide quantitative measures for an early identification of this development.

The investigation of physeal lesions in a rat model using DCE-MRI required a very high spatial resolution and the application of a reference region model. As a complementary independent measure the results of the MRI analyses were compared to histologic findings and expression rates of genes related to vascular growth and oxygenation provided by quantitative real-time reverse transcription

polymerase chain reaction data (qRT-PCR), which were acquired for a second cohort of animals.

## Materials and methods

### Animals

All animal experiments were conducted under animal ethical respect and were authorized by the Austrian Ministry of Science and Research. Seventy-seven male Sprague–Dawley rats with a weight of approximately 100 g and an age of one month were subjected to unilateral physeal lesion in general anesthesia using a standardized drill procedure [13, 14, 17, 34]. A longitudinal transepiphyseal lesion of 1.2 mm diameter was drilled through the proximal tibial physis, advanced from proximal by a median incision of the patella tendon.

For qRT-PCR analyses six animals were euthanized on days 0, 1, 3, 7, 14, 28 and 82 post-operation for sample dissection. For histological investigations five animals were sacrificed on days 1, 3, 7, 14, 28, 42 and 82; for the five animals designated for euthanasia on day 82 MR measurements were performed under anesthesia on the same seven time-points.

The investigation time-points were set in short intervals during the first month post-injury in order to closely follow bone bridge formation and changes in the microvessel system. The long-term time-points of 42 and 82 days were determined to follow further growth, physeal remodeling and to detect a potential disappearance of the bone bridge.

### MR measurements

Magnetic resonance imaging of the morphology and DCE-MRI were performed on a clinical 3 T scanner with 38 mT/m gradient strength (Tim Trio, Siemens AG, Erlangen, Germany). For enhanced image quality, especially suited surface received coils with a diameter of 18 mm (Rapid Biomedical, Rimpar, Germany) were used. Using an arrangement as shown in Fig. 1 a minimum distance to the rat knees and thereby a maximized SNR could be maintained for the complete duration of the study. Animals were placed in prone position with their knees in the center of the coils. This arrangement was positioned in a semicircular animal bed (Rapid Biomedical) providing a stable and reproducible assembly. As mentioned above, the measurements were performed on days 1, 3, 7, 14, 28, 42 and 82.

Morphological changes of the investigated area were imaged with a high-resolution 3D FLASH sequence ($T_E = 7$ ms, $T_R = 100$ ms, FA $= 15$, scanning matrix $256 \times 256$, FOV $= 50$ mm, THK $= 0.72$ mm) and coronal slice orientation related to the scanner's reference system. Image quality was documented calculating $\mathrm{SNR} = \mu_{\mathrm{signal}}/\sigma_{\mathrm{corr}}$, in which $\mu_{\mathrm{signal}}$ is the average image intensity in a region of interest and $\sigma_{\mathrm{corr}}$ is the standard deviation of a background region corrected for Rayleigh distribution. The corrected standard deviation is calculated $\sigma_{\mathrm{corr}} = \sigma_{\mathrm{Rayleigh}}/0.655$ with $\sigma_{\mathrm{Rayleigh}}$ being the standard

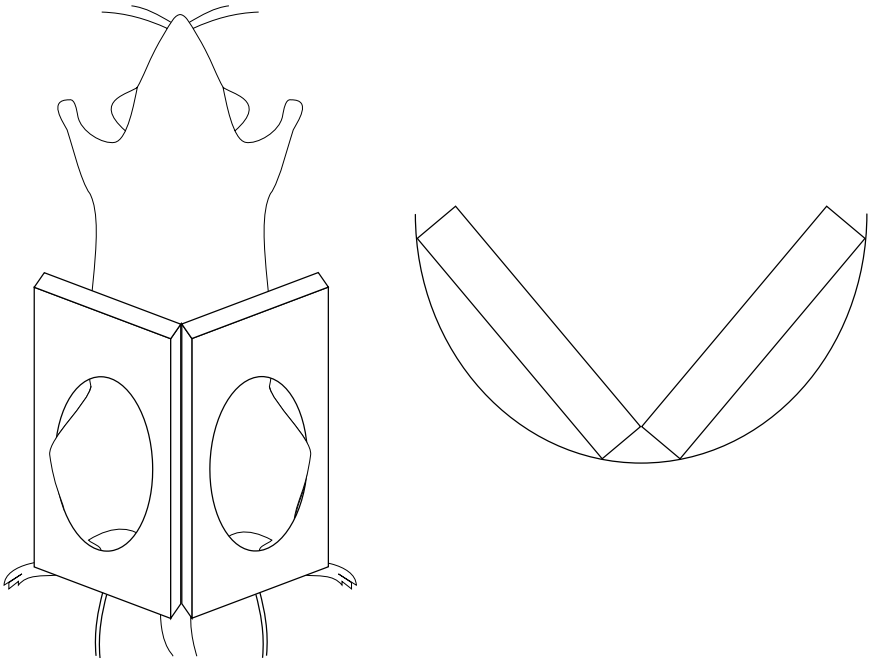

**Fig. 1** Arrangement of the surface coils for all MR measurements. *Left*: bottom view, *right*: arrangement of coils in the animal bed

deviation measured in the image background region. Regions of interest for SNR determination were skeletal muscle and the physis.

The scans for DCE-MRI analysis comprised a single PD-weighted 3D FLASH reference sequence ($T_E = 2.95$ ms, $T_R = 100$ ms, FA = 5) scan and a $T_1$-weighted dynamic 3D FLASH sequence ($T_E = 2.95$ ms, $T_R = 8.09$ ms, FA = 30) with a temporal resolution of $\Delta t = 13.32$ s. This combination follows the basic idea of the approach proposed by Hittmair et al. for 2D FLASH acquisitions [35]. Postoperatively a double-dose injection (0.2 mmol/kg) of Gadovist (Schering AG, Berlin, Germany) was manually administered intravenously in the tail vein for DCE-MRI. The administration started after the acquisition of three baseline images for the calculation of pre-contrast longitudinal relaxation time $T_1$; the entire protocol comprised 40 acquisitions. All scans for DCE-MRI were acquired in coronal orientation and featured a 205 × 256 matrix, a field of view of 50 mm and a slice thickness of 0.72 mm.

### Reference region model

Due to the absence of an adequate vessel providing an arterial input function in the FOV, blood supply related properties of the lesioned tissue were investigated by applying a reference region model [33] to the acquired DCE data. Maps of the longitudinal relaxation time $T_1$ were generated as proposed by Merwa et al. [36] according to Eq. (1)

$$T_1(t) = -\frac{T_{R,\mathrm{DCE}}}{\ln\left(\frac{S_{\mathrm{REF}}\sin(\theta_{\mathrm{DCE}}) - S_{\mathrm{DCE}}(t)\sin(\theta_{\mathrm{REF}})}{S_{\mathrm{REF}}\sin(\theta_{\mathrm{DCE}}) - S_{\mathrm{DCE}}(t)\sin(\theta_{\mathrm{REF}})\cos(\theta_{\mathrm{DCE}})}\right)}, \quad (1)$$

where $S$ is the signal intensity in the image, $\theta$ is the flip angle and the subscripts REF and DCE denote reference scan and dynamic scan, respectively. According to Yankeelov et al. [33] and using the notation suggested by Tofts et al. [24], the relaxation rate $R_1 \equiv 1/T_1$ of a tissue of interest (TOI) is related to the reference region by

$$\begin{aligned} R_{1,\mathrm{TOI}}(T) = {} & R \cdot (R_{1,\mathrm{RR}(t)} - R_{10,\mathrm{RR}}) + R \cdot [K^{\mathrm{trans,RR}}/v_{\mathrm{e,RR}} \\ & - K^{\mathrm{trans,TOI}}/v_{\mathrm{e,TOI}}] \times \int_0^T (R_{1,\mathrm{RR}} - R_{10,\mathrm{RR}}) \quad (2) \\ & \mathrm{e}^{(-K^{\mathrm{trans,TOI}}/v_{\mathrm{e,TOI}})(T-t)}\mathrm{d}t + R_{10,\mathrm{TOI}}. \end{aligned}$$

In Eq. (2) $K^{\mathrm{trans}}$ is the transfer coefficient, $v_e$ is the extravascular extracellular volume, $R$ equals $K^{\mathrm{trans,TOI}}/K^{\mathrm{trans,RR}}$, $R_{10}$ is the native relaxation rate in absence of a contrast agent and TOI and RR denote the tissue of interest and the reference region, respectively.

The reference region for all investigations was skeletal muscle close to the area of the physeal lesion, i.e. the tissue of interest, and the pharmacokinetic parameters of skeletal muscle were set to $K^{\mathrm{trans,RR}} = 0.045\ \mathrm{min}^{-1}$ and $v_{\mathrm{e,RR}} = 0.08$ [37–39]. For all measurements, the subjects' knees were located as close as possible to the center of the 3D slab to avoid different biases for the estimates of $R_1$ for RR and TOI due to $B_1$ inhomogeneities. The least mean squares routine for the parameter identification of $K^{\mathrm{trans,TOI}}$ and $v_{\mathrm{e,TOI}}$ was realized in MATLAB (TheMathWorks Inc., Natick, MA, USA).

### Histology

To obtain information on vascularisation complementary to the results of the analysis of the pharmacokinetic parameters, immunohistochemical analysis was performed for samples of the proximal epiphysis, physis and metaphysis of the tibial bone on the same days for a second cohort of animals.

Histological samples were fixed in methanol (100%) for 24 h and subsequently subjected to decalcification using Ethylenediamine Tetraacetic Acid (pH 7.0) for two weeks. Following a further fixation step in methanol (100%) for 12 h the samples were washed in PBS-sucrose 5% solution, covered with tissue freezing medium (Tissue Tek O.C.T. Compound, Sakura Finetek Europe B.V., The Netherlands) and cut into slices of 7 mm thickness.

To visualize angiogenesis of the physeal defect a collagen IV staining was used, as collagen IV represents a protein of the basal membrane of vessels, staining vasculature in a red/brown colour.

### Quantitative real-time reverse transcription polymerase chain reaction

Additionally to MR measurements and histological analysis, factors related to vascular growth and oxygenation were determined using quantitative real-time reverse transcription polymerase chain reaction analyses. The qRT-PCR analyses were performed for vascular endothelial growth factor a (VEGFa), which is a key parameter of angiogenesis [40] and hypoxia-inducible factor 1a (Hif1a) as a reporter for hypoxia.

For the analysis, physeal samples were dissected from the epiphysis and metaphysis under the microscope before storage in liquid nitrogen. The samples were homogenized using a tissue homogenizer and RNA was extracted using TRIZOL (Gibco BRL). Total RNA samples (2.5 mg) were reverse transcribed at 42 °C for 15 min using random hexamer priming. To establish quantitative expression profiles for VEGFa and Hif1a, commercially available, pre-optimized real time-PCR assays (Assay On Demand, Applied Biosystems) were used. Three reference genes (internal controls) were used for relative quantification. Normfinder [41] software was used to identify the optimal reference gene for internal normalization from a set of house-keeping

genes. Triplicates were averaged and data was normalized to the house keeping gene $\beta$-actin of day 0.

### Statistical analysis

Statistical analysis was performed in SPSS 22 (SPSS Chicago, IL). Differences between results were tested for significance applying a post hoc Bonferroni test and a $p$ value threshold of 0.05 for statistical significance; a p-value below 0.01 was considered highly significant.

## Results

Figure 2 shows the high resolution and the excellent contrast of the morphological images acquired with the setting described above. The scans show the changes of the lesioned area of the physis (marked by arrows) of one representative animal for all 7 time points of the study and document the formation of bone bridges: On days 1 and 3 after the drill procedure, the drill mark causing physeal interruption is clearly visible. On day 7 the physeal interruption caused by the drill mark disappears leaving a homogenous high signal physis. A first low-signal bone bridge can be seen as early as on day 14 and progressively becomes more defined as a larger low-signal interruption within a high signal physis. These interruptions did not dissolve until the end of the study. SNR values showed an observable decrease after two weeks: skeletal muscle exhibited an average SNR of 82 in the first 14 days and 76 afterwards. For the physis, the SNR dropped from 72 to 36 on average.

The analysis of the reference regions of all days and subjects yielded a relaxation rate of $0.82 \pm 0.17\ s^{-1}$. The results for the transfer coefficient and the extravascular extracellular volume provided by the reference region model are shown in Fig. 3: on day 1 post-operation $K^{trans}$ is at a minimum and $v_e$ is notably high; however, with strong variations. On day 3 a non-significant increase of the transfer coefficient accompanied by a decrease in $v_e$ is evident. The value of $K^{trans}$ on day 7 is significantly increased compared to day 1 and reaches its maximum on day 42 post-operation (highly significant different from day 14) with a concomitant increase of the extravascular extracellular space. Between the results of days 7, 14 and 28 no statistically significant differences exist. The value for the transfer coefficient decreased significantly from day 42 to day 82 accompanied by a decrease of $v_e$. For the entire study the results for $v_e$ did not show significant differences between measurement days.

Concerning factors of vascular growth, a first visible but non-significant increase occurs on day 1 for VEGFa as an immediate reaction to the operation (Fig. 4). The only significant difference for VEGFa can be observed on day 7 post-lesion which shows increased values compared to the baseline (day 0) and days 14 and 82. The expression of Hif1a increases from day 1 on with maximum values on day 3 yielding a highly significant increase compared to days 0, 14 and 82.

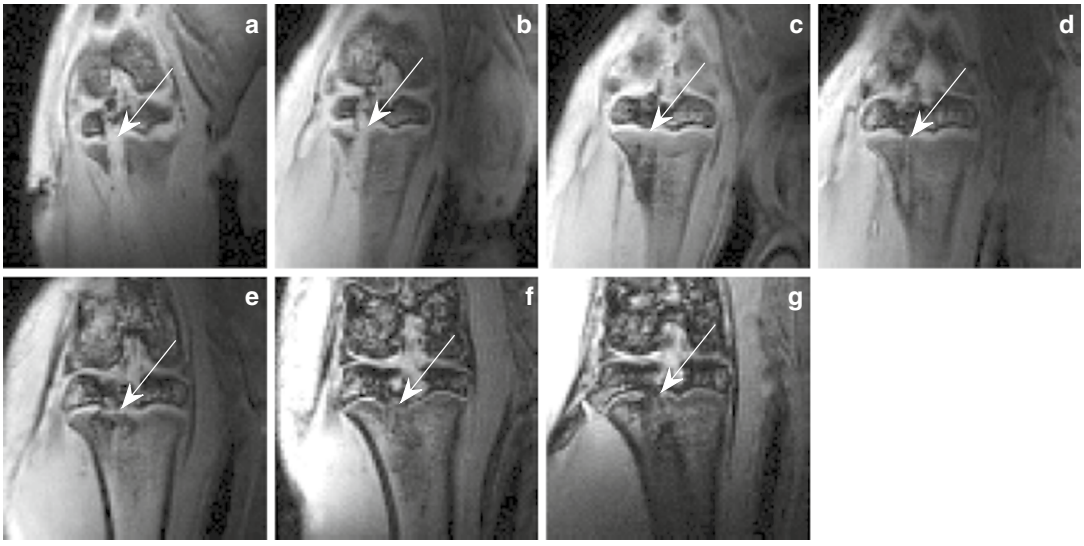


**Fig. 2** High resolution, non-contrast-enhanced MR Images of the lesioned area (*arrow*) in the tibial physis of one subject on days **a** 1, **b** 3, **c** 7, **d** 14, **e** 28, **f** 42 and **g** 82 post-lesion (images were brightened for a better view of the anatomy). The formerly disrupted area looks closed on day 7 but on day 28 it is clearly disrupted again

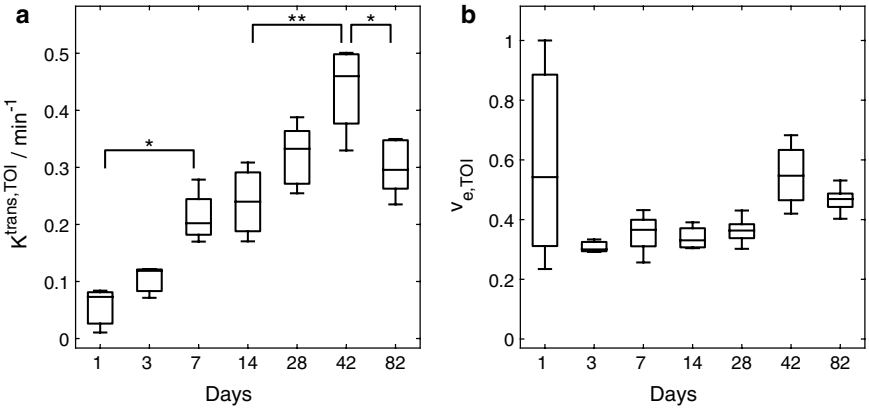


**Fig. 3** Results for **a** $K^{trans}$ and **b** $v_e$ ($n = 5$ for each day). *Horizontal bars* indicate the median, the 25th and 75th percentiles. The values for the transfer coefficient start to increase after 3 days and reach their maximum on day 42 post-operation. The volume of the extravascular extracellular space is increased on days 1 and 42 but does not show statistically significant changes. Statistical changes are marked with $*p < 0.05$ and $**p < 0.01$, respectively

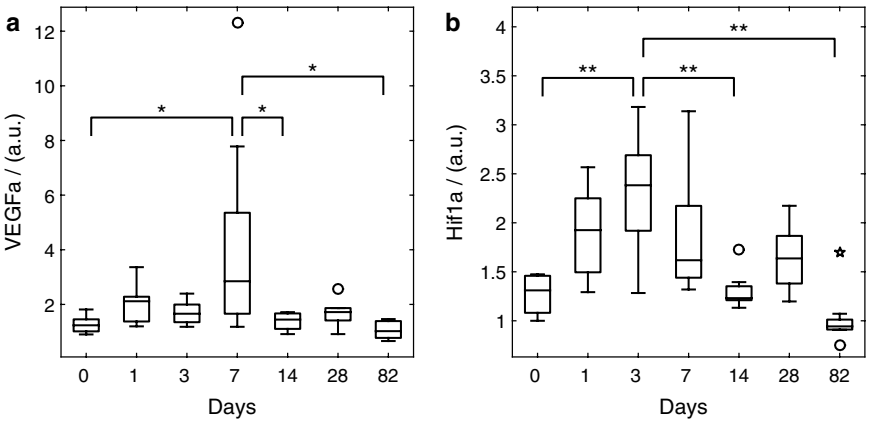


**Fig. 4** Quantitative real time reverse transcription PCR results for **a** VEGFa and **b** Hif1a ($n = 6$ for each day). *Horizontal bars* indicate the median, the 25th and 75th percentiles, minor outliers are displayed with a *circle*; major outliers with a *star*. Maximum vascular growth occurs on day 7 (VEGFa), forgone by maximum hypoxia on day 3 (Hif1a). Statistical changes are marked with $*p < 0.05$ and $**p < 0.01$, respectively

Finally, histological investigations additionally showed the development of microvasculature in the physeal defect. Figure 5 shows collagen IV-stained histologic slices of days 1, 3, 7, 14, 28, 42 and 82 of the physeal lesion. On day 1 the staining showed no vascularisation. On days 3 and 7 post-operation the staining clearly displays the presence of capillaries (marked by arrowheads). After two weeks, first bony trabeculae (collagen IV-negative and marked by arrows) are observed within the physeal defect site. At this time-point collagen IV-positive vessels appear to be more structured compared to days 3 and 7. On day 42 the defective area is filled with lamellar bone fragments, which are surrounded by vessels. On day 82 post-operation the number of collagen IV-positive vessels appear reduced compared to day 42.

## Discussion

In order to detect bone bridge formation at an early stage using a minimally invasive method a reference region model was applied to DCE-MRI data of injured physes to analyze the changes of the microvessel system of this tissue. Furthermore, the changes of the pharmacokinetic parameter $K^{trans}$ over time were compared to qRT-PCR data and results of immunohistochemical analyses and the development of bone bridges was observed using high-resolution MRI.

The performed MRI studies show significant and clear time dependent changes of the assessed model parameter $K^{trans}$. This supports the hypothesis that changes of the blood supply are a potential mechanism associated with bone bridge formation of injured physes and permits a detection of the formation even before it becomes visible in MR imaging data.

Although this study was performed on a whole-body system, high quality morphological images could be obtained by using a dedicated receiver coil and by optimizing the parameters of the 3D gradient echo sequence. The used setting provided images with a voxel size of 0.19 mm × 0.19 mm × 0.72 mm, which allowed for an identification of the relevant image details. For the second half of the study the image quality was noticeably decreased. This is owed to the growth of the animals causing an increase in the distance between the surface coils and the region of interest, which consequently lead to a

decrease of the SNR of the acquired data. However, the sharp decrease for the SNR of the physis after 2 weeks is also caused by a diminished signal intensity of the region of interest due to the animals' age. This is also reflected by the much less pronounced decrease in SNR for skeletal muscle. The images did not suffer from susceptibility artifacts; however, for higher field strengths this may be the case, as reported by Taha et al. [42], who found a RARE approach to be superior to FLASH at 9.4 T.

The high quality of the morphological scans provided a good insight into physeal bone bridge formations throughout the whole study. As was to be expected, the lesioned area can be clearly identified shortly after the application of the drilling procedure and the refillment of the injury was largely completed on day 7 post-operation. By only investigating image data for this day, this refillment could be accredited to healing processes closing the physeal lesion. While a remaining damage of the tibia was still visible, the formerly lesioned area of the physis was homogeneously closed and the isointensity of the filled lesion compared to the surrounding physis suggests a refillment with cartilaginous tissue.

First changes in the investigated area become slightly visible in the MR images on day 14 but without additional information these changes cannot be positively assigned to a bone bridge formation. However, the discontinuity of the physeal area on day 28 is a strong indication for bony activity. This new interruption of the physis occurred in all examined subjects indicating a strong connection between injuries across the physis and bone bridge-induced defective healing, as suggested in the literature [13, 15, 17, 34]. The onset of bone bridge formation is in good accordance with findings of a recent study investigating the efficacy of MRI for the detection of changes in bone morphology [42].

The specific requirements of this animal study lead to a moderate temporal resolution of the dynamic scan. This and the lack of a feeding artery in the investigated area required the application of an RRM to acquire pharmacokinetic parameters. The reference region was skeletal muscle and the average relaxation rate of the reference regions of all days and subjects is in good agreement with literature values [43, 44]. The analysis of the pharmacokinetic parameter $K^{\text{trans}}$ revealed changes in the investigated area, which were not visible in imaging data. These changes can be attributed to the underlying mechanisms of the formation of bone bridges, which did not become visible in the morphological images before day 14 and could not be clearly identified before day 28 post-operation. On days 1 and 3 post operation the lesion is mostly filled with blood, thus $K^{\text{trans}}$ cannot be reasonably determined. Especially on the first measurement day the development of blood vessels is expected to be still very low, which hinders a meaningful parameter identification. This, for instance, is reflected in the quite strong variance of the values for $v_e$. However, from day 3 onwards the fitting routines provide robust, i.e. less scattering, results and the increase of $K^{\text{trans}}$ suggests a proliferation of microvessels.

While it is not completely clear whether such an establishment of a microvessel structure triggers a defective healing and thereby hinders a *restitutio ad integrum*, it can be considered as a first sign for the formation of bone bridges. This is a remarkable finding, since prior to this study date neither histologic analysis nor MR image data could unambiguously detect newly formed bone tissue. Histology could confirm the presence of bone fragments in the lesioned area [13] but it is still disputed if these bone fragments within a fracture site lead to the formation of bone bridges, as according to Xian et al. [17], an irrigation of the drill track had no measurable effect on the development of osseous matter. Therefore, the determination of $K^{\text{trans}}$ allows for an earlier detection of bone bridge formation.

After day 3 post-operation the transfer coefficient indicates a steady increase. The maximum value of $K^{\text{trans}}$ on day 42 reflects the blood supply of bone bridges, which could be clearly detected in the morphological images at that time.

The volume of the extravascular extracellular space did not provide additional information. The decrease at the beginning of the study could be interpreted as a sign for increased blood supply; however, it was reported that the RR estimate of $v_e$ and the estimate produced by the standard method with known AIF are not correlated [45]. Therefore, and since the changes of this parameter were only statistically non-significant the course of this quantity was not investigated further.

The analysis of collagen IV-stained histology data confirmed the presence of vascularity from day 3 onwards, which coincided with an increase of $K^{\text{trans}}$. After two weeks the stained vessels appear less scattered but greater in size and first formations of bone bridges can be detected. This is followed by another increase of $K^{\text{trans}}$ until day 42 followed by a decrease between days 42 and 82, which coincides with a seemingly reduced staining. The voxel based integrative parameter $K^{\text{trans}}$ show a smoother development with less variation in comparison to parameter from histological samples.

The increased expression of VEGFa on day 7 is preceded by a rise in the expression of Hif1a with its maximum on day 3. VEGF expression has been reported to be induced by hypoxia [46]. Furthermore, the heterodimeric basic helix-loop-helix protein Hif1 has been attributed to directly activate VEGF transcription in hypoxic cells, implicating Hif1a to play a pivotal role within this cascade [47, 48]. Although, VEGF and Hif1a were not measured

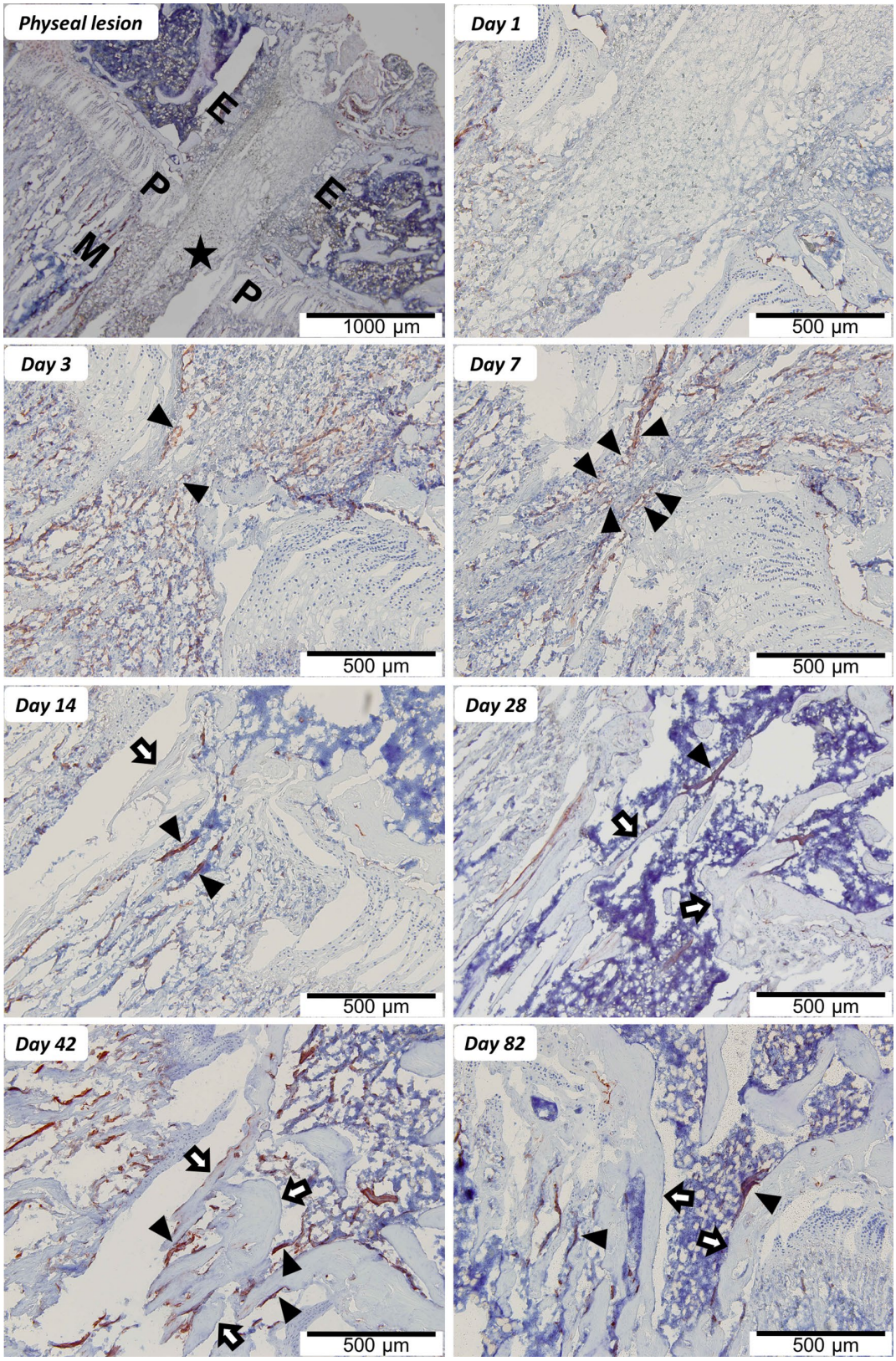
Physeal lesion
E
P
E
M
P
1000 µm
Day 1
500 µm
Day 3
500 µm
Day 7
500 µm
Day 14
500 µm
Day 28
500 µm
Day 42
500 µm
Day 82
500 µm

**Fig. 5** Immunohistochemical expression pattern of collagen IV demonstrating vascular ingrowth preceding bone bridge formation at the physeal lesion site. "Physeal lesion" shows an overview of the physeal lesion (*filled star* lesion, *P* physis, *E* epiphysis, *M* metaphysis of the tibial head). In the remaining images collagen IV-positive vascularization, stained *red/brown*, is highlighted by *arrowheads* (*filled pointer*), while *arrows* (*white arrow*) mark bone fragments which eventually form a bone bridge. The physeal lesion is postoperatively filled by hematoma without obvious vascular demarcation (day 1). Day 3 shows first capillaries ingrowing from surrounding hematoma into the physeal lesion site (indicated by *arrowheads*). The maximum number of capillaries pervading the physeal lesion are seen on day 7. Day 14 shows bony trabeculae traversing the physeal defect, maturing to a bone bridge connecting the epiphysis with the metaphysis by day 28 (marked by *arrows*). By day 42 the bone bridge consists of lamellar bone and is accompanied by distinct vessels, which decline with further maturation of the bridge (day 82)

on protein levels in our study, we suspect that, based on our qRT-PCR results, the changes of the microvessel system and the increased values of $K^{trans}$ occurring on day 7 were most probably triggered by hypoxia within the physeal lesion site. The scattered VEGFa expression observed primarily on day 7 is presumably associated with the relative small sample size, where a short increase of expression towards the randomly selected day 7 may be hard to detect exactly. The statistical outlier of day 7, however, may be due to a contaminated sample by surrounding tissue.

Comparing the results of MR imaging and the pharmacokinetic analyses to the complementary data it can be stated that the increase in $K^{trans}$ corresponds to a filling of the physeal injury with vasculature. The data also shows that the non-significant increase of $K^{trans}$ between days 7 and 14 coincides with a return of VEGFa expression to its initial value on day 14. However, it is also notable that qRT-PCR results reveal a rather pronounced variance in the data while the pharmacokinetic analysis provides a clearly identifiable trend. The results suggest that the combination of high-resolution MRI with a pharmacokinetic analysis allows to identify bone bridge formation at an early stage, while being only minimally invasive.

Currently, Gadolinium-based contrast agents are not generally used for the detection of physeal bone bridges; however, contrast-enhanced measurements are already applied for different disorders, such as the Legg–Calvé–Perthes disease [49]. Therefore, we expect our method to be generally applicable to children, which would provide a quantitative measure for changes in the micro-vessel system associated with the formation of bone bridges at an early stage. The detection of changes in $K^{trans}$ was at least 7 days earlier than the detection of first morphological signs for bone bridges. This time period may translate from the specific animal model to a duration between 6 and 19 months for humans [50, 51], which can be particularly important in cases with concealed physeal bridging. Clinically, many physeal bone bridges may not become evident until months or years have passed and growth disturbances have developed [1]. This highlights the necessity for early recognition of physeal bone bridge formation, which subsequently aids surgical management in order to restore potential growth to the bone.

## Conclusion

In this study, we used DCE-MRI on a clinical system to assess parameters related to blood supply in an animal model in order to investigate the possibility to detect the formation of bone bridges using a minimally invasive method. We conclude that a transphyseal lesion is associated with increased values for $K^{trans}$ which could be observed from day 3 onwards using DCE-MRI. The increase of the transfer coefficient coincides with a presence of vascularity, which appears to trigger the consecutive bone bridge formation and thereby may hinder a *restitutio ad integrum* of the physeal defect.

MR measurements did not only document the formation of bone bridges but additionally provided quantitative information on tissue development and microvessel proliferation in the lesioned area. The analysis of the DCE data enabled an indirect detection prior to visibility in morphology images, which may help in preventing growth disturbances in children by allowing therapeutic intervention early in course. This finding, however, still needs verification in a human study.

**Acknowledgements** Open access funding provided by Austrian Science Fund (FWF). This work was funded by the Austrian Science Fund under Grant SFB F3209-18 and by the AO Research Fund of the AO Foundation, Project S-06-96 W.

**Authors' Contribution** The medical part of the study was defined by EA and AMW, RS was responsible for MRI and pharmacokinetic modelling. Protocols for MR measurements were developed by CD and RS, EA and AMW supervised animal surgery, qRT-PCR and histological investigations. Neumayer implemented, tested and applied the pharmacokinetic model and performed pre-processing for quantification. Data analysis was made by BN, CD, ES and RS. BN, CD, EA and RAL were involved in MR data collection, EW conducted the histological experiments and performed the analyses. The manuscript was mainly written by BN; EA, ES and RS contributed to specific parts. The manuscript has been proof-read and approved by all named authors.

**Compliance with ethical standards**

**Conflict of interest** The authors declare that they have no conflict of interest.

**Ethical statement** All applicable international, national, and/or institutional guidelines for the care and use of animals were followed. All

procedures performed in studies involving animals were in accordance with the ethical standards of the Austrian Ministry of Science and Research.



## References

1. Wang DC, Deeney V, Roach JW, Shah AJ (2015) Imaging of physeal bars in children. Pediatr Radiol 45(9):1403–1412
2. Aitken AP, Magill HK (1952) Fractures involving the distal femoral epiphyseal cartilage. J Bone Joint Surg Am 34A:96–108
3. Boelitz R, Dallek M, Meenen NM, Jungbluth KH (1994) Die Reaktion der Epiphysenfuge auf fugenkreuzende Bohrdrahtosteosynthesen. Unfallchirurgie 20:131–137
4. Ecklund K, Jaramillo D (2002) Patterns of premature physeal arrest: MR imaging of 111 children. AJR Am J Roentgenol 178(4):967–972
5. Escott BG, Kelley SP (2012) Management of traumatic physeal growth arrest. Orthop Trauma 26:200–211
6. von Laer L (1994) Natural course following fractures during the growth years. Orthopade 23(3):211–219
7. Weinberg A, Tscherne H (2006) Tscherne Unfallchirurgie: Unfallchirurgie im Kindesalter-Teil 1: Allgemeiner Teil, Kopf, Obere Extremität. Springer, Berlin
8. Ecklund K, Jaramillo D (2001) Imaging of growth disturbance in children. Radiol Clin North Am 39(4):823–841
9. Sailhan F, Chotel F, Guibal AL, Gollogly S, Adam P, Bérard J, Guibaud L (2004) Three-dimensional MR imaging in the assessment of physeal growth arrest. Eur Radiol 14(9):1600–1608
10. Shukrimi AB, Afizah MH, Schmitt JF, Hui JH (2013) Mesenchymal stem cell therapy for injured growth plate. Front Biosci S5:774–785
11. Tomaszewski R, Bohosiewicz J, Gap A, Bursig H, Wysocka A (2014) Autogenous cultured growth plate chondrocyte transplantation in the treatment of physeal injury in rabbits. Bone Joint Res 3:310–316
12. Kennon JC, Ganey TM, Gaston RG, Ogden JA (2013) Continued growth after limited physeal bridging. J Pediatr Orthoped 33:857–861
13. Fischerauer E, Heidari N, Neumayer B, Deutsch A, Weinberg AM (2011) The spatial and temporal expression of VEGF and its receptors 1 and 2 in post-traumatic bone bridge formation of the growth plate. J Mol Histol 42:513–522
14. Garcés GL, Mugica-Garay I, Coviella NL-G, Guerado E (1994) Growth-plate modifications after drilling. J Pediatr Orthoped 14:225–228
15. Jaramillo D, Shapiro F, Hoffer FA et al (1990) Posttraumatic growth- plate abnormalities: MR imaging of bony-bridge formation in rabbits. Radiology 175:767–773
16. Jaramillo D, Laor T, Zaleske DJ (1993) Indirect trauma to the growth plate: results of MR imaging after epiphyseal and metaphyseal injury in rabbits. Radiology 187:171–178
17. Xian CJ, Zhou FH, McCarty RC, Foster BK (2004) Intramembranous ossification mechanism for bone bridge formation at the growth plate cartilage injury site. J Orthop Res 22:417–426
18. Koff MF, Chong LR, Virtue P, Ying L, Gholve PA, Rodeo SA, Widmann RF, Potter HG (2010) Correlation of magnetic resonance imaging and histologic examination of physeal bars in a rabbit model. J Pediatr Orthop 30:928–935
19. Shapiro F (1982) Epiphyseal growth plate fracture-separations: a pathophysiologic approach. Orthopedics 5:720–736
20. Widni EE, Hausbrandt P, Kraitsy K, Deutsch A, Höllwarth ME, Weinberg AM (2010) Physeal bone bridge formation after transphyseal lesion relapses endochondral ossification. In: Proceedings of the 77th AAOS annual meeting, New Orleans, p 143
21. Padhani AR (2002) Dynamic contrast-enhanced MRI in clinical oncology: current status and future directions. J Magn Reson Imaging 16:407–422
22. Neeman M (2000) Preclinical MRI experience in imaging angiogenesis. Cancer Metastasis Rev 19:39–43
23. Gillies RJ, Bhujwalla ZM, Evelhoch J, Garwood M, Neema M, Robinson SP, Sotak CH, Van Der Sanden B (2000) Applications of magnetic resonance in model systems: tumor biology and physiology. Neoplasia 2:139–151
24. Tofts PS, Brix G, Buckley DL, Evelhoch JL, Henderson E, Knopp MV, Larsson HB, Lee T-Y, Mayr NA, Parker GJ, Port RE, Taylor J, Weisskoff RM (1999) Estimating kinetic parameters from dynamic contrast-enhanced T1-weighted MRI of a diffusable tracer: standardized quantities and symbols. J Magn Reson Imaging 10:223–232
25. Ashton E, Raunig D, Ng C, Kelcz F, McShane T, Evelhoch J (2008) Scan-rescan variability in perfusion assessment of tumors in MRI using both model and data-derived arterial input functions. J Magn Reson Imaging 28:791–796
26. Jackson A, Buckley DL, Parker GJM (2006) Dynamic contrast-enhanced magnetic resonance imaging in oncology. Springer, Berlin
27. Yankeelov TE, Gore JC (2009) Dynamic contrast enhanced magnetic resonance imaging in oncology: theory, data acquisition, analysis, and examples. Curr Med Imaging Rev 3:91–107
28. Port RE, Knopp MV, Brix G (2001) Dynamic contrast-enhanced MRI using Gd-DTPA: interindividual variability of the arterial input function and consequences for the assessment of kinetics in tumors. Magn Reson Med 45:1030–1038
29. Wang Y, Huang W, Panicek DM, Schwartz LH, Koutcher JA (2008) Feasibility of using limited-population-based arterial input function for pharmacokinetic modeling of osteosarcoma dynamic contrast-enhanced MRI data. Magn Reson Med 59:1183–1189
30. Li X, Welch EB, Arlinghaus LR, Chakravarthy AB, Xu L, Farley J, Loveless ME, Mayer IA, Kelley MC, Meszoely IM et al (2011) A novel AIF tracking method and comparison of DCE-MRI parameters using individual and population-based AIFs in human breast cancer. Phys Med Biol 56:5753–5769
31. McGrath DM, Bradley DP, Tessier JL, Lacey T, Taylor CJ, Parker GJ (2009) Comparison of model-based arterial input functions for dynamic contrast-enhanced MRI in tumor bearing rats. Magn Reson Med 61:1173–1184
32. Kovar DA, Lewis M, Karczmar GS (1998) A new method for imaging perfusion and contrast extraction fraction: input functions derived from reference tissues. J Magn Reson Imaging 8:1126–1134
33. Yankeelov TE, Luci JJ, Lepage M, Li R, Debusk L, Lin PC, Price RR, Gore JC (2005) Quantitative pharmacokinetic analysis of DCE-MRI data without an arterial input function: a reference region model. Magn Reson Imaging 23:519–529
34. Lee MA, Nissen TP, Otsuka NY (2000) Utilization of a murine model to investigate the molecular process of transphyseal bone formation. J Pediatr Orthop 20:802–806
35. Hittmair K, Gomiscek G, Langenberger K, Recht M, Imhof H, Kramer J (1994) Method for the quantitative assessment of

contrast agent uptake in dynamic contrast-enhanced MRI. Magn Reson Med 31:567–571
36. Merwa R, Reishofer G, Feiweier T, Kapp K, Ebner F, Stollberger R (2009) Impact of B1 inhomogeneities on AIF selection in DCE-MRI at 3 Tesla. In: Proceedings of the 17th scientific meeting, international society for magnetic resonance in medicine, Honolulu, p 4661
37. Yankeelov TE, Luci JJ, DeBusk LM, Lin PC, Gore JC (2008) Incorporating the effects of transcytolemmal water exchange in a reference region model for DCE-MRI analysis: theory, simulations, and experimental results. Magn Reson Med 59:326–335
38. Landis CS, Li X, Telang FW, Molina PE, Palyka I, Vetek G, Springer CS (1999) Equilibrium transcytolemmal water-exchange kinetics in skeletal muscle in vivo. Magn Reson Med 42:467–478
39. Buckley DL, Kershaw LE, Stanisz GJ (2008) Cellular-interstitial water exchange and its effect on the determination of contrast agent concentration in vivo: dynamic contrast-enhanced MRI of human internal obturator muscle. Magn Reson Med 60:1011–1019
40. Ferrara N, Gerber H-P, LeCouter J (2003) The biology of VEGF and its receptors. Nat Med 9:669–676
41. Andersen CL, Jensen JL, Ørntoft TF (2004) Normalization of real-time quantitative reverse transcription-PCR data: a model-based variance estimation approach to identify genes suited for normalization, applied to bladder and colon cancer data sets. Cancer Res 64:5245–5250
42. Taha MA, Manske SL, Kristensen E, Taiani JT, Krawetz R, Wu Y, Ponjevic D, Matyas JR, Boyd SK, Rancourt DE, Dunn JF (2013) Assessment of the efficacy of MRI for detection of changes in bone morphology in a mouse model of bone injury. J Magn Reson Imaging 38:231–237
43. Donahue KM, Weisskoff RM, Parmelee DJ, Callahan RJ, Wilkinson RA, Mandeville JB, Rosen BR (1995) Dynamic Gd-DTPA enhanced MRI measurement of tissue cell volume fraction. Magn Reson Med 34:423–432
44. Yankeelov TE, Rooney WD, Li X, Springer CS (2003) Variation of the relaxographic "shutter-speed" for transcytolemmal water exchange affects the CR bolus-tracking curve shape. Magn Reson Med 50:1151–1169
45. Yankeelov TE, Cron GO, Addison CL, Wallace JC, Wilkins RC, Pappas BA, Santyr GE, Gore JC (2007) Comparison of a reference region model with direct measurement of an AIF in the analysis of DCE-MRI data. Magn Reson Med 57:353–361
46. Shweiki D, Itin A, Soffer D, Keshet E (1992) Vascular endothelial growth factor induced by hypoxia may mediate hypoxia-initiated angiogenesis. Nature 359:843–845
47. Forsythe JA, Jiang BH, Iyer NV, Agani F, Leung SW, Koos RD, Semenza GL (1996) Activation of vascular endothelial growth factor gene transcription by hypoxia-inducible factor 1. Mol Cell Biol 16(9):4604–4613
48. Weidemann A, Johnson RS (2008) Biology of HIF-1alpha. Cell Death Differ 15(4):621–627
49. Kim HKW, Wiesman KD, Kulkarni V, Burgess J, Chen E, Brabham C, Ikram H, Du J, Lu A, Kulkarni AV, Dempsey M, Herring JA (2014) Perfusion MRI in early stage of Legg-Calvé-Perthes disease to predict lateral pillar involvement. J Bone Joint Surg Am 96(14):1152–1160
50. Quinn R (2005) Comparing rat's to human's age: how old is my rat in people years? Nutrition 21:775–777
51. Andreollo NA, dos Santos EF, Araújo MR, Lopes LR (2012) Rat's age versus human's age: what is the relationship? Arq Bras Cir Dig 25:49–51

# 2.3 Reproducibility of Relaxometry of Human Lumbar Vertebrae at 3 Tesla Using $^{1}$H MR Spectroscopy

[164] Neumayer B., Widek T., Stollberger R., and Scheurer E. "Reproducibility of Relaxometry of Human Lumbar Vertebrae at 3 Tesla Using $^{1}$H MR Spectroscopy." In: *Journal of Magnetic Resonance Imaging* (Dec. 2017). DOI: 10.1002/jmri.25912

## 2.3.1 Summary

The NMR spectrum of normal bone marrow mainly consists of fat and water signal which relate to its fatty (yellow) and hematopoietic (red) components. The ratio of these components depends on age due to a well-established conversion of red to yellow bone marrow [138]. This age-related change was shown for various body regions using MR imaging [139–143] and for human lumbar vertebrae using MR spectroscopy (MRS) [145, 146, 148, 165]. Furthermore, the percentage fat fraction (FF) was shown to be connected to bone mineral density [166], osteoporosis [167], and abdominal adipose tissue [168].

The fat component of a $^{1}$H NMR spectrum of a lumbar vertebra consists of various peaks. Therefore, a simple analysis of peak values of the water peak and the main fat peak may be error prone causing either an underestimation of the complete fat component, or – if only the main fat peak is of interest – an overestimation due to peak overlaps [165].
It was shown that $T_2$ of the water compartment ($T_{2,w}$) is significantly shorter than that of fat in lumbar vertebrae [169], and therefore it is important to note that a correction of the influence of $T_2$ was either omitted or performed using average values in the above-mentioned MRS-based studies. Besides the difference between the two compartments, $T_{2,w}$ is very short in general. Therefore, the minimum achievable echo time $T_E$ for clinical MR scanners can also influence the accuracy of the determination of the fat fraction. The need for $T_2$ correction of MR spectra of human lumbar vertebrae has been shown recently [59].

The relaxation times in both fat and water compartments as well as the fat fraction corrected for relaxation decay were determined for vertebrae L2 and L3 at 3 Tesla using MR spectroscopy. The results derived from repeated measurements were analysed for intra-individual variability. Furthermore, the error introduced by omitting the correction for relaxation was determined.

### 2.3.2 Author Contribution

In this study Bernhard Neumayer was responsible for study design, data analysis and the final publication of the results. Protocols for MR measurements were defined by Bernhard Neumayer in collaboration with Chris Boesch, MD, PhD (Inselspital Bern, AMSM, Bern, Switzerland). Bernhard Neumayer was furthermore involved in MR data collection and performed spectral fits, parameter identification and statistical analyses. The manuscript was mainly written by Bernhard Neumayer.

# Reproducibility of Relaxometry of Human Lumbar Vertebrae at 3 Tesla Using $^1$H MR Spectroscopy

Bernhard Neumayer, MSc,[1,2]* Thomas Widek, MSc,[1,2] Rudolf Stollberger, PhD,[2,3] and Eva Scheurer, MD, MSc[4]

**Background:** MR spectroscopy is widely used for fat fraction quantification of human lumbar vertebrae. However, the measurements need to be corrected for relaxation effects.
**Purpose:** The aim of this study was to determine the reproducibility of relaxometry in human lumbar vertebrae required for the correction of fat fraction measurements using magnetic resonance spectroscopy at 3 Tesla. Such information provides error estimates and guidance regarding reliability for future studies.
**Study Type:** Prospective.
**Subjects:** Forty-six healthy volunteers (22 female [f], 24 male [m]) participated in this study.
**Field Strength:** All subjects underwent three consecutive multi-$T_E$/multi-$T_R$ MR spectroscopy measurements at 3 Tesla.
**Assessment:** A total of 2580 spectra of lumbar vertebrae L2 and L3 of 43 subjects (21f, 22m) were quantified using jMRUI software. Data were exported and mono-exponential fits were applied to the signals of water and fat compartments to derive relaxation times and calculate the fat fraction corrected for relaxation effects. Finally, relaxation times and fat fraction results of repeated measurements were analyzed for reproducibility.
**Statistical Tests:** Reproducibility was evaluated by calculating the coefficient of variation (CV). Influences of volunteer age and sex were tested by analysis of covariance.
**Results:** The CV for all calculated parameters ranged between 1.22% ($T_2$ of the fat compartment) and 3.02% ($T_1$ of the fat compartment). Relaxation times and fat fraction were statistically different for female and male volunteers ($P < 0.01$) and relaxation times of the water compartment showed significant ($P < 0.01$) correlation with the fat fraction.
**Data Conclusion:** Based on repeated acquisitions using the measurement parameters applied in this study, magnetic resonance spectroscopy allowed a reproducible calculation of the fat fraction corrected for relaxation effects. $T_1$ of the water compartment showed high reproducibility and correlation with the fat fraction. It, therefore, might be considered as a parameter linked to the composition of the water compartment and patient health.
**Level of Evidence:** 1
**Technical Efficacy:** Stage 1

J. MAGN. RESON. IMAGING 2017;00:000–000.

The NMR spectrum of normal bone marrow mainly consists of fat and water signals which relate to its fatty (yellow) and hematopoietic (red) components. The ratio of these components depends on age due to a well-established conversion of red to yellow bone marrow over the years.[1] This age-related change has previously been shown for various anatomical regions using MR imaging[2–6] and for human lumbar vertebrae using MR spectroscopy (MRS).[7–10] Furthermore, fat fraction (FF) has been shown to be connected to bone mineral density,[11,12] osteoporosis,[13] and abdominal adipose tissue.[14]

The dependence of the fat fraction on gender is yet to be fully determined.[15] Several authors[7,8,16] reported a significant difference between female and male subjects using MRS. However, some imaging studies confirm[17–20] as well as refute[4,21,22] gender-related differences. A plausible explanation for these differences may be offered by the differences in the applied measurement methods.[23]

View this article online at wileyonlinelibrary.com. DOI: 10.1002/jmri.25912

Received Jul 14, 2017, Accepted for publication Nov 14, 2017.

*Address reprint requests to: B. N., Ludwig Boltzmann Institute for Clinical Forensic Imaging, Universitätsplatz 4, 8010 Graz, Austria. E-mail: bernhard.neumayer@cfi.lbg.ac.at

From the [1]Ludwig Boltzmann Institute for Clinical Forensic Imaging, Graz, Austria; [2]BioTechMed-Graz, Austria; [3]Institute of Medical Engineering, Graz University of Technology, Graz, Austria; and [4]Institute of Forensic Medicine, University of Basel, Basel, Switzerland

 

The fat component of a $^1$H NMR spectrum of a lumbar vertebra consists of various peaks. Therefore, a simple analysis of signal amplitudes of the water peak and the main fat peak may be error prone causing either an underestimation of the complete fat component, or, if only the main fat peak is of interest, an overestimation due to overlapping peaks.[9]

Considering this, the data of existing work cannot easily be compared: Schellinger et al (8) mainly examined patients with back pain and determined the lipid water ratio using both signal amplitude and area values by charting the water area and subtracting it from the total area to determine the fat part. Kugel et al[7] examined healthy volunteers and determined the signal intensity in a spectrum by plain integration and correcting all results for $T_2$ decay using an average $T_2$ for all patients. Griffith et al[16] examined healthy subjects and focused on an older age range that was not covered by Kugel et al; however, the fat fraction was calculated using signal amplitudes and was not corrected for signal decay. The findings of this study showed an inverse behavior compared with previous work: the fat fraction in women was significantly higher than that in men.

Considering that the $T_2$ of the water compartment ($T_{2,w}$) is much shorter than that of fat ($T_{2,f}$) in lumbar vertebrae,[24] it is noteworthy that a correction of the influence of $T_2$ was either omitted or performed using average values in the above-mentioned MRS-based studies. Additionally, $T_{2,w}$ is very short in general, which means that limitations of the minimum achievable echo time $T_E$ for clinical MR scanners can also influence the accuracy of the determination of the fat fraction. The need for $T_2$ correction of MR spectra of human lumbar vertebrae has also been shown in a recent study.[25]

The correction of $T_2$ effects depends on the accuracy and reproducibility of the method used to determine the respective relaxation times of the water and the fat compartments. The reproducibility of fat content quantification of bone marrow based on repeated MRS acquisitions at 3 Tesla has already been investigated[9,26]; however, the correction for relaxation effects and the determination of the relaxation-corrected fat fraction has not been examined.

The main aim of this study was to investigate the relaxation times in both fat and water compartments of vertebrae L2 and L3, and to consequently determine the reproducibility of fat fraction calculations when correcting for relaxation decay at 3 Tesla. The intra-individual variability of relaxation times and fat fraction values resulting from repeated measurements as well as the error introduced by omitting the correction for relaxation were analyzed.

## Materials and Methods

### Study Design

The study was performed in accordance with the Declaration of Helsinki and was approved by the ethical committee of the local medical university. All eligible volunteering participants provided written informed consent.

### Subjects

Forty-six healthy volunteers (22 female [f], age: $27.08 \pm 5.32$ years; 24 male [m], age: $31.08 \pm 5.67$ years) participated in this study. All subjects had no history of bone disease or vertebral abnormalities and had not received any drugs reported to alter or affect the bone marrow.

### MR Measurements

All subjects were examined in supine position on a clinical 3T MR scanner (Trio [30 volunteers: 8f, 22m / Prisma [16 volunteers: 14f, 2m], Siemens Healthineers, Erlangen, Germany) using the spine coil and a surface coil. Before spectroscopy, scout images were acquired in sagittal, coronal, and transverse plane. The volume of interest for spectroscopy was positioned in the center of vertebral bodies L2 and L3 subsequently for $^1$H-MRS using STEAM (stimulated echo acquisition mode) sequences with the following parameters: voxel size $20 \times 20 \times 20\,mm^3$ (reduced if necessary); $T_E/T_R = 20, 40, 60, 80, 100/5000$ ms for $T_2$ determination and $T_E/T_R = 20/600, 1000, 2000, 3000, 10000$ ms for $T_1$ determination; band width = 2000 Hz; averages = 10; $T_M = 10$ ms to minimize J coupling effects; no water suppression; no regional saturation bands.

Each examination included patient positioning, measurement and removal from scanner. This procedure was performed three times in total for each subject. All three measurements and patient positioning took approximately 1 h and 45 min. All data of each volunteer were acquired on the same MR system.

### Spectral Fitting and Data Analysis

Spectra were analyzed in the time-frequency domain using jMRUI software[27] and the AMARES algorithm.[28] Five resonances were identified in the acquired spectra: $CH_3$ (0.9 ppm), $CH_2$ (1.3 ppm), $CH_2CH=CH$ (2.0 ppm), water (4.7 ppm), and $CH=CH$ (5.3 ppm). These five peaks were included in the AMARES algorithm. Peak fitting for the resonances of water and $CH_2$ was achieved by combination of Gaussian and Lorentzian lines to account for the non-Lorentzian shape of the peaks; the resonance frequencies and weightings of the individual lines of these combinations were fixed relative to each other to avoid a fit to neighboring resonances. For the remaining resonances, line widths and resonance frequencies were constrained relative to either the water or $CH_2$ peak; amplitude estimation remained unconstrained.

The spectral fits were exported to MATLAB (R2014b, The MathWorks Inc., Natick, MA) for the correction of $T_1$ and $T_2$ effects. The fat component $I_{fat}$ was calculated as the sum of all resonances except the water component $I_{water}$. The results for fat and water were then separately fit to the signal equation

$$I = I_0 \cdot \left(1 - e^{-\frac{T_R}{T_1}}\right) e^{-\frac{T_E}{T_2}} \quad (1)$$

to calculate relaxation times, $T_1$ and $T_2$, as well as the respective proton density-related value $I_0$. The influence of J coupling on the fat signal was neglected.[29] The fat fraction was then calculated by

$$FF = \frac{I_{0,fat}}{I_{0,water} + I_{0,fat}} \quad (2)$$

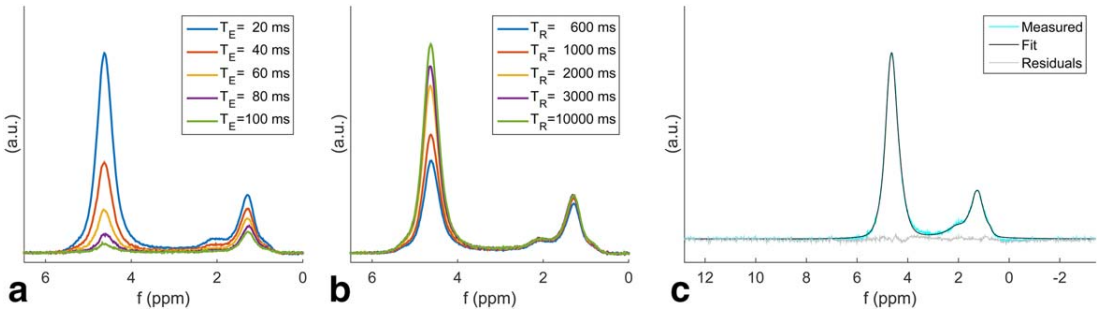


**FIGURE 1: Complete data set acquired for one vertebra. (a) Spectra acquired with 5 different values of $T_E$. (b) Spectra acquired with 5 different values of $T_R$. (c) Spectrum acquired with $T_E/T_R = 20$ ms/5000 ms and corresponding data fit and fit residuals.**

to derive a fat fraction value corrected for $T_1$ and $T_2$ decay (see Fig. 2 for a graphical depiction of the fitting procedure and the calculation of the fat fraction).

Additionally, relaxation time estimates for individual fat components were calculated by applying Eq. [1] to averaged data. The averaging was performed by normalizing the data of each measurement using the last data point ($T_E/T_R = 20$ ms/10000 ms) and calculating the median of all measurements for each component to reduce the influence of outliers.

### *Statistical Analysis*

Reproducibility of relaxometry was determined by comparing the results of the three repeated measurements of one vertebra to their respective mean value. Data were normalized by subtraction of the corresponding mean value to produce a distribution around zero for all measurements. The standard deviation $\sigma$ of this quantity served as a measure for reproducibility and was calculated absolutely ($\sigma_{abs}$) and relatively. For the relative measure, the coefficient of variation (CV) was calculated by dividing $\sigma_{abs}$ by the respective mean value. This analysis was applied to relaxation times $T_1$ and $T_2$ of the water ($T_{1,w}$, $T_{2,w}$) and the fat compartment ($T_{1,f}$, $T_{2,f}$). Additionally, the fat fraction (FF) and an uncorrected $T_2$-weighted fat fraction ($FF_{uncorr}$), which was calculated using only spectra acquired with the shortest available echo time ($T_E/T_R = 20/5000$ ms) and applying Eq. [2], were also compared to evaluate the error introduced by omitting relaxation correction (see Fig. 2). This comparison provided a distribution around a nonzero mean value, which is a measure for the error

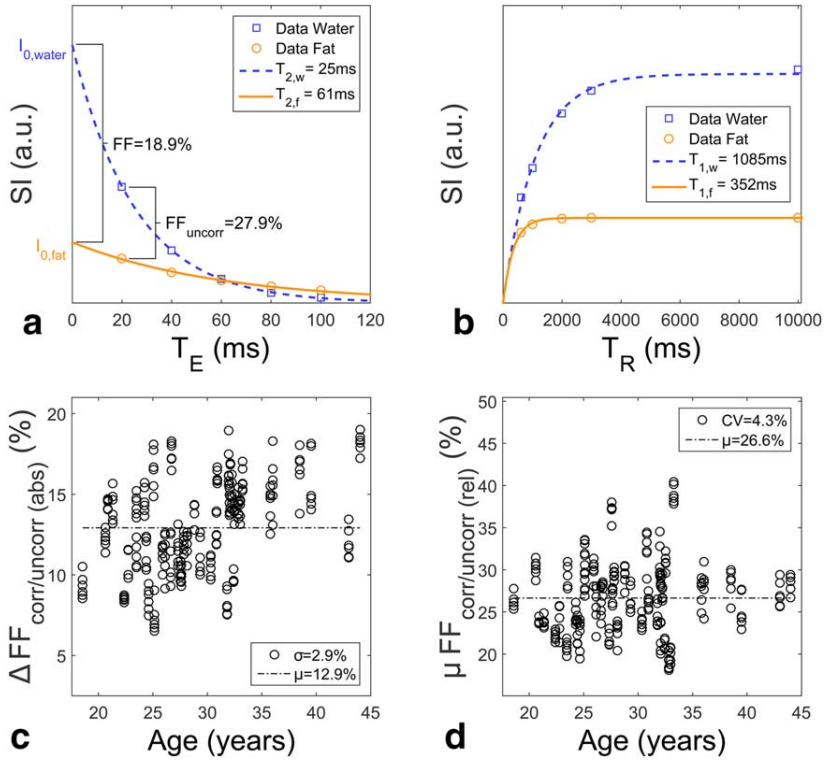


**FIGURE 2: a–d: Exemplary fits of relaxation times (a,b) and comparison of corrected (FF) and uncorrected ($FF_{uncorr}$) fat fraction (c,d). (a) and (b) show data points for the water and fat compartments derived from the data set shown in Figure 1 and the corresponding data fits. Additionally, data points used for the calculations of FF and $FF_{uncorr}$ and their respective results are shown. (c) Absolute deviations of $FF_{uncorr}$ values from the corresponding mean of FF. (d) Relative deviations compared with the corresponding mean value.**

**TABLE 1. Reproducibility of Relaxometry and Fat Fraction Determination**

| | $T_{1,w}$ | $T_{2,w}$ | $T_{1,f}$ | $T_{2,f}$ | FF | $FF_{uncorr}$ | $FF_{corr/uncorr}$ |
|---|---|---|---|---|---|---|---|
| $\sigma_{abs}$ | 20 ms | 0.7 ms | 11 ms | 0.7 ms | 0.7% | 0.7% | 2.9% ($\mu = 12.92\%$) |
| CV | 2.0% | 3.0% | 3.0% | 1.2% | 1.9% | 1.4% | 4.3% ($\mu = 26.65\%$) |

introduced by omitting the correction of relaxation effects for fat fraction analysis.

Correlations between fat fraction and relaxation times were analyzed by performing linear regression and calculating the Pearson correlation coefficient (Pearson's *r*). Potential influences related to volunteer age and sex were analyzed applying analysis of covariance (ANCOVA) with separate lines. Significance was assumed for a *P*-value of $< 0.05$. Reproducibility values were determined using the data of both vertebrae of all volunteers. Correlations between calculated parameters were determined using mean values of three associated measurements to avoid an influence of increased number of data points on the statistics.

## Results

Data of one female and two male volunteers were excluded due to distorted spectra leading to age distributions of $27.32 \pm 5.32$ and $30.84 \pm 5.87$ years for female and male subjects, respectively. This resulted in 43 volunteers and 2580 MR spectra, which could be analyzed in this study.

Figure 1 shows a complete set of spectra acquired for one vertebra. Figure 1a shows spectra acquired for the 5 different echo times and Figure 1b the spectra for the five different repetition times as described in the Materials and Methods section above. Figure 1c shows a data fit for a spectrum acquired with $T_E/T_R = 20$ ms/5000 ms.

An exemplary fit of relaxation curves and the comparison of FF and $FF_{uncorr}$ are presented in Figure 2; Table 1 lists all results in detail. The comparison of corrected and uncorrected fat fraction values yields a CV of 4.3%. The average error of absolute fat fraction determination without correction for relaxation was 12.9%, which corresponds to a relative error of 26.7% when compared with the respective mean value of the corrected fat fraction.

**TABLE 2. Pearson's *r* for Correlations Between Corrected Fat Fraction and Relaxation Times[a]**

| | $T_{1,w}$ | | | $T_{2,w}$ | | |
|---|---|---|---|---|---|---|
| | All | L2 | L3 | All | L2 | L3 |
| $FF_{All}$ | −0.53 | −0.51 | −0.53 | −0.47 | −0.46 | −0.48 |
| $FF_{Female}$ | −0.40 | −0.36 | −0.43 | −0.49 | −0.51 | −0.46 |
| $FF_{Male}$ | −0.72 | −0.68 | −0.76 | −0.37 | −0.33 | −0.41 |

[a]All correlations significant with $P < 0.01$.

Table 2 shows the correlation between fat fraction and relaxation times $T_{1,w}$ and $T_{2,w}$. The relaxation times of the water compartment show strong correlation with the fat fraction. ANCOVA showed significant differences between female and male volunteers ($P < 0.001$) and confirmed significantly different slopes for $T_{2,w}$ ($P < 0.05$). $T_{2,f}$ showed a weak correlation only for male volunteers and $T_{1,f}$ did not show any significant relationship with the fat fraction; therefore, these values are not listed in Table 2.

Detailed results for relaxation times and fat fraction are shown in Table 3 and relaxation time changes with volunteer age are presented in Figure 3. Relaxation times $T_{1,w}$, $T_{2,w}$, and $T_{2,f}$ ($P < 0.001$) and fat fractions ($P < 0.05$) were significantly different between female and male volunteers. Significant age-related changes were observed for the $T_2$ compartments in male volunteers and the correlation lines in Figure 3 show a decrease of 1.6 ms and 2.6 ms per decade for $T_{2,w}$ and $T_{2,f}$, respectively. However, ANCOVA only confirmed significantly different slopes for $T_{2,f}$ ($P < 0.05$).

The longest $T_1$ values in a cohort are of interest to estimate the maximum $T_1$-weighting that may influence fat fraction calculations. Largest $T_1$ values occurred for the water compartment and were 1389 ms and 1100 ms for female and male volunteers, respectively. Assuming monoexponential longitudinal relaxation and a repetition time of $T_R = 3000$ ms, the amplitude of the water compartment signal is reduced by 7.4% and 4.6% for female and male subjects, respectively, when assuming the average $T_1$ values reported in Table 3. For the maximum $T_1$ value in female subjects, the reduction of the water signal rises to 11.5% (6.5% for male subjects), potentially leading to an overestimation of the fat fraction in female volunteers. For a repetition time of $T_R = 5000$ ms, the longest $T_1$ leads to a signal decrease of 2.7%.

Relaxation times for individual fat components were $T_2/T_1 = 75$ ms/355 ms for $CH_2$, $T_2/T_1 = 63$ ms/601 ms for CH3, $T_2/T_1 = 34$ ms/377 ms for $CH_2CH{=}CH$ and $T_2/T_1 = 66$ ms/515 ms for $CH{=}CH$.

## Discussion

The presented results demonstrate the high reproducibility of relaxometry in human lumbar vertebrae, which is important for the calculation of the fat fraction corrected for

**TABLE 3. Mean Values and SDs for Determined Relaxation Times and Corrected Fat Fractions**

| | $T_{1,w}$ (ms) | $T_{2,w}$ (ms) | $T_{1,f}$ (ms) | $T_{2,f}$ (ms) | FF (%) |
|---|---|---|---|---|---|
| $\mu_{All}$ | 1061 | 23 | 368 | 58 | 36.4 |
| $\sigma_{All}$ | 113 | 3.1 | 12 | 3.1 | 10.0 |
| $\mu_{female}$ | 1154 | 25 | 370 | 60 | 33.6 |
| $\sigma_{female}$ | 82 | 2.4 | 12 | 2.0 | 7.9 |
| $\mu_{male}$ | 973 | 21 | 367 | 57 | 39.1 |
| $\sigma_{male}$ | 50 | 1.7 | 13 | 3.3 | 11.0 |

relaxation times. For the applied measurement parameters, the maximum CV was 3.02%, which occurred for $T_1$ of the fat component, $T_{1,f}$; the maximum absolute error was 20 ms, which occurred for $T_1$ of the water compartment, $T_{1,w}$, and is tantamount to a CV of 1.97% due to the long $T_1$ values of lumbar vertebrae.

The high reproducibility of relaxometry is also reflected in the high agreement of the results of fat fraction determination. The values of $\sigma_{abs}$ demonstrate no determinable differences between reproducibility for the corrected fat fraction, FF, and for the uncorrected fat fraction, $FF_{uncorr}$. The CV of 1.91% for the reproducibility of FF is comparable to that reported by Li et al[9] for vertebrae L2 and L3 (1.9% and 2.0%, respectively), who did not correct for relaxation effects, and the value for $FF_{uncorr}$ is even smaller. This difference can mainly be explained by the long $T_E$ of 37 ms Li et al applied, using a point resolved spectroscopy (PRESS) sequence. The short $T_2$ of the water compartment will lead to a strongly decreased water signal for this echo time value and signal noise will have considerable effect on the calculated fat fraction. Ultimately, the observed differences between FF and $FF_{uncorr}$ (e.g., high values corresponding to average error and CV) emphasize the need for relaxation correction, a fact also recently highlighted in Dieckmeyer et al.[25]

We were able to reproduce a negative association between $T_{2,w}$ and the fat fraction as reported by Dieckmeyer et al[25] for women; however, we also observed the same findings in men and additionally identified a correlation between $T_{1,w}$ and FF. The negative association between $T_{1,w}$ and FF thereby is comparable to that reported for brown adipose tissue.[30] It is noteworthy that for female subjects $T_{2,w}$ shows higher correlation while for male volunteers $T_{1,w}$ exhibits a stronger negative trend with increasing fat fraction. Dieckmeyer et al suggested $T_{2,w}$ to be a useful parameter linked to the water compartment composition. Considering the higher reproducibility of $T_{1,w}$ compared with $T_{2,w}$, $T_{1,w}$ may be better suited for the assessment of the state of the water compartment.

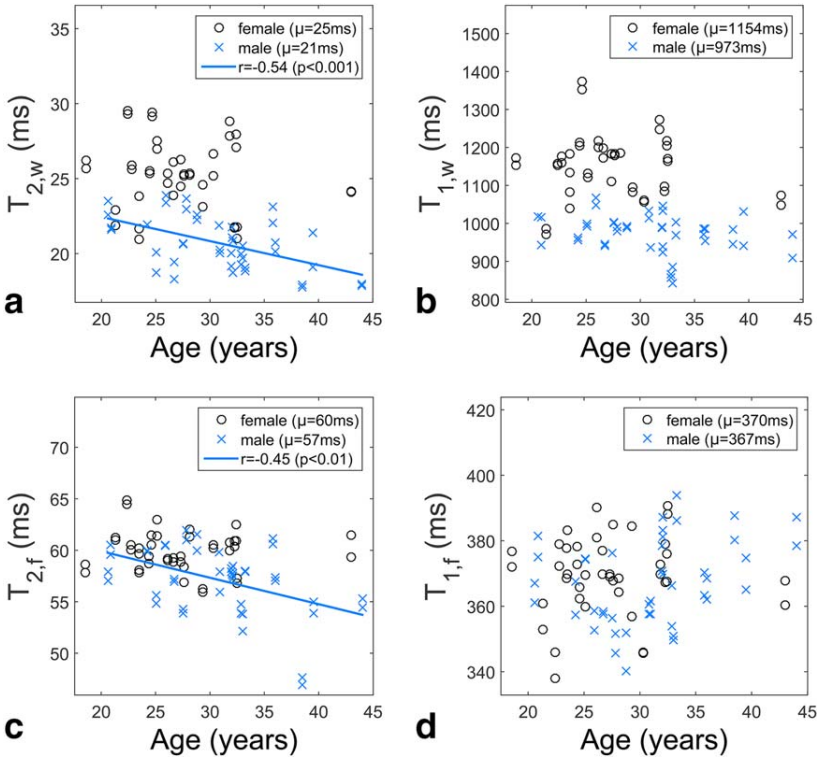


**FIGURE 3: a–d: Changes in relaxation times $T_{2,w}$ (a), $T_{1,w}$ (b), $T_{2,f}$, (c), and $T_{1,f}$ (d) with volunteer age. Correlation lines are only shown for statistically significant changes.**

The relaxation times reported in this work identify differences between female and male volunteers and indicate changes associated with age. Such information can consequently be used to avoid potential problems in studies on lumbar vertebrae. Changes in $T_{2,w}$ and $T_{2,f}$ with volunteer age for male subjects once more emphasize the need for $T_2$ correction for these kinds of studies. Furthermore, the smallest echo time of $T_E = 20$ ms was adequate for reproducible $T_{2,w}$ fits. Nevertheless, even shorter echo times may enable a more accurate parameter identification. Concerning $T_1$, a repetition time of 5000 ms as used in this study can sufficiently avoid $T_1$-weighting of the measurements. It was shown that for the $T_1$ values determined in this study, a $T_R$ of 3000 ms would have a notable effect on fat fraction calculations as the amplitude of the water compartment signal is reduced. This $T_1$-weighting in combination with long relaxation times reported for lumbar vertebrae at 1.5T[31] and the stronger decrease of $T_{2,f}$ with age compared with $T_{2,w}$ may even explain the reversal of the sex difference reported by Griffith et al.[16] However, the correlation of $T_2$ with age needs to be verified with additional data of older volunteers.

The pronounced variation in $T_{1,w}$, especially in women, suggests, that using average values for correcting relaxation effects may be inadequate for this parameter. For transverse relaxation times, the variation is smaller; however, because $T_{2,w}$ is particularly short and additionally appears to be decreasing with age, a correction using average values is potentially error prone and unadvisable.

A limitation of this study is the assumption of common relaxation times for all fat peaks of a volunteer. The fitting of individual relaxation times is in principle possible as we did not constrain peaks to certain ratios of other peaks but the assumption of a common relaxation time was necessary to maintain a stable fitting. A fitting of individual relaxation times leads to high variations in the results especially for small peaks and a coupling to the main peak for calculations is expected to provide a more accurate result instead. Generally, different relaxation times can be expected for individual fat peaks, which was also suggested by estimates provided in this study; however, for STEAM sequences it was shown that the difference between using the sum of all peaks for $T_2$ correction and $T_2$ correction of individual peaks is negligible for fat fraction calculations.[29] Concerning $T_1$, the minimum $T_R$ used in this study may be too long to reliably identify differences in $T_{1,f}$, which most probably explains the small variation of $T_{1,f}$ over all volunteers.

Furthermore, analysis of reproducibility requires changing conditions between measurements. For this study this was achieved by removing the subjects from the scanner after the acquisition of an entire protocol and a new registration for the following measurements; a more generalized approach could also include acquisitions on different scanners. In addition, this study only included healthy volunteers. We expect our method to be applicable to clinical patients; however, a considerable $T_2$ shortening due to a medical condition could require shorter echo times.

Besides these limitations, the number of female and male volunteers was almost identical and the covered age range is comparable for both groups, so that we expect the differences between these groups to be representative and reproducible for larger numbers of volunteers.

In conclusion, the high reproducibility of relaxometry of human lumbar vertebrae presented in this study enabled a stable correction of the fat fraction to derive a value not weighted by either $T_2$ or $T_1$. At 3 Tesla, the minimum echo time of a multi-$T_E$ MRS measurement should be 20 ms or shorter to allow reliable determination of the short $T_2$ of the water compartment. To avoid a $T_1$-weighting of the measurements, a $T_R$ of at least 5000 ms is recommended due to the long $T_1$ of the water compartment. Furthermore, $T_{1,w}$ shows high reproducibility and correlation with the fat fraction, indicating it may serve as a parameter linked to patient health in the future.

## Acknowledgments

The authors thank Chris Boesch, MD, PhD (Inselspital Bern, AMSM, Bern, Switzerland) for his support in designing this study and evaluating spectral fit quality and Bridgette Webb for a critical review of the manuscript. *Ethical Approval*: All procedures performed in studies involving human participants were in accordance with the ethical standards of the institutional and/or national research committee and with the 1964 Helsinki declaration and its later amendments or comparable ethical standards. *Informed Consent*: Informed consent was obtained from all individual participants included in the study. *Conflict of Interest*: The authors declare that they have no conflict of interest.

## References

1. Piney A. The anatomy of the bone marrow: with special reference to the distribution of the red marrow. Br Med J 1922;2:792–795.
2. Okada Y, Aoki S, Barkovich AJ, et al. Cranial bone marrow in children: assessment of normal development with MR imaging. Radiology 1989;171:161–164.
3. Moore SG, Dawson KL. Red and yellow marrow in the femur: age-related changes in appearance at MR imaging. Radiology 1990;175: 219–223.
4. Ricci C, Cova M, Kang YS, et al. Normal age-related patterns of cellular and fatty bone marrow distribution in the axial skeleton: MR imaging study. Radiology 1990;177:83–88.
5. Jaramillo D, Laor T, Hoffer FA, et al. Epiphyseal marrow in infancy: MR imaging. Radiology 1991;180:809–812.
6. Dawson KL, Moore SG, Rowland JM. Age-related marrow changes in the pelvis: MR and anatomic findings. Radiology 1992;183:47–51.

7. Kugel H, Jung C, Schulte O, Heindel W. Age- and sex-specific differences in the $^{1}$H-spectrum of vertebral bone marrow. J Magn Reson Imaging 2001;13:263–268.
8. Schellinger D, Lin CS, Fertikh D, et al. Normal lumbar vertebrae: anatomic, age, and sex variance in subjects at proton MR spectroscopy--initial experience. Radiology 2000;215:910–916.
9. Li X, Kuo D, Schafer AL, et al. Quantification of vertebral bone marrow fat content using 3 Tesla MR spectroscopy: reproducibility, vertebral variation, and applications in osteoporosis. J Magn Reson Imaging 2011;33:974–979.
10. Roldan-Valadez E, Piña-Jimenez C, Favila R, Rios C. Gender and age groups interactions in the quantification of bone marrow fat content in lumbar spine using 3T MR spectroscopy: a multivariate analysis of covariance (Mancova). Eur J Radiol 2013;82:e697–e702.
11. Shih TT, Chang C, Hsu C, Wei S, Su K, Chung H. Correlation of bone marrow lipid water content with bone mineral density on the lumbar spine. Spine (Phila Pa 1976) 2004;29:2844–2850.
12. Bredella M, Daley S, Kalra M, Brown J, Miller K, Torriani M. Marrow adipose tissue quantification of the lumbar spine by using dual-energy CT and single-voxel 1H MR spectroscopy: a feasibility study. Radiology 2015;277:230–235.
13. Yeung DKW, Griffith JF, Antonio GE, Lee FKH, Woo J, Leung PC. Osteoporosis is associated with increased marrow fat content and decreased marrow fat unsaturation: a proton MR spectroscopy study. J Magn Reson Imaging 2005;22:279–285.
14. Baum T, Yap SP, Karampinos DC, et al. Does vertebral bone marrow fat content correlate with abdominal adipose tissue, lumbar spine bone mineral density, and blood biomarkers in women with type 2 diabetes mellitus? J Magn Reson Imaging 2012;35:117–124.
15. Liney GP, Bernard CP, Manton DJ, Turnbull LW, Langton CM. Age, gender, and skeletal variation in bone marrow composition: a preliminary study at 3.0 Tesla. J Magn Reson Imaging 2007;26:787–793.
16. Griffith JF, Yeung DKW, Ma HT, Leung JCS, Kwok TCY, Leung PC. Bone marrow fat content in the elderly: a reversal of sex difference seen in younger subjects. J Magn Reson Imaging 2012;36:225–230.
17. Richards MA, Webb JAW, Jewell SE, Gregory WM, Reznek RH. In-vivo measurement of spin lattice relaxation time (T1) of bone marrow in healthy volunteers: the effects of age and sex. Br J Radiol 1988;61:30–33.
18. Duda SH, Laniado M, Schick F, Strayle M, Claussen CD. Normal bone marrow in the sacrum of young adults: differences between the sexes seen on chemical-shift MR imaging. AJR Am J Roentgenol 1995;164:935–940.
19. Ishijima H, Ishizaka H, Horikoshi H, Sakurai M. Water fraction of lumbar vertebral bone marrow estimated from chemical shift misregistration on MR imaging: normal variations with age and sex. AJR Am J Roentgenol 1996;167:355–358.
20. Vande Berg BC, Lecouvet FE, Moysan P, Maldague B, Jamart J, Malghem J. MR assessment of red marrow distribution and composition in the proximal femur: correlation with clinical and laboratory parameters. Skeletal Radiol 1997;26:589–596.
21. Dooms GC, Fisher MR, Hricak H, Richardson M, Crooks LE, Genant HK. Bone marrow imaging: magnetic resonance studies related to age and sex. Radiology 1985;155:429–432.
22. Jenkins JPR, Stehling M, Sivewright G, Hickey DS, Hillier VF, Isherwood I. Quantitative magnetic resonance imaging of vertebral bodies: a T1 and T2 study. Magn Reson Imaging 1989;7:17–23.
23. Vande Berg BC, Lecouvet FE, Malghem J. Sex-related difference in marrow conversion in the proximal femur: does it exist? Radiology 1998;209:587–588.
24. Neumayer B, Petrovic A, Widek T, Boesch C, Scheurer E. Reproducibility of $^{1}$H MR spectroscopy of human lumbar vertebrae at 3 Tesla. In Proceedings of the 30$^{th}$ Annual Meeting of ESMRMB, Toulouse, 2013. (abstract 631).
25. Dieckmeyer M, Ruschke S, Cordes C, et al. The need for T2 correction on MRS-based vertebral bone marrow fat quantification: implications for bone marrow fat fraction age dependence. NMR Biomed 2015;28:432–439.
26. Pansini VM, Monnet A, Salleron J, Penel G, Migaud H, Cotten A. Reproducibility of $^{1}$H MR spectroscopy of hip bone marrow at 3 Tesla. J Magn Reson Imaging 2012;36:1445–1449.
27. Naressi A, Couturier C, Devos JM, et al. Java-based graphical user interface for the MRUI quantitation package. MAGMA 2001;12:141–152.
28. Vanhamme L, van den Boogaart A, Van Huffel S. Improved method for accurate and efficient quantification of MRS data with use of prior knowledge. J Magn Reson 1997;129:35–43.
29. Hamilton G, Middleton MS, Bydder M, et al. Effect of PRESS and STEAM sequences on magnetic resonance spectroscopic liver fat quantification. J Magn Reson Imaging 2009;30:145–152.
30. Hu HH, Nayak KS. Change in the proton T1 of fat and water in mixture. Magn Reson Med 2010;63:494–501.
31. Schick F, Bongers H, Jung W-I, et al. Proton relaxation times in human red bone marrow by volume selective magnetic resonance spectroscopy. Appl Magn Reson 1992;3:947–963.

## 2.4 Reducing Acquisition Time for MRI-Based Forensic Age Estimation

[170] Neumayer B., Schlögl M., Payer C., Widek T., Tschauner S., Ehammer T., Stollberger R., and Urschler M. "Reducing Acquisition Time for MRI-Based Forensic Age Estimation." In: *Scientific Reports* (2018). DOI: 10.1038/s41598-018-20475-1

### 2.4.1 Summary

The topic of age estimation in the living is important for clinical applications [171–173] as well as legal or forensic investigations [174–177]. Current recommendations suggest X-ray-based imaging modalities for age estimation [178]; however, to avoid the application of ionizing radiation, MRI has recently experienced increased interest [175, 179–184]. Further, while for X-ray-based methods a substantial variance of the estimation error was reported when using only a single biological characteristic [185], a recently developed fully automatic method based only on MR images of the left hand and wrist provided promising results in an objective and repeatable manner [133].
A general drawback of MRI is the requirement of considerably longer measurement times compared to radiographs or computed tomography leading to increased examination costs and reduced patient comfort. A reduction of scanning time of MR acquisitions can be achieved with undersampling strategies and to recover artefact-free images from undersampled data, i.e. a reduced amount of data, advanced reconstruction methods have been developed [16–21]. The aim of this study was to investigate the reproducibility of age estimation based on undersampled MR data.

For 15 healthy volunteers MR raw data of the left hand was retrospectively undersampled applying the CAIPIRINHA (Controlled Aliasing In Parallel Imaging Results IN Higher Acceleration) undersampling strategy with varying acceleration factors; image reconstruction was performed using TGV (total generalized variation) [186, 187]. Two radiologists randomly assessed the original images and two sets of images reconstructed from undersampled data applying the method proposed by Greulich and Pyle [130]. Additionally, a neural network-based age estimation method [133] analysed four sets of further undersampled images.

The age estimates derived from undersampled data were compared to the estimates based on original images. The differences were analysed to determine the influence introduced by undersampling and to identify the limits of acceleration applicable to MRI data for age estimation.

### 2.4.2 Author Contribution

Bernhard Neumayer was responsible for concept and design of this study. Furthermore, he conducted the study and evaluated the data. Finally, Bernhard Neumayer was responsible for the publication of the study's results and contributed the main part of the final manuscript.

SCIENTIFIC REPORTS

OPEN

# Reducing acquisition time for MRI-based forensic age estimation

Bernhard Neumayer[1,5], Matthias Schloegl[2,5], Christian Payer[3], Thomas Widek[1,5], Sebastian Tschauner[4], Thomas Ehammer[1], Rudolf Stollberger[2,5] & Martin Urschler[1,3,5]

Received: 23 June 2017
Accepted: 19 January 2018
Published online: 01 February 2018

**Radiology-based estimation of a living person's unknown age has recently attracted increasing attention due to large numbers of undocumented immigrants entering Europe. To avoid the application of X-ray-based imaging techniques, magnetic resonance imaging (MRI) has been suggested as an alternative imaging modality. Unfortunately, MRI requires prolonged acquisition times, which potentially represents an additional stressor for young refugees. To eliminate this shortcoming, we investigated the degree of reduction in acquisition time that still led to reliable age estimates. Two radiologists randomly assessed original images and two sets of retrospectively undersampled data of 15 volunteers (N = 45 data sets) applying an established radiological age estimation method to images of the hand and wrist. Additionally, a neural network-based age estimation method analyzed four sets of further undersampled images from the 15 volunteers (N = 105 data sets). Furthermore, we compared retrospectively undersampled and acquired undersampled data for three volunteers. To assess reliability with increasing degree of undersampling, intra-rater and inter-rater agreement were analyzed computing signed differences and intra-class correlation. While our findings have to be confirmed by a larger prospective study, the results from both radiological and automatic age estimation showed that reliable age estimation was still possible for acquisition times of 15 seconds.**

Age estimation in living individuals is important for clinical applications[1–3] as well as in legal or forensic medicine investigations[4] and sports[5–8], but it is prone to uncertainty caused by the variation of human development[9]. Concerning biological age one can draw insights from comprehensive studies[10,11] but the use of biological development for estimating chronological age, as required in forensic applications, is still a topic of current research[12,13]. Recently, the increased flow of individuals into and across the European Union raised interest in forensic age estimation for children, adolescents and young adults claiming to be minors but lacking valid identification documents[14].

Current multi-factorial age estimation methods are based on a radiograph of the hand, a panoramic X-ray image of the teeth and computed tomography images of the clavicles[15]. To avoid exposure to ionizing radiation, there is growing interest in magnetic resonance imaging (MRI) for forensic age estimation[5,16–23]. This interest has led to developments such as a recently proposed fully automatic machine learning based method[24] based on MR images of the left hand and wrist.

Compared to acquiring radiographs or computed tomography images, MRI has the drawback of considerably longer acquisition times, leading to increased examination costs and reduced patient comfort. Additionally, longer acquisition times are more prone to errors due to motion artefacts when acquiring images of children or adolescents. Therefore, short examination times are highly preferable.

A reduction of MR scanning time can be achieved by leaving out acquisition steps, often termed undersampling. The CAIPIRINHA (Controlled Aliasing In Parallel Imaging Results IN Higher Acceleration) undersampling strategy[25] enables optimized acceleration for 3D image acquisition and is readily available on current MR scanners. To recover artefact-free images from a reduced amount of data, an advanced reconstruction strategy has to be applied. For this task *total generalized variation* (TGV) regularization[26,27] has already demonstrated its applicability in various MRI studies[28–31]. We thus anticipate applicability with a high acceleration potential for volumetric MR data for age estimation by using CAIPIRINHA and TGV.

[1]Ludwig Boltzmann Institute for Clinical Forensic Imaging, Universitätsplatz 4, 8010, Graz, Austria. [2]Institute of Medical Engineering, Graz University of Technology, Stremayrgasse 16, 8010, Graz, Austria. [3]Institute of Computer Graphics and Vision, Graz University of Technology, Inffeldgasse 16, 8010, Graz, Austria. [4]Division of Pediatric Radiology, Department of Radiology, Medical University of Graz, Auenbruggerplatz 34, 8036, Graz, Austria. [5]BioTechMed-Graz, Graz, Austria. Correspondence and requests for materials should be addressed to B.N. (email: bernhard.neumayer@cfi.lbg.ac.at)

| Simulated, n = 15 (13.77y–23.15 y, μ = 16.87 y, σ = 2.41) | | | | |
|---|---|---|---|---|
| **Name** | **AF** | **$t_{Acqu}$** | **Radiological analysis** | **Automatic analysis** |
| $I_{Orig}$ | 1 | 226 s | Yes | Yes |
| $I_{Sim29}$ | 3.89 | 29 s | Yes | Yes |
| $I_{Sim15}$ | 7.49 | 15 s | Yes | Yes |
| $I_{Sim10}$ | 10.84 | 10 s | No | Yes |
| $I_{Sim8}$ | 13.96 | 8 s | No | Yes |
| $I_{Sim7}$ | 16.86 | 7 s | No | Yes |
| $I_{Sim6}$ | 19.58 | 6 s | No | Yes |
| **Acquired, n = 3 (15.75 y, 18.85 y, 21.61 y)** | | | | |
| $I_{Acq28}$ | 4.07 | 28 s | No | No |
| $I_{Acq15}$ | 7.55 | 15 s | No | No |
| $I_{Acq8}$ | 13.63 | 8 s | No | No |

**Table 1.** Overview of acquisition times and acceleration factors for simulated and acquired data. μ: mean, σ: standard deviation, AF: acceleration factor describing speed-up of acquisition time, $t_{Acqu}$: acquisition time.

We conduct this feasibility study to investigate the degree of acceleration that can be applied to hand/wrist MRI for age estimation without significantly influencing the estimation outcome. This aims at determining limits and applicability of the proposed method by comparing the reliability of both human and automated evaluation, reflecting the potential of automatic methods to support radiologists in age estimation tasks.

## Methods

**Ethics Statement and Informed Consent.** The study was performed in accordance with the Declaration of Helsinki and was approved by the ethical committee of the Medical University of Graz (EK 21–399 ex 09/10). All volunteers provided written informed consent. From underage participants written consent from a legal guardian was additionally obtained.

**Subjects.** For this feasibility study 18 healthy male Caucasian volunteers between 13.8 and 23.2 years (mean = 17.2 y, median = 17.0 y) were recruited to acquire three-dimensional MR images of the left hand and wrist. The data of 15 volunteers were used to investigate implications of a reduction in acquisition time on resulting age estimates as described below. The data of the remaining three volunteers (see Table 1) were used to compare retrospectively undersampled images with actually acquired undersampled images.

**MR Image Acquisition.** MRI exams were performed using commercially available clinical 3 T MR scanners (Skyra/Prisma, Siemens Healthineers, Erlangen, Germany) and a conventional 20-channel receive-only head-neck coil (Siemens Healthineers, Erlangen, Germany). Volunteers were placed in prone position with outstretched left arm. The hand was weighted down using a sandbag to minimize movements.

For all 18 subjects $T_1$-weighted 3D FLASH (Fast Low Angle SHot) VIBE (Volumetric Interpolated Breath hold Examination) measurements ($T_E/T_R$/FA = 4.06 ms/14 ms/15°, field-of-view = 129 mm × 230 mm, two averages, acquisition matrix = 129 × 230 and image matrix = 288 × 512, 72 slices) of the left hand and wrist were acquired. The resulting 3D volumes had an image resolution of 0.45 mm × 0.45 mm × 0.90 mm and required an acquisition time of $t_{Acqu}$ = 3:46 minutes. For later comparisons with undersampled data, the images from this fully-sampled data are referred to as *original* images or data.

For three volunteers (see Table 1) *accelerated* measurements were additionally acquired using CAIPIRINHA with 12 calibration lines and acquisition times of 28, 15 and nine seconds.

For a better understanding, an overview of the study design is given in Fig. 1.

**Retrospective Undersampling of MRI Data.** Undersampling MRI raw data is equivalent to not acquiring part of the data, i.e. leaving out data lines during the acquisition. Therefore, retrospectively undersampling conventionally acquired data by removing data lines from the fully-sampled data set *prior to image reconstruction* is a valid reference method to determine specific acceleration potential. The retrospective undersampling of the raw MR data was applied by simulating the commercially available CAIPIRINHA acquisition strategy with minimized noise amplification[32].

For 15 volunteers, the CAIPIRINHA method with 12 calibration lines was applied retrospectively to simulate six different reduced acquisition times ($t_{Acqu}$) between 29 and six seconds (see Table 1) providing a total of 105 data sets. Only non-averaged data were undersampled, which additionally reduced the required acquisition time by a factor of two, compared to the standard setting of performing two averages. In order to reduce the computational burden, the multi-channel data were reduced to a lower number of virtual coils via coil compression[33]. The virtual coil sensitivities were then estimated from the calibration data with the ESPIRiT method[34]. Image reconstruction was carried out for all simulated acceleration factors (AF) using the TGV method[27], which considers smooth tissue variations and uses a dedicated optimization algorithm[35] adapted for parallel computing. When comparing images reconstructed from retrospectively undersampled data to original images they will be referred to as *simulated* images or data.

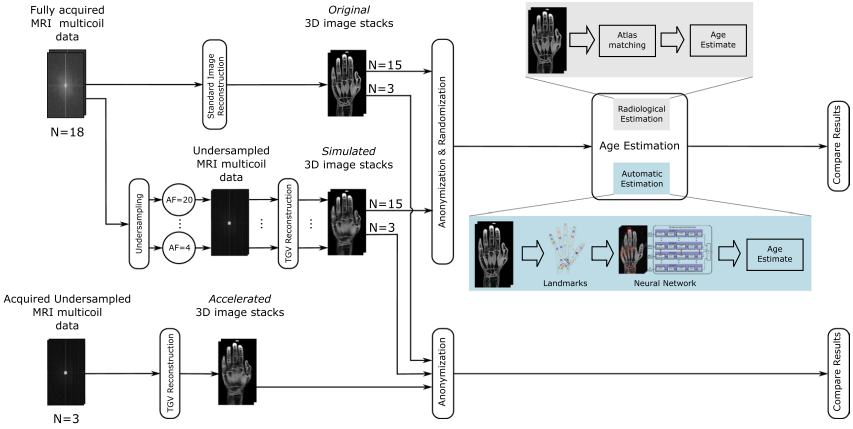


**Figure 1.** Schematic illustration of the applied method to investigate the reliability of age estimation based on undersampled data. Both original images and images reconstructed from undersampled data (AF: acceleration factor describing speed-up of acquisition time) are used for age estimation applying radiological and automatic estimation methods, respectively. Finally, the differences in the estimates are evaluated. Additionally, simulated data is compared to actually acquired data to show the validity of using retrospectively undersampled data.

For the remaining three volunteers, the undersampling patterns were matched exactly to the pattern of the additionally acquired accelerated measurements, simulating acquisition times of 28, 15 and eight seconds, respectively.

The software for image reconstruction is provided online at https://github.com/IMTtugraz/AVIONIC.

**Comparison of Simulated and Acquired Data.** For three volunteers (see Table 1), we compared acquired undersampled images with the corresponding simulated images. A comparison of changes of specific image features with increasing undersampling factor in both acquired and simulated data serves the purpose of showing the validity of using retrospectively undersampled data for this study.

**Skeletal Rating.** Skeletal age was rated independently using two different methods. A radiologist with more than five years of expertise in forensic applications (R1) and a pediatric radiologist with five years of experience in bone age estimation (R2) independently evaluated whether the quality of the simulated images was adequate for reproducible radiological age estimation. For MRI-based radiological age estimation, radiologists applied the method proposed by Greulich and Pyle[36] (GP) to the MR images evaluated as assessable. The GP method, originally developed for age estimation based on radiographs, was verified to be applicable for age estimation from MR images, reporting errors on the same scale as inter-rater variations[37]. To avoid biased age estimates the MR images were anonymized and randomized irrespective of the acceleration factor.

To estimate general limits of radiological assessability, an initial analysis was performed after acquisitions of the first five volunteers. The acquired MR data were undersampled according to the values in Table 1. A radiological evaluation rated four out of five data sets with acquisition times below 15 seconds as unusable for a non-ambiguous radiological age estimation. Therefore, for radiological evaluation only original data and simulated image stacks with acquisition times of 29 and 15 seconds – a total of 45 data sets – were presented to radiologists R1 and R2 for age estimation.

The second skeletal age rating was performed using the fully automated age estimation method proposed by Urschler *et al.*[24] extended by improving landmark localization accuracy[38] and introducing a novel deep neural network based age estimator[39]. This setup was used solely as an age predictor, i.e. without using data from the present study to further train the model or tune its parameters.

**Statistical Analysis.** The main focus of this study was on the reliability of age estimation with decreasing acquisition time and not on the actual absolute results of age estimation. Therefore, we analyzed the difference introduced into the estimated age with decreasing acquisition time to assess reliability. For this analysis the reference age for comparison was the age estimated by each observer using the original images. The difference was then calculated by subtracting the age estimated from original data from the age estimated from simulated data for results of radiologist R1 and R2 ($\Delta\text{Age}_{R1}$, $\Delta\text{Age}_{R2}$) and the automatic age estimation ($\Delta\text{Age}_{autom}$):

$$\Delta\text{Age}_{R1} = \text{Age}_{R1} - \text{Age}_{R1,orig}$$

$$\Delta Age_{R2} = Age_{R2} - Age_{R2,orig}$$

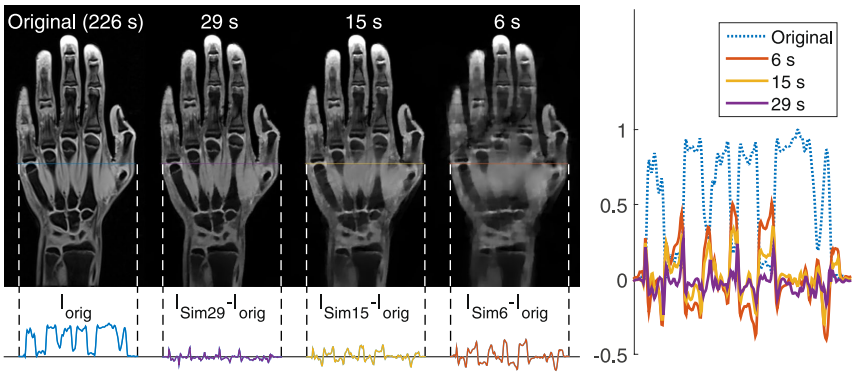


**Figure 2.** Exemplary images of a selected slice of one volunteer (14.2 y) for originally acquired data, $I_{orig}$, and simulated images $I_{Sim29}$, $I_{Sim15}$ and $I_{Sim6}$. Differences between original and reconstructed images are additionally displayed for selected image profiles.

$$\Delta \mathrm{Age}_{autom} = \mathrm{Age}_{autom} - \mathrm{Age}_{autom,orig}$$

The standard deviation of the signed differences (SSD) of $\Delta$Age was used as a measure for the reliability of the age estimation, the mean of signed differences (MSD) to identify potential systematic errors. Additionally, the intra-class correlation coefficient *ICC* was calculated between the age estimates based on original images and the estimates from simulated data sets.

The inter-rater reproducibility between all three observers, i.e. R1, R2 and the automatic age estimation method (A), was determined by calculating ICC and Bland-Altman limits of agreement (LOA) between corresponding age estimates. The inter-rater reproducibility between the radiological estimation and the automatic method thereby provides a measure of conformity between the two different age estimation methods. This information may help to evaluate the potential to combine them to a hybrid between manual and fully automatic age estimation similar to an approach recently proposed for volumetry in oncology[40].

All statistical analyses were performed using MATLAB (R2014b, The MathWorks Inc., Natick, MA, USA).

**Data Availability.** The acquired MRI data sets generated and/or analyzed during the current study are not publicly available for data privacy reasons. The participants did not explicitly give their consent to freely distribute their imaging data, albeit anonymized. However, quantitative measures derived from the imaging data will be made available as a supplementary to this publication.

**Ethical approval.** All procedures performed in studies involving human participants were in accordance with the ethical standards of the institutional and/or national research committee and with the 1964 Helsinki declaration and its later amendments or comparable ethical standards.

## Results

**Image Reconstruction and Image Quality.** Figure 2 shows representative images of a central slice of the left hand and wrist of one volunteer (14.2 y) for the original data set and simulated acquisition times of 29, 15 and six seconds. Qualitatively, for an acquisition time of at least 15 seconds no severe artefacts can be identified; however, images with an acquisition time of 15 seconds already feature image blurring, which increases with the acceleration factor. For an acquisition time of six seconds, differences between original and simulated data become clearly visible.

Additionally, the difference between original and simulated images is shown for an image profile line covering bone, muscle tissue and joint cartilage. Deviations from the original image increase with the acceleration factor and become pronounced for larger muscle regions. In general, the reduction of available data leads to blurring and loss of morphological details in the resulting images. This blurring is observable for example as overlap of the muscle tissue with metacarpal bones or the broadening of the joint cartilage of the fifth digit (first visible for $t_{Acqu} = 15$ s) producing positive peaks in the difference of the profile lines.

**Assessability of Simulated MR Images.** All images with acquisition times of 29 and 15 seconds were rated as suitable for age estimation by both radiologists. The automatic age estimation provided age estimates for all data sets.

**Variability and Reliability of Rating.** Figure 3 visualizes the influence of the reduction of acquisition time on age estimation by showing the difference to the age estimates based on the original data for radiologists R1 and R2 and the automatic method (the values for all age estimates can be found in Supplementary Table S1 online). For the radiological evaluation, standard deviations of signed differences (SSD) introduced by simulated

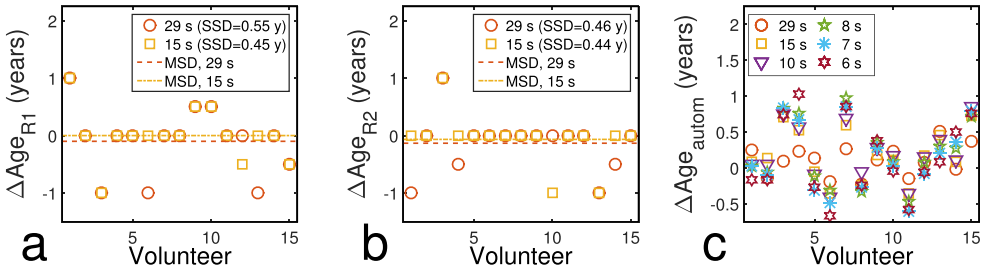


**Figure 3.** Differences to age estimates based on original data set introduced by a reduction of the acquisition time. Differences are shown for (**a**) R1, (**b**) R2 and (**c**) the automatic age estimation method as a function of the acquisition time. Lines in (**a**) and (**b**) mark the MSD value for each acceleration factor (exact values are shown in Table 2).

| | R1 | | | R2 | | | Automatic Analysis | | |
|---|---|---|---|---|---|---|---|---|---|
| Name | ICC | SSD (y) | MSD (y) | ICC | SSD (y) | MSD (y) | ICC | SSD (y) | MSD (y) |
| $I_{Sim29}$ | 0.96 | 0.55 | −0.1 | 0.97 | 0.46 | −0.13 | 0.99 | 0.21 | 0.10 |
| $I_{Sim15}$ | 0.98 | 0.45 | 0 | 0.98 | 0.44 | −0.07 | 0.98 | 0.34 | 0.18 |
| $I_{Sim10}$ | — | — | — | — | — | — | 0.98 | 0.37 | 0.21 |
| $I_{Sim8}$ | — | — | — | — | — | — | 0.97 | 0.43 | 0.21 |
| $I_{Sim7}$ | — | — | — | — | — | — | 0.97 | 0.46 | 0.15 |
| $I_{Sim6}$ | — | — | — | — | — | — | 0.96 | 0.51 | 0.14 |

**Table 2.** Comparison between ratings of radiological and automatic age estimation: reliability of age estimates is reported as correlation with estimates based on fully-sampled data sets. ICC: Intra-class correlation coefficient, SSD/MSD: Standard deviation/mean of signed differences.

acceleration were 0.57 y and 0.46 y for acquisition times of 29 and 15 seconds, respectively, for R1 and 0.46 y and 0.44 y for R2; the corresponding values for the mean deviations (MSD) were −0.10 y and 0.00 y for R1 and −0.13 y and −0.07 y for R2. For automatic age estimation, SSD values increased with the acceleration factor and reached a maximum of 0.51 y for $t_{Acqu}$ =6 s, MSD values lay between 0.10 and 0.21 years; all SSD and MSD values are provided in Table 2.

The values for the ICC in Table 2 show high intra-class correlation for both applied age estimation methods. A comparison to original age estimates yields a minimum ICC of 0.96 for all evaluated data sets; the values for inter-rater variability lay between 0.91 and 0.99. All results were highly significant with $p < 0.000001$ for all values. The Bland-Altman plots in Fig. 4 show high inter-rater agreement. The mean values of the Bland-Altman analysis lie between 0.03 and 0.33 years and suggest no systematic error in the analysis. Radiological raters R1 and R2 show the best agreement with LOA = 1.02 y, testing the agreement between radiological and automatic method yields LOA = 1.5 y for R1 and LOA = 1.14 y for R2.

The automatic method as well as both radiologists estimated the oldest volunteer (23.2 y) to be over 18 y for all acceleration factors. The evaluation by the radiologists yielded 19 y for all acceleration factors for this volunteer – the maximally assessable age – and the automatic estimation provided estimates between 18.3 y and 18.9 y.

**Comparing Simulated and Acquired Data.** Figure 5 compares simulated data with actually acquired undersampled data of three volunteers (15.75, 18.85 and 21.61 years from top to bottom) showing image details for simulated (upper rows) and acquired (lower rows) accelerated MRI and acquisition times of 29, 15 and eight seconds. For the youngest volunteer epiphyseal gaps are still visible for an acquisition time of eight seconds and the hyperintense structure marked by circles is blurred equally for simulated and acquired images with decreasing acquisition time. Structures marked in the images of the remaining two volunteers become noticeably blurred for an acquisition time of 15 seconds and disappear for further acceleration; again, this behavior can be seen in both simulated and acquired data.

## Discussion

The presented results suggest that a radiological analysis can provide reliable age estimates based on hand/wrist MRI using an acquisition time of only 15 seconds, which corresponds to an acceleration factor of approximately 7.5 compared to the original acquisition time of 3:46 minutes. For this duration no relevant artefacts occurred in the simulated images and all data sets were deemed assessable and yielded a maximum SSD of 0.55 years (shown in Fig. 3). This is in the range of reported errors for the radiological examination of skeletal development[41]. With decreasing acquisition time, automatic age estimation showed an increasing deviation compared to the estimation from the original data set. However, for a simulated duration of six seconds the standard deviation was still only

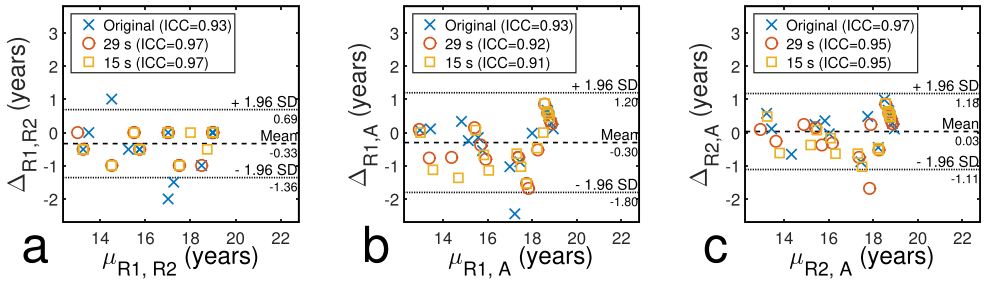


**Figure 4.** Bland-Altman plots for inter-rater agreement. Agreement is shown between (**a**) R1 and R2, (**b**) R1 and the automatic method (A) and (**c**) R2 and the automatic method as a function of the acquisition time. $\mu_{R1,R2}$, $\mu_{R1,A}$ and $\mu_{R2,A}$, describe the mean value of the age estimates of the respective raters, $\Delta$ is the difference between the respective ratings.

0.51 years (see Table 2). Both estimation methods yielded small MSD values suggesting that age estimates are not influenced by a systematic offset.

With increasing acceleration factor, images reconstructed from undersampled data tend to appear blurry while noise is suppressed and fine structures become less distinctive, creating an unusual image representation for radiologists. The quality of the simulated images allowed a radiological analysis for acquisition times down to 15 seconds and age estimates for the analyzed data sets were close to identical. The automatic method provided reliable results even for the shortest acquisition time of six seconds. This is a remarkable reduction of the acquisition time as existing age estimation studies at a field strength of 3 Tesla can require acquisition times of up to six minutes for the wrist only[7]. The potential acceleration is markedly higher than acceleration factors reported in a recent study by Terada *et al*. reducing the acquisition time by a factor of 4 from 2:44 minutes to 41 seconds[42]. However, our results cannot easily be compared to the work of Terada *et al*., since they used a low-field MR scanner at 0.3 Tesla. A lower field strength generally bears the disadvantage of lower SNR but also allows shorter acquisition times due to shorter $T_1$ relaxation times. Above that, Terada *et al*. applied an optimized undersampling pattern for their compressed sensing-based approach, which is not commercially available.

The comparison of standard deviations of radiological and automatic analysis methods has to be interpreted carefully, since the minimal deviation that may occur using the GP atlas-matching scheme is 0.5 years, while the automatic method provides a continuous age estimate. Furthermore, contrary to the modern-day reference population of the automatic method, the GP scheme uses a different reference population consisting of Caucasian volunteers born in the 1930's, which may be considered outdated due to changes in multinational behavior. From a methodological point of view, the difference between the acceptable acceleration factor for an analysis by a radiologist and that for the automatic method could be explained by the fact that the automatic age estimation algorithm analyses the entire 3D data set simultaneously. This avoids influences of single artefacts mimicking a partial closure of the epiphyseal gap in a 2D representation.

The main aim of this study was to test reliability. However, the oldest volunteer (23.15 years) was included to test whether image reconstruction may introduce misleading image features causing an estimation of under 18 years – a legally important age threshold indicating majority age in many countries. Based on the atlas, the maximum age a radiologist can allocate is 19 years old. In the oldest volunteer this maximum age was allocated to image stacks of all acceleration factors. Accordingly, the automatic estimation also provided estimates over 18 y for all acceleration factors, which suggests that the chosen undersampling and reconstruction strategies are robust against misleading artefacts for the simulated acceleration factors.

The validity to use retrospectively undersampled data in this study was shown by a comparison of simulated and acquired images. The simulation of an accelerated acquisition removes data lines that are not acquired during an actual acquisition. Therefore, an agreement between simulated and acquired data can be anticipated. Even more, retrospective undersampling represents a worst-case simulation since the reduced amount of data is extracted from a long acquisition during which more patient movement can occur. For this reason the additional acquisition of accelerated data sets was only performed for a small number of volunteers.

Our work is based on an undersampling scheme readily available on current MR scanners and therefore does not require comprehensive knowledge on undersampling strategies or MR sequence programming. The same applies to the image reconstruction algorithm, which is available to the public in an online repository. This allows for an easy adoption of our proposed method. It is also noteworthy that the automatic method did not require additional training and could readily be applied to undersampled data in its original state. Using the concept of systematically increasing the undersampling of the available data, the feasibility of our approach could already be shown for the relatively small sample size used in this study. We expect to reproduce these results with more data sets, which are currently being acquired.

The potential decrease in acquisition time presented in this study is an important step towards establishing MRI as standard method for age estimation. On successful transfer of this approach to MR acquisitions of third molars and clavicular epiphyses, the application of MRI for multi-factorial age estimation could be promoted

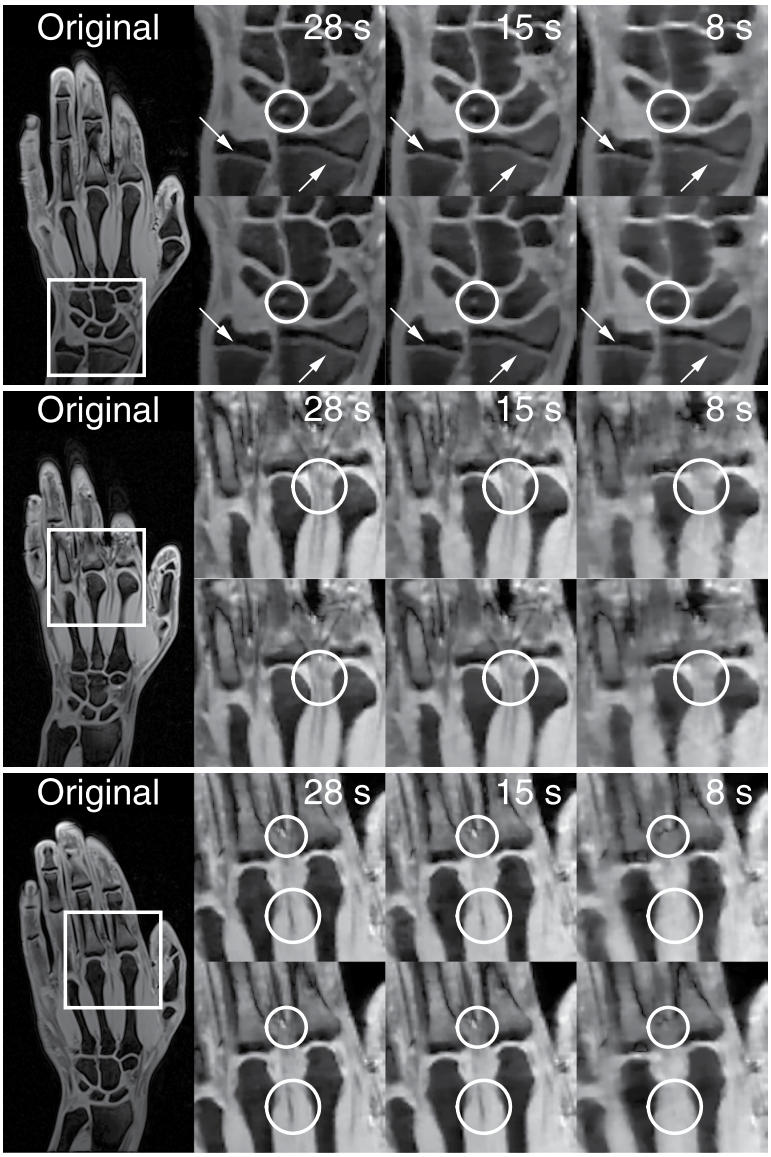


**Figure 5.** Comparison of simulated (upper rows) and acquired (lower rows) undersampled data for three different volunteers (15.75, 18.85 and 21.61 years from top to bottom) and locations. Arrows mark structures relevant for age estimation, while circles highlight structures changing their appearance with decreasing acquisition time in both simulated and acquired data.

even further due to the elimination of the drawback of time consumption. Furthermore, this also translates to a potential reduction of the cost of using this ionizing radiation-free imaging modality for age estimation.

In conclusion, we showed the reliability of image data undersampled with the CAIPIRINHA technique in combination with TGV-based reconstruction for skeletal age estimation. A reduction of the acquisition time to 15 seconds for MR acquisitions of the hand and wrist was found to produce images interpretable using both a radiological and an automatic age estimation method. Furthermore, the high correlation between the two methods shows the potential of automatic methods to support radiologists in age estimation investigations.

## References


1. Martin, D. D. *et al*. The use of bone age in clinical practice–part 1. *Horm Res Paediatr* **76**, 1–9 (2011).
2. Lee, S. C., Shim, J. S., Seo, S. W., Lim, K. S. & Ko, K. R. The accuracy of current methods in determining the timing of epiphysiodesis. *Bone Jt. J* **95–B**, 993–1000 (2013).
3. Wang, W. W. J. *et al*. Correlation of Risser sign, radiographs of hand and wrist with the histological grade of iliac crest apophysis in girls with adolescent idiopathic scoliosis. *Spine* (*Phila Pa 1976*) **34**, 1849–1854 (2009).
4. Schmeling, A., Geserick, G., Reisinger, W. & Olze, A. Age estimation. *Forensic Sci Intl* **165**, 178–181 (2007).
5. Dvorak, J., George, J., Junge, A. & Hodler, J. Age determination by magnetic resonance imaging of the wrist in adolescent male football players. *Br J Sport. Med* **41**, 45–52 (2007).
6. George, J., Nagendran, J. & Azmi, K. Comparison study of growth plate fusion using MRI versus plain radiographs as used in age determination for exclusion of overaged football players. *Br J Sport. Med* **46**, 273–278 (2012).
7. Schmidt, S., Vieth, V., Timme, M., Dvorak, J. & Schmeling, A. Examination of ossification of the distal radial epiphysis using magnetic resonance imaging. New insights for age estimation in young footballers in FIFA tournaments. *Sci. Justice* **55**, 139–144 (2015).
8. Timme, M., Steinacker, J. M. & Schmeling, A. Age estimation in competitive sports. *Int. J. Legal Med.* **131**, 225–233 (2017).
9. Cameron, N. Can maturity indicators be used to estimate chronological age in children? *Ann Hum Biol* **42**, 302–307 (2015).
10. Tanner, J. M. *A history of the study of human growth*. (Cambridge University Press, 1981).
11. Ulijaszek, S. J., Johnston, F. E. & Preece, M. A. *The Cambridge encyclopedia of human growth and development*. (Cambridge University Press, 1998).
12. Liversidge, H. M., Buckberry, J. & Marquez-Grant, N. Age estimation. *Ann Hum Biol* **42**, 299–301 (2015).
13. van Rijn, R. & Thodberg, H. Bone age assessment: automated techniques coming of age? *Acta radiol.* **54**, 1024–1029 (2013).
14. Schmeling, A., Garamendi, M. P., Prieto, J. L. & Landa, I. M. Forensic Age Estimation in Unaccompanied Minors and Young Living Adults. *Forensic Med. - From Old Probl. to New Challenges* https://doi.org/10.5772/19261 (2011).
15. Schmeling, A. *et al*. Updated recommendations of the Study Group on Forensic Age Diagnostics for age estimation in the living in criminal proceedings. *Rechtsmedizin* **18**, 451–453 (2008).
16. Hillewig, E. *et al*. Magnetic resonance imaging of the medial extremity of the clavicle in forensic bone age determination: a new four-minute approach. *Eur. Radiol.* **21**, 757–767 (2011).
17. Dedouit, F. *et al*. Age assessment by magnetic resonance imaging of the knee: A preliminary study. *Forensic Sci Intl* **217**, 232.e1–232.e7 (2012).
18. Terada, Y. *et al*. Skeletal age assessment in children using an open compact MRI system. *Magn Reson Med* **69**, 1697–1702 (2013).
19. Tomei, E. *et al*. Value of MRI of the hand and the wrist in evaluation of bone age: Preliminary results. *J Magn Reson Imaging* **39**, 1198–1205 (2013).
20. Serinelli, S. *et al*. Accuracy of MRI skeletal age estimation for subjects 12–19. Potential use for subjects of unknown age. *Int J Leg. Med* **129**, 609–617 (2015).
21. Baumann, P. *et al*. Dental age estimation of living persons: Comparison of MRI with OPG. *Forensic Sci Intl* **253**, 76–80 (2015).
22. De Tobel, J., Hillewig, E. & Verstraete, K. Forensic age estimation based on magnetic resonance imaging of third molars: converting 2D staging into 3D staging. *Ann. Hum. Biol.* **44**, 121–129 (2017).
23. Ekizoglu, O. *et al*. Forensic age estimation via 3-T magnetic resonance imaging of ossification of the proximal tibial and distal femoral epiphyses: Use of a T2-weighted fast spin-echo technique. *Forensic Sci. Int.* **260**, 102.e1–102.e7 (2016).
24. Urschler, M., Grassegger, S. & Štern, D. What automated age estimation of hand and wrist MRI data tells us about skeletal maturation in male adolescents. *Ann Hum Biol* **42**, 358–367 (2015).
25. Breuer, F. A. *et al*. Controlled aliasing in parallel imaging results in higher acceleration (CAIPIRINHA) for multi-slice imaging. *Magn Reson Med* **53**, 684–691 (2005).
26. Bredies, K., Kunisch, K. & Pock, T. Total generalized variation. *SIAM J Imaging Sci* **3**, 492–526 (2010).
27. Knoll, F., Bredies, K., Pock, T. & Stollberger, R. Second order total generalized variation (TGV) for MRI. *Magn Reson Med* **65**, 480–491 (2010).
28. Knoll, F., Clason, C., Bredies, K., Uecker, M. & Stollberger, R. Parallel Imaging with Nonlinear Reconstruction using Variational Penalties. *Magn Reson Med* **67**, 34–41 (2012).
29. Knoll, F. *et al*. Reconstruction of undersampled radial PatLoc imaging using total generalized variation. *Magn Reson Med* **70**, 40–52 (2013).
30. Valkonen, T., Bredies, K. & Knoll, F. Total Generalized Variation in Diffusion Tensor Imaging. *SIAM J Imaging Sci* **6**, 487–525 (2013).
31. Langkammer, C. *et al*. Fast quantitative susceptibility mapping using 3D EPI and total generalized variation. *Neuroimage* **111**, 622–630 (2015).
32. Athalye, V., Lustig, M. & Uecker, M. Parallel magnetic resonance imaging as approximation in a reproducing kernel Hilbert space. *Inverse Probl* **31**, 45008 (2015).
33. Buehrer, M., Pruessmann, K. P., Boesiger, P. & Kozerke, S. Array compression for MRI with large coil arrays. *Magn Reson Med* **57**, 1131–1139 (2007).
34. Uecker, M. *et al*. ESPIRiT–an eigenvalue approach to autocalibrating parallel MRI: Where SENSE meets GRAPPA. *Magn Reson Med* **71**, 990–1001 (2014).
35. Chambolle, A. & Pock, T. A First-Order Primal-Dual Algorithm for Convex Problems with Applications to Imaging. *J Math Imaging Vis* **40**, 120–145 (2011).
36. Greulich, W. W. & Pyle, S. I. Radiographic atlas of skeletal development of the hand and wrist. *Am J Med Sci* **238**, 393 (1959).
37. Urschler, M. *et al*. Applicability of Greulich–Pyle and Tanner–Whitehouse grading methods to MRI when assessing hand bone age in forensic age estimation: A pilot study. *Forensic Sci Intl* **266**, 281–288 (2016).
38. Payer, C., Štern, D., Bischof, H. & Urschler, M. Regressing Heatmaps for Multiple Landmark Localization Using CNNs. *Med. Image Comput. Comput. Interv.–MICCAI 2016: 19th International Conference, Athens, Greece, October 17–21, 2016, Proceedings, Part II*, 230–238 (Springer International Publishing, 2016).
39. Štern, D., Payer, C., Lepetit, V. & Urschler, M. Automated Age Estimation from Hand MRI Volumes Using Deep Learning. *Med. Image Comput. Comput. Interv.–MICCAI 2016 19th Int. Conf. Athens, Greece, Oct. 17–21, 2016, Proceedings, Part II*, 194–202 (2016).
40. Kleesiek, J. *et al*. Virtual Raters for Reproducible and Objective Assessments in Radiology. *Sci. Rep.* **6**, 25007 (2016).
41. Ritz-Timme, S. *et al*. Age estimation: The state of the art in relation to the specific demands of forensic practise. *Int J Leg. Med* **113**, 129–136 (2000).
42. Terada, Y. *et al*. Acceleration of skeletal age MR examination using compressed sensing. *J. Magn. Reson. Imaging* **44**, 204–211 (2015).


## Acknowledgements

We thank Sylvia Wolf and Alexander Bornik for proofreading the manuscript. This work was supported by the SFB "Mathematical Optimization and Applications in Biomedical Sciences" of the Austrian Science Fund (FWF): SFB F32-N18 and the project FAME of the Austrian Science Fund (FWF): P28078-N33.

## Author Contributions

All named authors have contributed significantly to this work. The concept and design was defined by T.W., B.N. and M.U. The method of reconstruction of undersampled M.R. acquisitions was implemented by M.S. and R.S. C.P. and M.U. contributed the software for automatic age estimation and conducted the respective experiments. T.E. and S.T. performed the radiological analysis and B.N. conducted the study and evaluated the data. The manuscript was written by B.N., M.S. and M.U.

## Additional Information

**Supplementary information** accompanies this paper at https://doi.org/10.1038/s41598-018-20475-1.

**Competing Interests:** The authors declare that they have no competing interests.

**Publisher's note:** Springer Nature remains neutral with regard to jurisdictional claims in published maps and institutional affiliations.

# 3 Discussion

This thesis presents different approaches to measure or derive estimators for tissue remodelling from MR data and their applicability for medical and clinical forensic problems. Following further studies, the newly-found estimators may eventually serve as biomarkers.
The studies conducted within the framework of this thesis emphasize the versatility of MR techniques by addressing different levels of biomarkers applying different techniques. The application of standard MR imaging protocols, DCE-MRI, MR spectroscopy, undersampling strategies and neural network-based image analysis emphasizes the importance of quantitative MRI for diagnostic purposes and shows its versatility of applicability.

## 3.1 Determination of Biomarkers

Biomarkers are defined as objectively measured characteristics that are evaluated as indicators of biological processes [188]. More generally, a biomarker can be "almost any measurement reflecting an interaction between a biological system and a potential hazard" [189]. Additionally, a biomarker should show content validity, construct validity and criterion validity, which need to be confirmed by analyses of reliability, sensitivity and predictive power [190]. The complexity of the data analysis applied to the acquired data, however, can be adapted to the intended application.

The estimation of the age of soft tissue haematomas was based on simple contrast analysis. The reason for this was the intention to create a model that can be easily adopted without further knowledge and thereby to promote an application of the proposed method. This is also the reason for the application of standard commercially available sequences.
Signal contrast is a characteristic that can be determined easily; however, it cannot provide detailed information on specific processes occurring during haematoma resorption. Still, literature on contrast behaviour of intracranial haematomas [124, 125] suggested that signal contrast information may provide evaluable information on the time of origin.
The outcome of this study is a simple model based solely on contrast information of standard commercially available MRI sequences. The simplicity of this model allows for an easy adoption of the method, on the one hand,

but also emphasizes the relevance of a quantitative analysis of MRI data – even for a quantity as simple as contrast – on the other hand.

The formation of bone bridges was hypothesized to be triggered by increased microvessel proliferation. Therefore, pharmacokinetic parameters were anticipated to provide insight into formation processes due to their sensitivity to microvessel-related functional changes.
The absence of an adequate blood vessel that could provide an arterial input function in the field of view required the application of a reference region model (RRM) to the acquired DCE-MRI data. An RRM-based analysis only requires a well-defined homogeneous tissue region with known tissue parameters, which is located near the region of interest.
The course of the transfer coefficient $K^{trans}$ provided information on the microvessel proliferation in a minimally invasive manner, which could otherwise only be derived using histological analyses.

The fat fraction in bones has already been defined as a biomarker for the conversion of red to yellow bone marrow with increasing age but so far, the significance of relaxation times in this context has not been investigated. However, transverse relaxation has a strong effect on the fat fraction determination due to pronounced differences between the transverse relaxation times $T_2$ of the water and the fat compartment. Furthermore, the longitudinal relaxation times $T_1$ of water and fat compartments are reported to change with changing relative concentrations [191]. Therefore, a conversion of the bone marrow should also be detectable as changes in $T_1$; however, relaxation times cannot serve as a reliable biomarker due to their response to numerous influences, i.e. their limited specificity.
The acquisition of repeated measurements for the relaxometry study performed in the course of this thesis provided estimates for the precision of relaxometry in lumbar vertebrae. Additionally, relaxation times showed different correlations for female and male volunteers.

For the study on undersampling of MRI data for age estimation, the $T_1$ contrast of epiphyseal gaps can be interpreted as a biomarker for age. As described in 1.5 these gaps appear as hyperintensities, which can be used to apply established radiological methods as well as fully automatic methods to estimate the age of a living subject. In the case of automatic methods, however, it cannot be entirely ruled out that the applied algorithms identify additional age-related parameters in the data set they are trained on.

## 3.2 Novelty

Although contrast information is very simple to measure in MR images, the application of contrast analysis has not been used for an assessment of

haematoma age before. While changes over time in $T_1$- and $T_2$-weighted images have been reported, up to now no model for contrast changes of subcutaneous haematomas has been created. There are several reasons for this. First of all, haematomas have scarcely been investigated extracranially, which is owed to the fact that they are not clinically relevant. However, in the field of clinical forensics subcutaneous haematomas are important for the reconstruction of events and a method for determining the age of haematomas is highly desired. Secondly, the creation of a model requires data from standardized procedures to derive reliable information and the data used for the model must be acquired in relevant phases of haematoma resorption.
The study on soft tissue haematomas therefore was the first to address the estimation of the age of extracranial haematomas based on standardized measurements.

The formation of bone bridges has been investigated using contrast enhanced MRI before [192, 193]; however, not using DCE-MRI. Consequently, the changes of pharmacokinetic parameters in respect to the formation of bone bridges have not been investigated. The study on bone bridge formation showed that DCE-MRI investigations can provide microvessel-related functional information of injured growth plates in addition to imaging data. Furthermore, it was shown that a preclinical DCE-MRI study can be conducted on a clinical scanner providing highly resolved images and dynamic data with adequate signal-to-noise ratio. Ultimately, the course of $K^{trans}$ gave insight into the processes involved in bone bridge formation.

In the spectroscopy study on human lumbar vertebrae the reproducibility of relaxometry has been investigated. This study provided information on average relaxation times in this body area, on the precision of the applied method and on the implications on the determination of the fat fraction – a biomarker used for numerous applications [166–168, 194]. A correlation between $T_2$ of the water compartment and the fat fraction could be shown for male subjects, which was only reported for women before. Finally, a correlation between fat fraction and $T_1$ of the water compartment was found, comparable to the behaviour reported for brown adipose tissue [191].

The study on the acceleration of MR imaging for forensic age estimation is based on state-of-the-art methods. The CAIPIRINHA pattern used for retrospective undersampling is available on current MR scanners and enables optimized undersampling; image reconstruction is performed applying the TGV algorithm.
The quality of the reconstructed images was evaluated by radiologists and a recently published fully automatic method. The study thereby showed that a combination of CAIPIRINHA and TGV allowed for higher undersampling factors compared to existing studies [195]. Above that, this is the first study

to use an automatic and objective evaluation method for the assessment of the quality of undersampled images for age estimation.

## 3.3 Limitations

The simplicity of the model used for the haematoma study allows for an easy adoption of the method; however, an incorporation of additional information may still enhance accuracy.
The inclusion of relaxation times may provide additional information. With adequate values for $T_I$, a bi-exponential fit to the data could identify different processes; however, this may not be feasible in an acceptable acquisition time. Volume information, a typical parameter used for intracranial hemorrhage, cannot be included in the model since the diffuse borders of the blood volumes did not allow for a reliable quantitative analysis, which represents another notable difference between intra- and extracranial haematomas.
The acquisition of additional data may allow an optimization of the weighting of the different parameters to enhance the accuracy of the estimation of haematoma age. Also, the empiric assumption of an exponential contrast behavior could be adapted.

Concerning the investigation of bone bridge formation, a limiting factor of the study is that the results of the qRT-PCR analyses are ambiguous and cannot be interpreted properly without additional data. Histologic results help to interpret the results but uncertainties remain. To rule out a possible contamination of the physeal samples by surrounding tissue, applying microdissection should be considered for future studies.

The minimum repetition time applied for the determination of $T_1$ in the relaxometry study was $T_R = 600\,\text{ms}$. For the chosen remaining sequence parameters, this was the smallest possible value but judging from the results, this value was too long to enable a reliable identification of $T_1$ of the fat compartment. A potential improvement could be an additional acquisition with reduced spectral resolution, which would allow shorter repetition times.
Another limitation of the study is the combined analysis of all fat peaks. The different peaks of the fat component generally exhibit different relaxation parameters and therefore an influence on the final results can be anticipated; however, previous studies so far only reported negligible influences [196].

The main limitation of the study on age estimation is the relatively small number of volunteers investigated in this study. This is owed to the fact that the raw data is not available for previous volunteers who participated in the study. While it is expected that the results can be reproduced for a larger cohort, additional data will also allow to investigate the influence

of different image reconstruction algorithms or optimized undersampling patterns.

## 3.4 Summary and Conclusion

In the presented work, information regarding tissues changes was derived from standard clinical data, contrast enhanced images, spectroscopy acquisitions and using automatic, neural network-based techniques. This work thereby provides a basis for further studies, emphasizing the importance to consider the variety of techniques that is available for MR-based studies.

Tissue remodelling is often considered in respect to age, for example, to derive the biological age of a subject to plan surgery. This aspect is also present in this thesis, which comprises two studies addressing age estimation in the living. These two studies are based on different markers and thereby also illustrate the different age ranges that can be described by a specific parameter.
The remaining two studies investigate tissue remodelling as a response to injuries. While one study investigates rather superficial injuries in form of subcutaneous haematomas, the second study identifies specific details of healing processes in the growth plate. This difference is also reflected in the level of the applied acquisition strategies and analysis methods.

In conclusion, this thesis provides examples on how magnetic resonance techniques can be applied to determine biomarkers related to tissue remodelling. The range of methods that were applied in the course of this thesis shows the versatility of MR as well as its ability to address specific problems by applying specialized methods.

# Bibliography


[1] Purcell E., Torrey H., and Pound R. "Resonance Absorption by Nuclear Magnetic Moments in a Solid." In: *Physical Review* 69.1-2 (Jan. 1946), pp. 37–38. DOI: 10.1103/PhysRev.69.37 (cit. on p. 1).

[2] Bloch F., Hansen W., and Packard M. "Nuclear Induction." In: *Physical Review* 69.3-4 (Feb. 1946), pp. 127–127. DOI: 10.1103/PhysRev.69.127 (cit. on p. 1).

[3] Bloch F., Hansen W. W., and Packard M. "The Nuclear Induction Experiment." In: *Physical Review* 70.7-8 (Oct. 1946), pp. 474–485. DOI: 10.1103/physrev.70.474 (cit. on p. 1).

[4] Lauterbur P. C. "Image Formation by Induced Local Interactions: Examples Employing Nuclear Magnetic Resonance." In: *Nature* 242.5394 (Mar. 1973), pp. 190–191. DOI: 10.1038/242190a0 (cit. on p. 1).

[5] Lauterbur P. C. "Magnetic resonance zeugmatography." In: *Pure and Applied Chemistry* 40.1-2 (1974), pp. 149–157. DOI: 10.1351/pac197440010149 (cit. on p. 1).

[6] Runge V. M. *Clinical MRI*. Philadelphia: Saunders, 2002 (cit. on p. 1).

[7] Haacke E., Brown R., Thompson M., and Venkatesan R. *Magnetic Resonance Imaging: Physical Principles and Sequence Design*. Wiley, 1999 (cit. on pp. 1, 3, 4).

[8] Bernstein M. A., King K. E., Zhou X. J., and Fong W. "Handbook of MRI Pulse Sequences." In: *Med. Phys.* 32.5 (2005), p. 1452. DOI: 10.1118/1.1904597 (cit. on pp. 1, 9).

[9] Levitt M. *Spin Dynamics: Basics of Nuclear Magnetic Resonance*. Wiley, 2001 (cit. on pp. 1, 5, 6).

[10] Graaf R. A. de. *In Vivo NMR Spectroscopy*. Wiley Blackwell (John Wiley & Sons), Oct. 2007. DOI: 10.1002/9780470512968 (cit. on pp. 1–3, 5).

[11] Tofts P. *Quantitative MRI of the Brain - Measuring Changes Caused by Disease*. New York: John Wiley & Sons, 2003 (cit. on pp. 1, 6, 12).

[12] Feynman R. P., Vernon F. L., and Hellwarth R. W. "Geometrical Representation of the Schrödinger Equation for Solving Maser Problems." In: *Journal of Applied Physics* 28.1 (1957), pp. 49–52. DOI: http://dx.doi.org/10.1063/1.1722572 (cit. on p. 3).

[13] Bloch F. "Nuclear Induction." In: *Physical Review* 70.7-8 (Oct. 1946), pp. 460–474. DOI: 10.1103/physrev.70.460 (cit. on p. 6).

[14] Crawley A. P. and Henkelman R. M. "A comparison of one-shot and recovery methods in T1 imaging." In: *Magnetic Resonance in Medicine* 7.1 (May 1988), pp. 23–34. DOI: 10.1002/mrm.1910070104 (cit. on pp. 6, 8).

[15] Ejchart A., Oleski P., and Wróblewski K. "Reliability of nonlinear three-parameter analysis of T1 experiments." In: *Journal of Magnetic Resonance (1969)* 59.3 (Oct. 1984), pp. 446–451. DOI: 10.1016/0022-2364(84)90077-5 (cit. on p. 7).

[16] Sodickson D. K. and Manning W. J. "Simultaneous acquisition of spatial harmonics (SMASH): Fast imaging with radiofrequency coil arrays." In: *Magnetic Resonance in Medicine* 38.4 (Oct. 1997), pp. 591–603. DOI: 10.1002/mrm.1910380414 (cit. on pp. 8, 57).

[17] Pruessmann K. P., Weiger M., Scheidegger M. B., and Boesiger P. "SENSE: Sensitivity encoding for fast MRI." In: *Magnetic Resonance in Medicine* 42.5 (Nov. 1999), pp. 952–962. DOI: 10.1002/(sici)1522-2594(199911)42:5<952::aid-mrm16>3.0.co;2-s (cit. on pp. 8, 57).

[18] Griswold M. A., Jakob P. M., Heidemann R. M., Nittka M., Jellus V., Wang J., Kiefer B., and Haase A. "Generalized autocalibrating partially parallel acquisitions (GRAPPA)." In: *Magnetic Resonance in Medicine* 47.6 (June 2002), pp. 1202–1210. DOI: 10.1002/mrm.10171 (cit. on pp. 8, 57).

[19] Candes E., Romberg J., and Tao T. "Robust uncertainty principles: exact signal reconstruction from highly incomplete frequency information." In: *IEEE Trans. Inform. Theory* 52.2 (Feb. 2006), pp. 489–509. DOI: 10.1109/tit.2005.862083 (cit. on pp. 8, 57).

[20] Donoho D. "Compressed sensing." In: *IEEE Trans. Inform. Theory* 52.4 (Apr. 2006), pp. 1289–1306. DOI: 10.1109/tit.2006.871582 (cit. on pp. 8, 57).

[21] Lustig M., Donoho D., and Pauly J. M. "Sparse MRI: The application of compressed sensing for rapid MR imaging." In: *Magnetic Resonance in Medicine* 58.6 (2007), pp. 1182–1195. DOI: 10.1002/mrm.21391 (cit. on pp. 8, 57).

[22] Larkman D. J., Hajnal J. V., Herlihy A. H., Coutts G. A., Young I. R., and Ehnholm G. "Use of multicoil arrays for separation of signal from multiple slices simultaneously excited." In: *J. Magn. Reson. Imaging* 13.2 (Feb. 2001), pp. 313–317. DOI: 10.1002/1522-2586(200102)13:2<313::aid-jmri1045>3.0.co;2-w (cit. on p. 8).

[23] Feinberg D. A. and Setsompop K. "Ultra-fast MRI of the human brain with simultaneous multi-slice imaging." In: *Journal of Magnetic Resonance* 229 (Apr. 2013), pp. 90–100. DOI: 10.1016/j.jmr.2013.02.002 (cit. on p. 8).

[24] Uğurbil K., Xu J., Auerbach E. J., Moeller S., Vu A. T., Duarte-Carvajalino J. M., Lenglet C., Wu X., Schmitter S., Moortele P. F. van de, Strupp J., Sapiro G., Martino F. D., Wang D., Harel N., Garwood M., Chen L., Feinberg D. A., Smith S. M., Miller K. L., Sotiropoulos S. N., Jbabdi S., Andersson J. L., Behrens T. E., Glasser M. F., Essen D. C. V., and Yacoub E. "Pushing spatial and temporal resolution for functional and diffusion MRI in the Human Connectome Project." In: *NeuroImage* 80 (Oct. 2013), pp. 80–104. DOI: 10.1016/j.neuroimage.2013.05.012 (cit. on p. 8).

[25] Bakker C. J. G., Graaf C. N. d., and Dijk P. v. "Derivation of quantitative information in NMR imaging: a phantom study." In: *Phys. Med. Biol.* 29.12 (Dec. 1984), pp. 1511–1525. DOI: 10.1088/0031-9155/29/12/004 (cit. on p. 8).

[26] Look D. C. and Locker D. R. "Time Saving in Measurement of NMR and EPR Relaxation Times." In: *Review of Scientific Instruments* 41.2 (1970), pp. 250–251. DOI: 10.1063/1.1684482 (cit. on p. 8).

[27] Kaptein R., Dijkstra K., and Tarr C. "A single-scan fourier transform method for measuring spin-lattice relaxation times." In: *Journal of Magnetic Resonance (1969)* 24.2 (Nov. 1976), pp. 295–300. DOI: 10.1016/0022-2364(76)90039-1 (cit. on p. 8).

[28] Kay I. and Henkelman R. M. "Practical implementation and optimization of oHomer1985ne-shot T1 imaging." In: *Magnetic Resonance in Medicine* 22.2 (Dec. 1991), pp. 414–424. DOI: 10.1002/mrm.1910220249 (cit. on p. 8).

[29] Haase A. "Snapshot flash MRI. Applications to T1, T2, and chemical-shift imaging." In: *Magnetic Resonance in Medicine* 13.1 (Jan. 1990), pp. 77–89. DOI: 10.1002/mrm.1910130109 (cit. on p. 8).

[30] Deichmann R. and Haase A. "Quantification of T1 values by SNAPSHOT-FLASH NMR imaging." In: *Journal of Magnetic Resonance (1969)* 96.3 (Feb. 1992), pp. 608–612. DOI: 10.1016/0022-2364(92)90347-a (cit. on p. 8).

[31] Jivan A., Horsfield M., Moody A., and Cherryman G. "Dynamic T1 Measurement Using Snapshot-FLASH MRI." In: *Journal of Magnetic Resonance* 127.1 (July 1997), pp. 65–72. DOI: 10.1006/jmre.1997.1177 (cit. on p. 8).

[32] Stollberger R. and Wach P. "Imaging of the active B1 field in vivo." In: *Magn. Reson. Med.* 35.2 (Feb. 1996), pp. 246–251. DOI: 10.1002/mrm.1910350217 (cit. on p. 8).

[33] Cunningham C. H., Pauly J. M., and Nayak K. S. "Saturated double-angle method for rapid B1+ mapping." In: *Magn. Reson. Med.* 55.6 (2006), pp. 1326–1333. DOI: 10.1002/mrm.20896 (cit. on p. 8).

[34] Yarnykh V. L. "Actual flip-angle imaging in the pulsed steady state: A method for rapid three-dimensional mapping of the transmitted radiofrequency field." In: *Magn. Reson. Med.* 57.1 (2006), pp. 192–200. DOI: 10.1002/mrm.21120 (cit. on p. 8).

[35] Jiru F. and Klose U. "Fast 3D radiofrequency field mapping using echo-planar imaging." In: *Magn. Reson. Med.* 56.6 (2006), pp. 1375–1379. DOI: 10.1002/mrm.21083 (cit. on p. 8).

[36] Chung S., Kim D., Breton E., and Axel L. "Rapid B1+ mapping using a preconditioning RF pulse with TurboFLASH readout." In: *Magn. Reson. Med.* 64.2 (2010), pp. 439–446. DOI: 10.1002/mrm.22423 (cit. on p. 8).

[37] Morrell G. R. "A phase-sensitive method of flip angle mapping." In: *Magn. Reson. Med.* 60.4 (Oct. 2008), pp. 889–894. DOI: 10.1002/mrm.21729 (cit. on p. 8).

[38] Sacolick L. I., Wiesinger F., Hancu I., and Vogel M. W. "B1 mapping by Bloch-Siegert shift." In: *Magn. Reson. Med.* 63.5 (Apr. 2010), pp. 1315–1322. DOI: 10.1002/mrm.22357 (cit. on p. 8).

[39] Chang Y. V. "Rapid B1 mapping using orthogonal, equal-amplitude radio-frequency pulses." In: *Magn. Reson. Med.* 67.3 (June 2011), pp. 718–723. DOI: 10.1002/mrm.23051 (cit. on p. 8).

[40] Park D. J., Bangerter N. K., Javed A., Kaggie J., Khalighi M. M., and Morrell G. R. "A statistical analysis of the Bloch–Siegert B1 mapping technique." In: *Phys. Med. Biol.* 58.16 (July 2013), pp. 5673–5691. DOI: 10.1088/0031-9155/58/16/5673 (cit. on p. 8).

[41] Duan Q., Gelderen P. van, and Duyn J. "Improved Bloch-Siegert based B1 mapping by reducing off-resonance shift." In: *NMR Biomed.* 26.9 (Jan. 2013), pp. 1070–1078. DOI: 10.1002/nbm.2920 (cit. on p. 8).

[42] Sharma A., Tadanki S., Jankiewicz M., and Grissom W. A. "Highly-accelerated Bloch-Siegert —B1+— mapping using joint autocalibrated parallel image reconstruction." In: *Magn. Reson. Med.* 71.4 (July 2013), pp. 1470–1477. DOI: 10.1002/mrm.24804 (cit. on p. 8).

[43] Pohmann R. and Scheffler K. "A theoretical and experimental comparison of different techniques for B1 mapping at very high fields." In: *NMR Biomed.* 26.3 (Sept. 2012), pp. 265–275. DOI: 10.1002/nbm.2844 (cit. on p. 8).

[44] Haase A. and Frahm J. "NMR imaging of spin-lattice relaxation using stimulated echoes." In: *Journal of Magnetic Resonance (1969)* 65.3 (Dec. 1985), pp. 481–490. DOI: 10.1016/0022-2364(85)90133-7 (cit. on p. 8).

[45] Mareci T., Sattin W., Scott K., and Bax A. "Tip-angle-reduced T1 imaging." In: *Journal of Magnetic Resonance (1969)* 67.1 (Mar. 1986), pp. 55–65. DOI: 10.1016/0022-2364(86)90408-7 (cit. on p. 8).

[46] Franconi F., Seguin F., Sonier C., Le Pape A., and Akoka S. "T1 mapping from spin echo and stimulated echoes." In: *Med. Phys.* 22.11 (1995), p. 1763. DOI: 10.1118/1.597632 (cit. on p. 8).

[47] Ropele S., Stollberger R., Ebner F., and Fazekas F. "T1 imaging using phase acquisition of composite echoes." In: *Magnetic Resonance in Medicine* 41.2 (Feb. 1999), pp. 386–391. DOI: 10.1002/(sici)1522-2594(199902)41:2<386::aid-mrm24>3.0.co;2-s (cit. on p. 8).

[48] Ropele S., Stollberger R., Kapeller P., Hartung H.-P., and Fazekas F. "Fast multislice T1 and T1sat imaging using a phase acquisition of composite echoes (PACE) technique." In: *Magnetic Resonance in Medicine* 42.6 (Dec. 1999), pp. 1089–1097. DOI: 10.1002/(sici)1522-2594(199912)42:6<1089::aid-mrm13>3.0.co;2-6 (cit. on p. 8).

[49] Homer J. and Beevers M. S. "Driven-equilibrium single-pulse observation of T1 relaxation. A reevaluation of a rapid "new" method for determining NMR spin-lattice relaxation times." In: *Journal of Magnetic Resonance (1969)* 63.2 (June 1985), pp. 287–297. DOI: 10.1016/0022-2364(85)90318-x (cit. on p. 9).

[50] Brookes J. A., Redpath T. W., Gilbert F. J., Murray A. D., and Staff R. T. "Accuracy of T1 Measurement in dynamic contrast-enhanced breast MRI using two- and three-dimensional variable flip angle fast low-angle shot." In: *J. Magn. Reson. Imaging* 9.2 (Feb. 1999), pp. 163–171. DOI: 10.1002/(sici)1522-2586(199902)9:2<163::aid-jmri3>3.0.co;2-l (cit. on p. 9).

[51] Deoni S. C., Rutt B. K., and Peters T. M. "Rapid combined T1 and T2 mapping using gradient recalled acquisition in the steady state." In: *Magnetic Resonance in Medicine* 49.3 (Feb. 2003), pp. 515–526. DOI: 10.1002/mrm.10407 (cit. on pp. 9, 11).

[52] Deoni S. C., Peters T. M., and Rutt B. K. "Determination of optimal angles for variable nutation proton magnetic spin-lattice, $T_1$, and spin-spin, $T_2$, relaxation times measurement." In: *Magnetic Resonance in Medicine* 51.1 (2004), pp. 194–199. DOI: 10.1002/mrm.10661 (cit. on pp. 9, 11).

[53] Deoni S. C. L., Peters T. M., and Rutt B. K. "High-resolution T1 and T2 mapping of the brain in a clinically acceptable time with DESPOT1 and DESPOT2." In: *Magnetic Resonance in Medicine* 53.1 (2005), pp. 237–241. DOI: 10.1002/mrm.20314 (cit. on pp. 9, 11).

[54] Hittmair K., Gomiscek G., Langenberger K., Recht M., Imhof H., and Kramer J. "Method for the quantitative assessment of contrast agent uptake in dynamic contrast-enhanced MRI." In: *Magn Reson Med* 31.5 (May 1994), pp. 567–571. DOI: 10.1002/mrm.1910310516 (cit. on p. 9).

[55] Merwa R., Reishofer G., Feiweier T., Kapp K., Ebner F., and Stollberger R. "Impact of B1 inhomogeneities on AIF selection in DCE-MRI at 3 Tesla." In: *Proc. Intl. Soc. Mag. Reson. Med. 17 (2009)*. 2009, p. 4661 (cit. on p. 9).

[56] Kingsley P. B. "Methods of measuring spin-lattice (T1) relaxation times: An annotated bibliography." In: *Concepts in Magnetic Resonance* 11.4 (1999), pp. 243–276. DOI: 10.1002/(sici)1099-0534(1999)11:4<243::aid-cmr5>3.0.co;2-c (cit. on p. 9).

[57] Stikov N., Boudreau M., Levesque I. R., Tardif C. L., Barral J. K., and Pike G. B. "On the Accuracy of T1 Mapping: Searching for Common Ground." In: *Magnetic Resonance in Medicine* 73.2 (2015), pp. 514–522. DOI: 10.1002/mrm.25135 (cit. on p. 9).

[58] Kellman P. and Hansen M. S. "T1-mapping in the heart: accuracy and precision." In: *J Cardiovasc Magn Reson* 16.1 (2014), p. 2. DOI: 10.1186/1532-429x-16-2 (cit. on p. 9).

[59] Dieckmeyer M., Ruschke S., Cordes C., Yap S. P., Kooijman H., Hauner H., Rummeny E. J., Bauer J. S., Baum T., and Karampinos D. C. "The need for T2 correction on MRS-based vertebral bone marrow fat quantification: implications for bone marrow fat fraction age dependence." In: *NMR in Biomedicine* 28.4 (Feb. 2015), pp. 432–439. DOI: 10.1002/nbm.3267 (cit. on pp. 10, 47).

[60] Allerhand A. "Analysis of Carr–Purcell Spin-Echo NMR Experiments on Multiple-Spin Systems. I. The Effect of Homonuclear Coupling." In: *The Journal of Chemical Physics* 44.1 (1966), pp. 1–9. DOI: 10.1063/1.1726430 (cit. on p. 10).

[61] Allerhand A. "Analysis of Carr–Purcell Spin-Echo NMR Experiments on Multiple-Spin Systems. II. The Effect of Chemical Exchange." In: *The Journal of Chemical Physics* 45.3 (1966), pp. 902–916. DOI: 10.1063/1.1727703 (cit. on p. 10).

[62] Carr H. and Purcell E. "Effects of Diffusion on Free Precession in Nuclear Magnetic Resonance Experiments." In: *Phys. Rev.* 94.3 (May 1954), pp. 630–638. DOI: 10.1103/physrev.94.630 (cit. on p. 10).

[63] Majumdar S., Orphanoudakis S. C., Gmitro A., O'Donnell M., and Gore J. C. "Errors in the measurements of T2 using multiple-echo MRI techniques. I. Effects of radiofrequency pulse imperfections." In: *Magnetic Resonance in Medicine* 3.3 (June 1986), pp. 397–417. DOI: 10.1002/mrm.1910030305 (cit. on p. 11).

[64] Majumdar S., Orphanoudakis S. C., Gmitro A., O'Donnell M., and Gore J. C. "Errors in the measurements of T2 using multiple-echo MRI techniques. II. Effects of static field inhomogeneity." In: *Magnetic Resonance in Medicine* 3.4 (Aug. 1986), pp. 562–574. DOI: 10.1002/mrm.1910030410 (cit. on p. 11).

[65] Majumdar S., Gmitro A., Orphanoudakis S. C., Reddy D., and Gore J. C. "An estimation and correction scheme for system imperfections in multiple-echo magnetic resonance imaging." In: *Magnetic Resonance in Medicine* 4.3 (Mar. 1987), pp. 203–220. DOI: 10.1002/mrm.1910040302 (cit. on p. 11).

[66] Crawley A. P. and Henkelman R. M. "Errors in T2 estimation using multislice multiple-echo imaging." In: *Magnetic Resonance in Medicine* 4.1 (Jan. 1987), pp. 34–47. DOI: 10.1002/mrm.1910040105 (cit. on p. 11).

[67] Wong S. T. S. and Roos M. S. "Effects of slice selection and diffusion on T2 measurement." In: *Magnetic Resonance in Medicine* 5.4 (Oct. 1987), pp. 358–365. DOI: 10.1002/mrm.1910050407 (cit. on p. 11).

[68] Meiboom S. and Gill D. "Modified Spin-Echo Method for Measuring Nuclear Relaxation Times." In: *Review of Scientific Instruments* 29.8 (1958), pp. 688–691. DOI: 10.1063/1.1716296 (cit. on p. 11).

[69] Levitt M. H. and Freeman R. "Compensation for pulse imperfections in NMR spin-echo experiments." In: *Journal of Magnetic Resonance (1969)* 43.1 (Apr. 1981), pp. 65–80. DOI: 10.1016/0022-2364(81)90082-2 (cit. on p. 11).

[70] Zur Y. and Stokar S. "A phase-cycling technique for canceling spurious echoes in NMR imaging." In: *Journal of Magnetic Resonance (1969)* 71.2 (Feb. 1987), pp. 212–228. DOI: 10.1016/0022-2364(87)90051-5 (cit. on p. 11).

[71] Lukzen N. N. and Savelov A. A. "Analytical derivation of multiple spin echo amplitudes with arbitrary refocusing angle." eng. In: *J Magn Reson* 185.1 (Mar. 2007), pp. 71–76. DOI: 10.1016/j.jmr.2006.11.010 (cit. on p. 11).

[72] Petrovic A., Scheurer E., and Stollberger R. "Closed-form solution for T2 mapping with nonideal refocusing of slice selective CPMG sequences." In: *Magnetic Resonance in Medicine* 73.2 (2015), pp. 818–827. DOI: 10.1002/mrm.25170 (cit. on p. 11).

[73] Deoni S. C., Ward H. A., Peters T. M., and Rutt B. K. "Rapid T2 estimation with phase-cycled variable nutation steady-state free precession." In: *Magnetic Resonance in Medicine* 52.2 (2004), pp. 435–439. DOI: 10.1002/mrm.20159 (cit. on p. 11).

[74] Neumayer B., Diwoky C., Reinisch A., Strunk D., and Stollberger R. "Quantification of Cell Density of SPIO-Labelled Cell Populations." In: *Proceedings of the International Society for Magnetic Resonance in Medicine*. Ed. by Magnetic Resonance in Medicine I. S. for. Stockholm, Apr. 2010, p. 4192 (cit. on p. 12).

[75] Padhani A. R. "Dynamic contrast-enhanced MRI in clinical oncology: current status and future directions." eng. In: *J Magn Reson Imaging* 16.4 (Oct. 2002), pp. 407–422. DOI: 10.1002/jmri.10176 (cit. on pp. 13, 33).

[76] Neeman M. "Preclinical MRI experience in imaging angiogenesis." eng. In: *Cancer Metastasis Rev* 19.1-2 (2000), pp. 39–43. DOI: 10.1023/A:1026583911941 (cit. on pp. 13, 33).

[77] Gillies R. J., Bhujwalla Z. M., Evelhoch J., Garwood M., Neema M., Robinson S. P., Sotak C. H., and Van Der Sanden B. "Applications of Magnetic Resonance in Model Systems: Tumor Biology and Physiology." In: *Neoplasia* 2.1-2 (Jan. 2000), pp. 139–151. DOI: 10.1038/sj.neo.7900076 (cit. on pp. 13, 33).

[78] Neumayer B., Amerstorfer E., Diwoky C., Lindtner R. A., Wadl E., Scheurer E., Weinberg A.-M., and Stollberger R. "Assessment of Pharmacokinetics for Microvessel Proliferation by DCE-MRI for Early Detection of Physeal Bone Bridge Formation in an Animal Model." In: *Magnetic Resonance Materials in Physics, Biology and Medicine* 30.5 (Oct. 2017), pp. 417–427. DOI: 10.1007/s10334-017-0615-2 (cit. on pp. 13, 33).

[79] Yuh W. T. "An exciting and challenging role for the advanced contrast MR imaging." In: *J. Magn. Reson. Imaging* 10.3 (Sept. 1999), pp. 221–222. DOI: 10.1002/(sici)1522-2586(199909)10:3<221::aid-jmri1>3.0.co;2-x (cit. on p. 13).

[80] Kety S. S. "The Theory and Applications of the Exchange of Inert Gas at the Lungs and Tissues." In: *Pharmacological Reviews* 3.1 (1951), pp. 1–41. eprint: http://pharmrev.aspetjournals.org/content/3/1/1.full.pdf+html (cit. on p. 13).

[81] Tofts P. S., Brix G., Buckley D. L., Evelhoch J. L., Henderson E., Knopp M. V., Larsson H. B., Lee T.-Y., Mayr N. A., Parker G. J., Port R. E., Taylor J., and Weisskoff R. M. "Estimating kinetic parameters from dynamic contrast-enhanced T1-weighted MRI of a diffusable tracer: Standardized quantities and symbols." In: *J. Magn. Reson.*

*Imaging* 10.3 (Sept. 1999), pp. 223–232. DOI: 10.1002/(sici)1522-2586(199909)10:3<223::aid-jmri2>3.0.co;2-s (cit. on pp. 13, 14).

[82] Renkin E. M. "Transport of potassium-42 from blood to tissue in isolated mammalian skeletal muscles." eng. In: *Am J Physiol* 197 (Dec. 1959), pp. 1205–1210 (cit. on p. 14).

[83] Yankeelov T., Pickens D. R., and Price R. R. *Quantitative MRI in Cancer*. Justus-Liebig-Universität Gießen: Taylor & Francis, 2011 (cit. on p. 14).

[84] Moran G. R. and Prato F. S. "Modeling (1H) exchange: an estimate of the error introduced in MRI by assuming the fast exchange limit in bolus tracking." In: *Magn Reson Med* 51.4 (Apr. 2004), pp. 816–827. DOI: 10.1002/mrm.20002 (cit. on p. 15).

[85] Lopata R. G. P., Backes W. H., Bosch P. P. J. van den, and Riel N. A. W. van. "On the identifiability of pharmacokinetic parameters in dynamic contrast-enhanced imaging." In: *Magn Reson Med* 58.2 (Aug. 2007), pp. 425–429. DOI: 10.1002/mrm.21336 (cit. on p. 15).

[86] Aerts H. J. W. L., Riel N. A. W. van, and Backes W. H. "System identification theory in pharmacokinetic modeling of dynamic contrast-enhanced MRI: influence of contrast injection." In: *Magn Reson Med* 59.5 (May 2008), pp. 1111–1119. DOI: 10.1002/mrm.21575 (cit. on p. 15).

[87] Fritz-Hansen T., Rostrup E., Larsson H. B. W., Søndergaard L., Ring P., and Henriksen O. "Measurement of the arterial concentration of Gd-DTPA using MRI: A step toward quantitative perfusion imaging." In: *Magnetic Resonance in Medicine* 36.2 (Aug. 1996), pp. 225–231. DOI: 10.1002/mrm.1910360209 (cit. on p. 15).

[88] Larsson H. B. W., Stubgaard M., Frederiksen J. L., Jensen M., Henriksen O., and Paulson O. B. "Quantitation of blood-brain barrier defect by magnetic resonance imaging and gadolinium-DTPA in patients with multiple sclerosis and brain tumors." In: *Magnetic Resonance in Medicine* 16.1 (Oct. 1990), pp. 117–131. DOI: 10.1002/mrm.1910160111 (cit. on p. 15).

[89] Wang Y., Huang W., Panicek D. M., Schwartz L. H., and Koutcher J. A. "Feasibility of using limited-population-based arterial input function for pharmacokinetic modeling of osteosarcoma dynamic contrast-enhanced MRI data." In: *Magn Reson Med* 59.5 (2008), pp. 1183–1189. DOI: 10.1002/mrm.21432 (cit. on p. 16).

[90] Onxley J. D., Yoo D. S., Muradyan N., MacFall J. R., Brizel D. M., and Craciunescu O. I. "Comprehensive Population-Averaged Arterial Input Function for Dynamic Contrast–Enhanced vMagnetic Resonance Imaging of Head and Neck Cancer." In: *International Journal of Radiation Oncology*Biology*Physics* 89.3 (July 2014), pp. 658–665. DOI: 10.1016/j.ijrobp.2014.03.006 (cit. on p. 16).

[91] Port R. E., Knopp M. V., and Brix G. "Dynamic contrast-enhanced MRI using Gd-DTPA: Interindividual variability of the arterial input function and consequences for the assessment of kinetics in tumors." In: *Mag Reson Med* 45.6 (2001), pp. 1030–1038. DOI: 10.1002/mrm.1137 (cit. on p. 16).

[92] Shukla-Dave A., Lee N., Stambuk H., Wang Y., Huang W., Thaler H. T., Patel S. G., Shah J. P., and Koutcher J. A. "Average arterial input function for quantitative dynamic contrast enhanced magnetic resonance imaging of neck nodal metastases." In: *BMC Medical Physics* 9.1 (2009), p. 4. DOI: 10.1186/1756-6649-9-4 (cit. on p. 16).

[93] Li X., Welch E. B., Arlinghaus L. R., Chakravarthy A. B., Xu L., Farley J., Loveless M. E., Mayer I. A., Kelley M. C., Meszoely I. M., and al. et. "A novel AIF tracking method and comparison of DCE-MRI parameters using individual and population-based AIFs in human breast cancer." In: *Phys. Med. Biol.* 56.17 (Aug. 2011), pp. 5753–5769. DOI: 10.1088/0031-9155/56/17/018 (cit. on p. 16).

[94] Meng R., Chang S. D., Jones E. C., Goldenberg S. L., and Kozlowski P. "Comparison between Population Average and Experimentally Measured Arterial Input Function in Predicting Biopsy Results in Prostate Cancer." In: *Academic Radiology* 17.4 (Apr. 2010), pp. 520–525. DOI: 10.1016/j.acra.2009.11.006 (cit. on p. 16).

[95] McGrath D. M., Bradley D. P., Tessier J. L., Lacey T., Taylor C. J., and Parker G. J. "Comparison of model-based arterial input functions for dynamic contrast-enhanced MRI in tumor bearing rats." In: *Magn Reson Med* 61.5 (May 2009), pp. 1173–1184. DOI: 10.1002/mrm.21959 (cit. on p. 16).

[96] Kovar D. A., Lewis M., and Karczmar G. S. "A new method for imaging perfusion and contrast extraction fraction: Input functions derived from reference tissues." In: *J. Magn. Reson. Imaging* 8.5 (Sept. 1998), pp. 1126–1134. DOI: 10.1002/jmri.1880080519 (cit. on p. 16).

[97] Yankeelov T. E., Luci J. J., Lepage M., Li R., Debusk L., Lin P. C., Price R. R., and Gore J. C. "Quantitative pharmacokinetic analysis of DCE-MRI data without an arterial input function: a reference region model." In: *Magn Reson Imaging* 23.4 (May 2005), pp. 519–529. DOI: 10.1016/j.mri.2005.02.013 (cit. on pp. 16, 22, 34).

[98] Yang C., Karczmar G. S., Medved M., and Stadler W. M. "Multiple reference tissue method for contrast agent arterial input function estimation." In: *Magn Reson Med* 58.6 (Dec. 2007), pp. 1266–1275. DOI: 10.1002/mrm.21311 (cit. on p. 16).

[99] Yankeelov T. E., DeBusk L. M., Billheimer D. D., Luci J. J., Lin P. C., Price R. R., and Gore J. C. "Repeatability of a reference region model for analysis of murine DCE-MRI data at 7T." In: *J Magn Reson Imaging* 24.5 (Nov. 2006), pp. 1140–1147. DOI: 10.1002/jmri.20729 (cit. on p. 16).

[100] Yankeelov T. E., Cron G. O., Addison C. L., Wallace J. C., Wilkins R. C., Pappas B. A., Santyr G. E., and Gore J. C. "Comparison of a reference region model with direct measurement of an AIF in the analysis of DCE-MRI data." In: *Magn. Reson. Med.* 57.2 (2007), pp. 353–361. DOI: 10.1002/mrm.21131 (cit. on p. 16).

[101] Walker-Samuel S., Parker C. C., Leach M. O., and Collins D. J. "Reproducibility of reference tissue quantification of dynamic contrast-enhanced data: comparison with a fixed vascular input function." In: *Phys. Med. Biol.* 52.1 (Dec. 2006), pp. 75–89. DOI: 10.1088/0031-9155/52/1/006 (cit. on p. 16).

[102] Yankeelov T. E., Luci J. J., DeBusk L. M., Lin P. C., and Gore J. C. "Incorporating the effects of transcytolemmal water exchange in a reference region model for DCE-MRI analysis: theory, simulations, and experimental results." In: *Magn Reson Med* 59.2 (Feb. 2008), pp. 326–335. DOI: 10.1002/mrm.21449 (cit. on pp. 17, 19).

[103] Landis C. S., Li X., Telang F. W., Molina P. E., Palyka I., Vetek G., and Springer C. S. "Equilibrium transcytolemmal water-exchange kinetics in skeletal muscle in vivo." In: *Magn Reson Med* 42.3 (Sept. 1999), pp. 467–478. DOI: 10.1002/(sici)1522-2594(199909)42:3<467::aid-mrm9>3.0.co;2-0 (cit. on pp. 17–19).

[104] Buckley D. L., Kershaw L. E., and Stanisz G. J. "Cellular-interstitial water exchange and its effect on the determination of contrast agent concentration in vivo: dynamic contrast-enhanced MRI of human internal obturator muscle." In: *Magn Reson Med* 60.5 (Nov. 2008), pp. 1011–1019. DOI: 10.1002/mrm.21748 (cit. on pp. 17, 19).

[105] Donahue K. M., Weisskoff R. M., Parmelee D. J., Callahan R. J., Wilkinson R. A., Mandeville J. B., and Rosen B. R. "Dynamic Gd-DTPA enhanced MRI measurement of tissue cell volume fraction." In: *Magn Reson Med* 34.3 (Sept. 1995), pp. 423–432. DOI: 10.1002/mrm.1910340320 (cit. on p. 17).

[106] Osbakken M. *NMR Techniques in the Study of Cardiovascular Structure and Functions*. Futura Pub Co, 1988 (cit. on p. 18).

[107] Landis C. S., Li X., Telang F. W., Coderre J. A., Micca P. L., Rooney W. D., Latour L. L., Vétek G., Pályka I., and Springer C. S. "Determination of the MRI contrast agent concentration time course in vivo following bolus injection: Effect of equilibrium transcytolemmal water exchange." In: *Magnetic Resonance in Medicine* 44.4 (2000), pp. 563–574. DOI: 10.1002/1522-2594(200010)44:4<563::aid-mrm10>3.0.co;2-%23 (cit. on pp. 18, 19).

[108] Li J. G., Stanisz G. J., and Henkelman R. M. "Integrated analysis of diffusion and relaxation of water in blood." In: *Magnetic Resonance in Medicine* 40.1 (July 1998), pp. 79–88. DOI: 10.1002/mrm.1910400112 (cit. on p. 18).

[109] Donahue K. M., Weisskoff R. M., Chesler D. A., Kwong K. K., Bogdanov A. A., Mandeville J. B., and Rosen B. R. "Improving MR quantification of regional blood volume with intravascular T1 contrast agents: Accuracy, precision, and water exchange." In: *Magnetic Resonance in Medicine* 36.6 (Dec. 1996), pp. 858–867. DOI: 10.1002/mrm.1910360608 (cit. on p. 18).

[110] Donahue K. M., Weisskoff R. M., and Burstein D. "Water diffusion and exchange as they influence contrast enhancement." In: *J. Magn. Reson. Imaging* 7.1 (Jan. 1997), pp. 102–110. DOI: 10.1002/jmri.1880070114 (cit. on p. 18).

[111] Yankeelov T. E., Rooney W. D., Li X., and Springer C. S. "Variation of the relaxographic "shutter-speed" for transcytolemmal water exchange affects the CR bolus-tracking curve shape." In: *Magn Reson Med* 50.6 (Dec. 2003), pp. 1151–1169. DOI: 10.1002/mrm.10624 (cit. on p. 19).

[112] Li X., Rooney W. D., and Springer C. S. "A unified magnetic resonance imaging pharmacokinetic theory: intravascular and extracellular contrast reagents." In: *Magn Reson Med* 54.6 (Dec. 2005), pp. 1351–1359. DOI: 10.1002/mrm.20684 (cit. on p. 19).

[113] Zhou R., Pickup S., Yankeelov T. E., Springer C. S., and Glickson J. D. "Simultaneous measurement of arterial input function and tumor pharmacokinetics in mice by dynamic contrast enhanced imaging: Effects of transcytolemmal water exchange." In: *Magnetic Resonance in Medicine* 52.2 (2004), pp. 248–257. DOI: 10.1002/mrm.20143 (cit. on p. 19).

[114] Labadie C., Lee J., Vetek G., and Springer C. "Relaxographic Imaging." In: *Journal of Magnetic Resonance, Series B* 105.2 (Oct. 1994), pp. 99–112. DOI: 10.1006/jmrb.1994.1109 (cit. on p. 19).

[115] Strijkers G. J., Hak S., Kok M. B., Springer C. S., and Nicolay K. "Three-compartment T1 relaxation model for intracellular paramagnetic contrast agents." In: *Magn Reson Med* 61.5 (May 2009), pp. 1049–1058. DOI: 10.1002/mrm.21919 (cit. on p. 19).

[116] Lüsse S., Claassen H., Gehrke T., Hassenpflug J., Schünke M., Heller M., and Glüer C. C. "Evaluation of water content by spatially resolved transverse relaxation times of human articular cartilage." In: *Magnetic resonance imaging* 18 (4 May 2000), pp. 423–430. DOI: 10.1016/s0730-725x(99)00144-7 (cit. on p. 20).

[117] Bansal R., Hao X., Liu F., Xu D., Liu J., and Peterson B. S. "The effects of changing water content, relaxation times, and tissue contrast on tissue segmentation and measures of cortical anatomy in MR images." In: *Magnetic resonance imaging* 31 (10 Dec. 2013), pp. 1709–1730. DOI: 10.1016/j.mri.2013.07.017 (cit. on p. 20).

[118] Fragonas E., Mlynárik V., Jellús V., Micali F., Piras A., Toffanin R., Rizzo R., and Vittur F. "Correlation between biochemical composition and magnetic resonance appearance of articular cartilage." In: *Osteoarthritis and cartilage* 6 (1 Jan. 1998), pp. 24–32. DOI: 10.1053/joca.1997.0089 (cit. on p. 20).

[119] Menezes N. M., Gray M. L., Hartke J. R., and Burstein D. "T2 and T1rho MRI in articular cartilage systems." In: *Magnetic resonance in medicine* 51 (3 Mar. 2004), pp. 503–509. DOI: 10.1002/mrm.10710 (cit. on p. 20).

[120] Henkelman R. M., Stanisz G. J., Kim J. K., and Bronskill M. J. "Anisotropy of NMR properties of tissues." In: *Magnetic resonance in medicine* 32 (5 Nov. 1994), pp. 592–601. DOI: 10.1002/mrm.1910320508 (cit. on p. 20).

[121] Stahl R., Blumenkrantz G., Carballido-Gamio J., Zhao S., Munoz T., Hellio Le Graverand-Gastineau M. P., Li X., Majumdar S., and Link T. M. "MRI-derived T2 relaxation times and cartilage morphometry of the tibio-femoral joint in subjects with and without osteoarthritis during a 1-year follow-up." In: *Osteoarthritis and cartilage* 15 (11 Nov. 2007), pp. 1225–1234. DOI: 10.1016/j.joca.2007.04.018 (cit. on p. 20).

[122] Jayasundar R., Ayyar S., and Raghunathan R. "Proton resonance imaging and relaxation in raw and cooked hen eggs." In: *Magnetic resonance imaging* 15 (6 1997), pp. 709–717. DOI: 10.1016/S0730-725X(97)00010-6 (cit. on p. 20).

[123] Stanisz G. J., Odrobina E. E., Pun J., Escaravage M., Graham S. J., Bronskill M. J., and Henkelman R. M. "T1, T2 relaxation and magnetization transfer in tissue at 3T." In: *Magnetic resonance in medicine* 54 (3 Sept. 2005), pp. 507–512. DOI: 10.1002/mrm.20605 (cit. on p. 21).

[124] Bradley W. and Schmidt P. "Effect of methemoglobin formation on the MR appearance of subarachnoid hemorrhage." In: *Radiology* 156.1 (Jan. 1985), pp. 99–103 (cit. on pp. 21, 69).

[125] Bradley W. G. "MR appearance of hemorrhage in the brain." In: *Radiology* 189.1 (Oct. 1993), pp. 15–26. DOI: 10.1148/radiology.189.1.8372185 (cit. on pp. 21, 69).

[126] Clark R. A., Watanabe A. T., Bradley W. G., and Roberts J. D. "Acute hematomas: effects of deoxygenation, hematocrit, and fibrin-clot formation and retraction on T2 shortening." In: *Radiology* 175.1 (Jan. 1990), pp. 201–206. DOI: 10.1148/radiology.175.1.2315481 (cit. on p. 21).

[127] Silvennoinen M., Kettunen M., and Kauppinen R. "Effects of hematocrit and oxygen saturation level on blood spin-lattice relaxation." In: *Magnetic Resonance in Medicine* 49.3 (Mar. 2003), pp. 568–571. DOI: 10.1002/mrm.10370 (cit. on p. 21).

[128] Chen J. J. and Pike G. B. "Human whole blood T2 relaxometry at 3 Tesla." In: *Magnetic Resonance in Medicine* 61.2 (Feb. 2009), pp. 249–254. DOI: 10.1002/mrm.21858 (cit. on p. 21).

[129] Petrovic A., Krauskopf A., Hassler E., Stollberger R., and Scheurer E. "Time related changes of T1, T2, and T2(*)(2) of human blood in vitro." In: *Forensic science international* 262 (May 2016), pp. 11–17. DOI: 10.1016/j.forsciint.2016.02.032 (cit. on p. 21).

[130] Greulich W. W. and Pyle S. I. "Radiographic atlas of skeletal development of the hand and wrist." In: *Am J Med Sci* 238.3 (1959), p. 393 (cit. on pp. 21, 57).

[131] Tanner J. M. *A history of the study of human growth*. Cambridge University Press, 1981 (cit. on p. 21).

[132] Tanner J. M., Whitehouse R. H., Cameron N., Marshall W. A., and Healy M. J. R. *Assessment of Skeletal Maturity and Prediction of Adult Height (TW2 Method)*. Academic Press, 1983 (cit. on p. 21).

[133] Urschler M., Grassegger S., and Štern D. "What automated age estimation of hand and wrist MRI data tells us about skeletal maturation in male adolescents." In: *Ann Hum Biol* 42.4 (July 2015), pp. 358–367. DOI: 10.3109/03014460.2015.1043945 (cit. on pp. 21, 57).

[134] Urschler M., Krauskopf A., Widek T., Sorantin E., Ehammer T., Borkenstein M., Yen K., and Scheurer E. "Applicability of Greulich–Pyle and Tanner–Whitehouse grading methods to MRI when assessing hand bone age in forensic age estimation: A pilot study." In: *Forensic Sci Intl* 266 (Sept. 2016), pp. 281–288. DOI: 10.1016/j.forsciint.2016.06.016 (cit. on p. 21).

[135] Štern D., Ebner T., Bischof H., Grassegger S., Ehammer T., and Urschler M. "Fully Automatic Bone Age Estimation from Left Hand MR Images." In: *Med Image Comput Comput Assist Interv* (2014), pp. 220–227. DOI: 10.1007/978-3-319-10470-6_28 (cit. on p. 21).

[136] Štern D., Ebner T., and Urschler M. "From Local to Global Random Regression Forests: Exploring Anatomical Landmark Localization." In: *Med Image Comput Comput Assist Interv* (2016). Ed. by Ourselin S., Joskowicz L., Sabuncu M. R., Unal G., and Wells W., pp. 221–229. DOI: 10.1007/978-3-319-46723-8_26 (cit. on p. 21).

[137] Štern D., Payer C., Lepetit V., and Urschler M. "Automated Age Estimation from Hand MRI Volumes Using Deep Learning." In: *Med Image Comput Comput Assist Interv* (2016). Ed. by Ourselin S., Joskowicz L., Sabuncu M. R., Unal G., and Wells W., pp. 194–202. DOI: 10.1007/978-3-319-46723-8_23 (cit. on p. 21).

[138] Piney A. "The anatomy of the bone marrow: with special reference to the distribution of the red marrow." In: *The British Medical Journal* 2.3226 (1922), pp. 792–795 (cit. on pp. 21, 47).

[139] Okada Y., Aoki S., Barkovich A. J., Nishimura K., Norman D., Kjos B. O., and Brasch R. C. "Cranial bone marrow in children: assessment of normal development with MR imaging." In: *Radiology* 171.1 (1989), pp. 161–164. DOI: 10.1148/radiology.171.1.2928520 (cit. on pp. 21, 47).

[140] Moore S. G. and Dawson K. L. "Red and yellow marrow in the femur: age-related changes in appearance at MR imaging." In: *Radiology* 175.1 (1990), pp. 219–223. DOI: 10.1148/radiology.175.1.2315484 (cit. on pp. 21, 47).

[141] Ricci C., Cova M., Kang Y. S., Yang A., Rahmouni A., Scott W., and Zerhouni E. "Normal age-related patterns of cellular and fatty bone marrow distribution in the axial skeleton: MR imaging study." In: *Radiology* 177.1 (1990), pp. 83–88. DOI: 10.1148/radiology.177.1.2399343 (cit. on pp. 21, 47).

[142] Jaramillo D., Laor T., Hoffer F. A., Zaleske D. J., Cleveland R., Buchbinder B. R., and Egglin T. K. "Epiphyseal marrow in infancy: MR imaging." In: *Radiology* 180.3 (1991), pp. 809–812. DOI: 10.1148/radiology.180.3.1871298 (cit. on pp. 21, 47).

[143] Dawson K. L., Moore S. G., and Rowland J. M. "Age-related marrow changes in the pelvis: MR and anatomic findings." In: *Radiology* 183.1 (1992), pp. 47–51. DOI: 10.1148/radiology.183.1.1549693 (cit. on pp. 21, 47).

[144] Koo K.-H., Dussault R., Kaplan P., Kim R., Ahn I.-O., Christopher J., Song H.-R., and Wang G.-J. "Age-related marrow conversion in the proximal metaphysis of the femur: evaluation with T1-weighted MR imaging." In: *Radiology* 206.3 (1998), pp. 745–748. DOI: 10.1148/radiology.206.3.9494495 (cit. on p. 21).

[145] Schellinger D., Lin C. S., Fertikh D., Lee J. S., Lauerman W. C., Henderson F., and Davis B. "Normal lumbar vertebrae: anatomic, age, and sex variance in subjects at proton MR spectroscopy–initial experience." In: *Radiology* 215.3 (2000), pp. 910–6. DOI: 10.1148/radiology.215.3.r00jn42910 (cit. on pp. 21, 47).

[146] Kugel H., Jung C., Schulte O., and Heindel W. "Age- and sex-specific differences in the 1H-spectrum of vertebral bone marrow." In: *J Magn Reson Imaging* 13.2 (2001), pp. 263–8. DOI: 10.1002/1522-2586(200102)13:2<263::AID-JMRI1038>3.0.CO;2-M (cit. on pp. 21, 47).

[147] Li B., Beveridge P., O'Hare W. T., and Islam M. "The estimation of the age of a blood stain using reflectance spectroscopy with a microspectrophotometer, spectral pre-processing and linear discriminant analysis." In: *Forensic Science International* 212 (July 2011), pp. 198–204. DOI: 10.1016/j.forsciint.2011.05.031 (cit. on pp. 21, 25).

[148] Roldan-Valadez E., Piña-Jimenez C., Favila R., and Rios C. "Gender and age groups interactions in the quantification of bone marrow fat content in lumbar spine using 3T MR spectroscopy: A multivariate analysis of covariance (Mancova)." In: *European journal of radiology* (2013). DOI: 10.1016/j.ejrad.2013.07.012 (cit. on pp. 21, 47).

[149] Neumayer B., Hassler E., Petrovic A., Widek T., Ogris K., and Scheurer E. "Age Determination of Soft Tissue Hematomas." In: *NMR Biomed.* 27.11 (Sept. 2014), pp. 1397–1402. DOI: 10.1002/nbm.3202 (cit. on p. 25).

[150] Langlois N. and Gresham G. "The ageing of bruises: A review and study of the colour changes with time." In: *Forensic Science International* 50.2 (Sept. 1991), pp. 227–238. DOI: 10.1016/0379-0738(91)90154-B (cit. on p. 25).

[151] Stephenson T. and Bialas Y. "Estimation of the age of bruising." In: *Archives of Disease in Childhood* 74.1 (Jan. 1996), pp. 53–55. DOI: 10.1136/adc.74.1.53 (cit. on p. 25).

[152] Pilling M., Vanezis P., Perrett D., and Johnston A. "Visual assessment of the timing of bruising by forensic experts." In: *Journal of Forensic and Legal Medicine* 17.3 (Apr. 2010), pp. 143–149. DOI: 10.1016/j.jflm.2009.10.002 (cit. on p. 25).

[153] Grossman S. E., Johnston A., Vanezis P., and Perrett D. "Can we assess the age of bruises? An attempt to develop an objective technique." In: *Medicine, Science and the Law* 51.3 (July 2011), pp. 170–176. DOI: 10.1258/msl.2011.010135 (cit. on p. 25).

[154] Hughes V., Ellis P., and Langlois N. "The perception of yellow in bruises." In: *Journal of Clinical Forensic Medicine* 11.5 (Oct. 2004), pp. 257–259. DOI: 10.1016/j.jcfm.2004.01.007 (cit. on p. 25).

[155] Hughes V. K. "The practical application of reflectance spectrophotometry for the demonstration of haemoglobin and its degradation in bruises." In: *Journal of Clinical Pathology* 57.4 (Apr. 2004), pp. 355–359. DOI: 10.1136/jcp.2003.011445 (cit. on p. 25).

[156] Randeberg L. L., Haugen O. A., Haaverstad R., and Svaasand L. O. "A novel approach to age determination of traumatic injuries by reflectance spectroscopy." In: *Lasers in Surgery and Medicine* 38.4 (Apr. 2006), pp. 277–289. DOI: 10.1002/lsm.20301 (cit. on p. 25).

[157] Yajima Y. and Funayama M. "Spectrophotometric and tristimulus analysis of the colors of subcutaneous bleeding in living persons." In: *Forensic Science International* 156 (Jan. 2006), pp. 131–137. DOI: 10.1016/j.forsciint.2003.09.022 (cit. on p. 25).

[158] Hassler E. M., Ogris K., Petrovic A., Neumayer B., Widek T., Yen K., and Scheurer E. "Contrast of artificial subcutaneous hematomas in MRI over time." In: *Int J Legal Med* 129.2 (Nov. 2014), pp. 317–324. DOI: 10.1007/s00414-014-1124-8 (cit. on p. 26).

[159] Aitken A. P. and Magill H. K. "Fractures involving the distal femoral epiphyseal cartilage." In: *J Bone Joint Surg Am* 34-A.1 (Jan. 1952), pp. 96–108 (cit. on p. 33).

[160] Navascués J. A., González-López J. L., López-Valverde S., Soleto J., Rodriguez-Durantez J. A., and García-Trevijano J. L. "Premature physeal closure after tibial diaphyseal fractures in adolescents." In: *J Pediatr Orthop* 20.2 (2000), pp. 193–196 (cit. on p. 33).

[161] Weinberg A. and Tscherne H. *Tscherne Unfallchirurgie: Unfallchirurgie im Kindesalter - Teil 1: Allgemeiner Teil, Kopf, Obere Extremität*. Springer, 2006 (cit. on p. 33).

[162] Fischerauer E., Heidari N., Neumayer B., Deutsch A., and Weinberg A. M. "The spatial and temporal expression of VEGF and its receptors 1 and 2 in post-traumatic bone bridge formation of the growth plate." In: *Journal of Molecular Histology* 42.6 (Sept. 2011), pp. 513–522. DOI: 10.1007/s10735-011-9359-x (cit. on p. 34).

[163] Baron K., Neumayer B., Amerstorfer E., Scheurer E., Diwoky C., Stollberger R., Sprenger H., and Weinberg A. M. "Time-Dependent Changes in T1 during Fracture Healing in Juvenile Rats: A Quantitative MR Approach." In: *PLOS ONE* 11.11 (Nov. 2016). Ed. by Wallace J. M., e0164284. DOI: 10.1371/journal.pone.0164284 (cit. on p. 34).

[164] Neumayer B., Widek T., Stollberger R., and Scheurer E. "Reproducibility of Relaxometry of Human Lumbar Vertebrae at 3 Tesla Using $^{1}$H MR Spectroscopy." In: *Journal of Magnetic Resonance Imaging* (Dec. 2017). DOI: 10.1002/jmri.25912 (cit. on p. 47).

[165] Li X., Kuo D., Schafer A. L., Porzig A., Link T. M., Black D., and Schwartz A. V. "Quantification of vertebral bone marrow fat content using 3 Tesla MR spectroscopy: reproducibility, vertebral variation, and applications in osteoporosis." In: *Journal of Magnetic Resonance Imaging* 33.4 (2011), pp. 974–979. DOI: 10.1002/jmri.22489 (cit. on p. 47).

[166] Shih T. T., Chang C., Hsu C., Wei S., Su K., and Chung H. "Correlation of bone marrow lipid water content with bone mineral density on the lumbar spine." In: *Spine (Phila Pa 1976)* 29.24 (2004), pp. 2844–50. DOI: 10.1097/01.brs.0000147803.01224.5b (cit. on pp. 47, 71).

[167] Yeung D. K. W., Griffith J. F., Antonio G. E., Lee F. K. H., Woo J., and Leung P. C. "Osteoporosis is associated with increased marrow fat content and decreased marrow fat unsaturation: a proton MR spectroscopy study." In: *J Magn Reson Imaging* 22.2 (2005), pp. 279–85. DOI: 10.1002/jmri.20367 (cit. on pp. 47, 71).

[168] Baum T., Yap S. P., Karampinos D. C., Nardo L., Kuo D., Burghardt A. J., Masharani U. B., Schwartz A. V., Li X., and Link T. M. "Does vertebral bone marrow fat content correlate with abdominal adipose tissue, lumbar spine bone mineral density, and blood biomarkers in women with type 2 diabetes mellitus?" In: *Journal of Magnetic Resonance Imaging* 35.1 (2012), pp. 117–124. DOI: 10.1002/jmri.22757 (cit. on pp. 47, 71).

[169] Neumayer B., Hassler E., Widek T., Ogris K., and Scheurer E. "Age Estimation of Soft Tissue Hematomas." In: *Proceedings of the International Society for Magnetic Resonance in Medicine*. Apr. 2013, p. 2499 (cit. on p. 47).

[170] Neumayer B., Schlögl M., Payer C., Widek T., Tschauner S., Ehammer T., Stollberger R., and Urschler M. "Reducing Acquisition Time for MRI-Based Forensic Age Estimation." In: *Scientific Reports* (2018). DOI: 10.1038/s41598-018-20475-1 (cit. on p. 57).

[171] Martin D. D., Wit J. M., Hochberg Z., Sävendahl L., van Rijn R. R., Fricke O., Cameron N., Caliebe J., Hertel T., Kiepe D., Albertsson-Wikland K., Thodberg H. H., Binder G., and Ranke M. B. "The use of bone age in clinical practice – part 1." In: *Horm Res Paediatr* 76.1 (2011), pp. 1–9. DOI: 10.1159/000329372 (cit. on p. 57).

[172] Lee S. C., Shim J. S., Seo S. W., Lim K. S., and Ko K. R. "The accuracy of current methods in determining the timing of epiphysiodesis." In: *Bone Joint J* 95-B.7 (July 2013), pp. 993–1000. DOI: 10.1302/0301-620X.95B7.30803 (cit. on p. 57).

[173] Wang W. W. J., Xia C. W., Zhu F., Zhu Z. Z., Wang B., Wang S. F., Yeung B. H. Y., Lee S. K. M., Cheng J. C. Y., and Qiu Y. "Correlation of Risser sign, radiographs of hand and wrist with the histological grade of iliac crest apophysis in girls with adolescent idiopathic scoliosis." In: *Spine (Phila Pa 1976)* 34.17 (Aug. 2009), pp. 1849–1854. DOI: 10.1097/BRS.0b013e3181ab358c (cit. on p. 57).

[174] Schmeling A., Geserick G., Reisinger W., and Olze A. "Age estimation." In: *Forensic Sci Intl* 165.2-3 (Jan. 2007), pp. 178–181. DOI: 10.1016/j.forsciint.2006.05.016 (cit. on p. 57).

[175] Dvorak J., George J., Junge A., and Hodler J. "Age determination by magnetic resonance imaging of the wrist in adolescent male football players." In: *Br J Sports Med* 41.1 (2007), pp. 45–52. DOI: 10.1136/bjsm.2006.031021 (cit. on p. 57).

[176] George J., Nagendran J., and Azmi K. "Comparison study of growth plate fusion using MRI versus plain radiographs as used in age determination for exclusion of overaged football players." In: *Br J Sports Med* 46.4 (Dec. 2012), pp. 273–278. DOI: 10.1136/bjsm.2010.074948 (cit. on p. 57).

[177] Vieth V., Schulz R., Brinkmeier P., Dvorak J., and Schmeling A. "Age estimation in U-20 football players using 3.0 Tesla MRI of the clavicle." In: *Forensic Sci Intl* 241 (Aug. 2014), pp. 118–122. DOI: 10.1016/j.forsciint.2014.05.008 (cit. on p. 57).

[178] Schmeling A., Grundmann C., Fuhrmann A., Kaatsch H.-J., Knell B., Ramsthaler F., Reisinger W., Riepert T., Ritz-Timme S., Rösing F., Rötzscher K., and Geserick G. "Updated recommendations of the Study Group on Forensic Age Diagnostics for age estimation in the living in criminal proceedings." In: *Rechtsmedizin* 18.6 (2008), pp. 451–453. DOI: 10.1007/s00194-008-0571-2 (cit. on p. 57).

[179] Hillewig E., Degroote J., Van der Paelt T., Visscher A., Vandemaele P., Lutin B., D'Hooghe L., Vandriessche V., Piette M., and Verstraete K. "Magnetic resonance imaging of the sternal extremity of the clavicle in forensic age estimation: towards more sound age estimates." In:

*Int J Legal Med* 127.3 (Dec. 2012), pp. 677–689. DOI: 10.1007/s00414-012-0798-z (cit. on p. 57).

[180] Dedouit F., Auriol J., Rousseau H., Rouge D., Crubézy E., and Telmon N. "Age assessment by magnetic resonance imaging of the knee: A preliminary study." In: *Forensic Sci Intl* 217.1–3 (2012), 232.e1–232.e7. DOI: 10.1016/j.forsciint.2011.11.013 (cit. on p. 57).

[181] Terada Y., Kono S., Tamada D., Uchiumi T., Kose K., Miyagi R., Yamabe E., and Yoshioka H. "Skeletal age assessment in children using an open compact MRI system." In: *Magn Reson Med* 69.6 (2013), pp. 1697–1702. DOI: 10.1002/mrm.24439 (cit. on p. 57).

[182] Tomei E., Sartori A., Nissman D., Al Ansari N., Battisti S., Rubini A., Stagnitti A., Martino M., Marini M., Barbato E., and al. et. "Value of MRI of the hand and the wrist in evaluation of bone age: Preliminary results." In: *J Magn Reson Imaging* 39.5 (Nov. 2013), pp. 1198–1205. DOI: 10.1002/jmri.24286 (cit. on p. 57).

[183] Serinelli S., Panebianco V., Martino M., Battisti S., Rodacki K., Marinelli E., Zaccagna F., Semelka R. C., and Tomei E. "Accuracy of MRI skeletal age estimation for subjects 12–19. Potential use for subjects of unknown age." In: *Int J Legal Med* 129.3 (Feb. 2015), pp. 609–617. DOI: 10.1007/s00414-015-1161-y (cit. on p. 57).

[184] Baumann P., Widek T., Merkens H., Boldt J., Petrovic A., Urschler M., Kirnbauer B., Jakse N., and Scheurer E. "Dental age estimation of living persons: Comparison of MRI with OPG." In: *Forensic Sci Intl* 253 (Aug. 2015), pp. 76–80. DOI: 10.1016/j.forsciint.2015.06.001 (cit. on p. 57).

[185] Gelbrich B., Frerking C., Schwerdt S. W. S., Stellzig-Eisenhauer A., Tausche E., and Gelbrich G. "Combining wrist age and third molars in forensic age estimation: how to calculate the joint age estimate and its error rate in age diagnostics." In: *Ann Hum Biol* 42.4 (2015). PMID: 26079219, pp. 389–396. DOI: 10.3109/03014460.2015.1046487 (cit. on p. 57).

[186] Bredies K., Kunisch K., and Pock T. "Total generalized variation." In: *SIAM J Imaging Sci* 3.3 (2010), pp. 492–526. DOI: 10.1137/090769521 (cit. on p. 57).

[187] Knoll F., Bredies K., Pock T., and Stollberger R. "Second order total generalized variation (TGV) for MRI." In: *Magn Reson Med* 65.2 (Dec. 2010), pp. 480–491. DOI: 10.1002/mrm.22595 (cit. on p. 57).

[188] Biomarkers Definitions Working Group. "Biomarkers and surrogate endpoints: Preferred definitions and conceptual framework." In: *Clinical Pharmacology & Therapeutics* 69.3 (Mar. 2001), pp. 89–95. DOI: 10.1067/mcp.2001.113989 (cit. on p. 69).

[189] Strimbu K. and Tavel J. A. "What are biomarkers?" In: *Current Opinion in HIV and AIDS* 5.6 (Nov. 2010), pp. 463–466. DOI: 10.1097/coh.0b013e32833ed177 (cit. on p. 69).

[190] Mayeux R. "Biomarkers: Potential uses and limitations." In: *NeuroRx* 1.2 (Apr. 2004), pp. 182–188. DOI: 10.1602/neurorx.1.2.182 (cit. on p. 69).

[191] Hu H. H. and Nayak K. S. "Change in the proton T1of fat and water in mixture." In: *Magnetic Resonance in Medicine* 63.2 (Feb. 2010), pp. 494–501. DOI: 10.1002/mrm.22205 (cit. on pp. 70, 71).

[192] Jaramillo D., Shapiro F., Hoffer F. A., Winalski C. S., Koskinen M. F., Frasso R., and Johnson A. "Posttraumatic growth-plate abnormalities: MR imaging of bony-bridge formation in rabbits." In: *Radiology* 175.3 (June 1990), pp. 767–773. DOI: 10.1148/radiology.175.3.2343128 (cit. on p. 71).

[193] Jaramillo D., Laor T., and Zaleske D. J. "Indirect trauma to the growth plate: results of MR imaging after epiphyseal and metaphyseal injury in rabbits." In: *Radiology* 187.1 (Apr. 1993), pp. 171–178. DOI: 10.1148/radiology.187.1.8451408 (cit. on p. 71).

[194] Bredella M. A., Daley S. M., Kalra M. K., Brown J. K., Miller K. K., and Torriani M. "Marrow Adipose Tissue Quantification of the Lumbar Spine by Using Dual-Energy CT and Single-Voxel 1H MR Spectroscopy: A Feasibility Study." In: *Radiology* 277.1 (Oct. 2015), pp. 230–235. DOI: 10.1148/radiol.2015142876 (cit. on p. 71).

[195] Terada Y., Tamada D., Kose K., Nozaki T., Kaneko Y., Miyagi R., and Yoshioka H. "Acceleration of skeletal age MR examination using compressed sensing." In: *Journal of Magnetic Resonance Imaging* 44.1 (Dec. 2015), pp. 204–211. DOI: 10.1002/jmri.25140 (cit. on p. 71).

[196] Hamilton G., Middleton M. S., Bydder M., Yokoo T., Schwimmer J. B., Kono Y., Patton H. M., Lavine J. E., and Sirlin C. B. "Effect of PRESS and STEAM sequences on magnetic resonance spectroscopic liver fat quantification." In: *Journal of Magnetic Resonance Imaging* 30.1 (2009), pp. 145–152. DOI: 10.1002/jmri.21809 (cit. on p. 72).

# List of Publications

## Refereed Journal Publications


**Neumayer, B.**, Schloegl, M., Payer, C., Widek, T., Tschauner, S., Ehammer, T., Stollberger, R., Urschler, M., "Reducing acquisition time for MRI-based forensic age estimation." In: *Scientific Reports* 8.1 (Feb. 2018), p. 2063. DOI: 10.1038/s41598-018-20475-1.

**Neumayer, B.**, Widek, T., Stollberger, R., Scheurer, E., "Reproducibility of Relaxometry of Human Lumbar Vertebrae at 3 Tesla Using $^{1}$H MR Spectroscopy." In: *Journal of Magnetic Resonance Imaging* (Dec. 2017). DOI: 10.1002/jmri.25912.

**Neumayer, B.**, Amerstorfer, E., Diwoky, C., Lindtner, R. A., Wadl, E., Scheurer, E., Weinberg, A.-M., Stollberger, R., "Assessment of Pharmacokinetics for Microvessel Proliferation by DCE-MRI for Early Detection of Physeal Bone Bridge Formation in an Animal Model." In: *Magnetic Resonance Materials in Physics, Biology and Medicine* 30.5 (Oct. 2017), pp. 417–427. DOI: 10.1007/s10334-017-0615-2.

Martínez Vera, N. P., Höller, J., Widek, T., **Neumayer, B.**, Ehammer, T., Urschler, M., "Forensic age estimation by morphometric analysis of the manubrium from 3D MR images." In: *Forensic Science International* 277 (Aug. 2017), pp. 21–29. DOI: 10.1016/j.forsciint.2017.05.005.

Baron, K., **Neumayer, B.**, Amerstorfer, E., Scheurer, E., Diwoky, C., Stollberger, R., Sprenger, H., Weinberg, A. M., "Time-Dependent Changes in T1 during Fracture Healing in Juvenile Rats: A Quantitative MR Approach." In: *PLOS ONE* 11.11 (Nov. 2016). Ed. by Wallace J. M., e0164284. DOI: 10.1371/journal.pone.0164284.

Webb, B., Widek, T., **Neumayer, B.**, Bruguier, C., Scheicher, S., Sprenger, H., Grabherr, S., Schwark, T., Stollberger, R., "Temperature dependence of viscosity, relaxation times (T1, T2) and simulated contrast for potential perfusates in post-mortem MR angiography (PMMRA)." In: *International Journal of Legal Medicine* (Nov. 2016). DOI: 10.1007/s00414-016-1482-5.

Baron, K., **Neumayer, B.**, Widek, T., Schick, F., Scheicher, S., Hassler, E., Scheurer, E., "Quantitative MR Imaging in Fracture Dating – Initial Results." In: *Forensic Science International* 261.Supplement C (Apr. 2016), pp. 61–69. DOI: 10.1016/j.forsciint.2016.01.020.

Diwoky, C., Liebmann, D., **Neumayer, B.**, Reinisch, A., Knoll, F., Strunk, D., Stollberger, R., "Positive contrast of SPIO-labeled cells by off-resonant reconstruction of 3D radial half-echo bSSFP." In: *NMR in Biomedicine* 28.1 (Jan. 2015), pp. 79–88. DOI: 10.1002/nbm.3229.

Hassler, E. M., Ogris, K., Petrovic, A., **Neumayer, B.**, Widek, T., Yen, K., Scheurer, E., "Contrast of artificial subcutaneous hematomas in MRI over time." In: *Int J Legal Med* 129.2 (Nov. 2014), pp. 317–324. DOI: 10.1007/s00414-014-1124-8.

**Neumayer, B.**, Hassler, E., Petrovic, A., Widek, T., Ogris, K., Scheurer, E., "Age determination of soft tissue hematomas." In: *NMR Biomed.* 27.11 (Sept. 2014), pp. 1397–1402. DOI: 10.1002/nbm.3202.

Storck, C., Gehrer, R., Hofer, M., **Neumayer, B.**, Stollberger, R., Schumacher, R., Gugatschka, M., Friedrich, G., Wolfensberger, M., "Laryngeal Electromyography: Electrode Guidance Based on 3-Dimensional Magnetic Resonance Tomography Images of the Larynx." In: *Journal of Voice* 26.1 (Jan. 2012), pp. 110–116. DOI: 10.1016/j.jvoice.2010.09.002.

Fischerauer, E., Heidari, N., **Neumayer, B.**, Deutsch, A., Weinberg, A. M., "The spatial and temporal expression of VEGF and its receptors 1 and 2 in post-traumatic bone bridge formation of the growth plate." In: *Journal of Molecular Histology* 42.6 (Sept. 2011), pp. 513–522. DOI: 10.1007/s10735-011-9359-x.

## Refereed Conference Proceedings

**Neumayer, B.**, Schlögl, M., Payer, C., Widek, T., Ehammer, T., Stollberger, R., Urschler, M., "Accuracy of Age Estimation based on Undersampled MR Images of the Hand." In: *Proceedings of the International Society for Magnetic Resonance in Medicine*. 2017.

**Neumayer, B.**, Widek, T., Boesch, C., Scheurer, E., "Reproducibility for MRS-Based Relaxometry and Identification of Influential Parameters." In: *Proceedings of the International Society for Magnetic Resonance in Medicine*. 2017.

Webb, B., Urschler, M., Leoni, M., **Neumayer, B.**, Widek, T., Scheicher, S., Stollberger, R., Schwark, T., "Cause of death or caused by death: Differentiation of thromboemboli and post-mortem clots using quantitative MRI." In: *Proceedings of the International Society for Magnetic Resonance in Medicine*. 2017.

Baron, K., Widek, T., Sprenger, H., **Neumayer, B.**, Hofer, H., Scheurer, E., "Influences on fracture healing of long bones analysed by qMRI." In: *Proceedings of the 33rd Annual Scientific Meeting ESMRMB*. Oct. 2016, pp. 389–390.

Martinez Vera, N. P., Hoeller, J., **Neumayer, B.**, Widek, T., Ehammer, T., Urschler, M., "Skeletal age estimation using shape variations of the manubrium in MR images." In: *Proceedings of the 33rd Annual Scientific Meeting ESMRMB*. Sept. 2016, pp. 324–325.

Webb, B., Widek, T., **Neumayer, B.**, Stollberger, R., Schwark, T., "Post-mortem reperfusion of the vascular system and examination in MRI: Temperature-dependent characterisation of perfusates and contrast simulations." In: *Proceedings of the International Society for Magnetic Resonance in Medicine*. May 2016.

Martinez Vera, N. P., **Neumayer, B.**, Widek, T., Grassegger, S., Scheurer, E., Urschler, M., "Bone age determination from adolescence to young adulthood by investigating the sternoclavicular joint in MRI." In: *Proceedings of the 32nd Annual Scientific Meeting ESMRMB*. Oct. 2015, p. 235.

Widek, T., Hassler, E., Petrovic, A., **Neumayer, B.**, Ogris, K., Scheurer, E., "Analysis of possible impact factors on the regeneration of hematomas in the subcutaneous fatty tissue." In: *Proceedings of the 32nd Annual Scientific Meeting ESMRMB*. Oct. 2015, p. 434.

Baron, K., **Neumayer, B.**, Widek, T., Scheicher, S., Hassler, E. M., Schick, F., Scheurer, E., "Musculoskeletal MR-Imaging in Fracture Dating." In: *Proceedings of the International Society for Magnetic Resonance in Medicine*. June 2015.

Martinez Vera, N. P., Höller, J., **Neumayer, B.**, Widek, T., Grassegger, S., Ehammer, T., Scheurer, E., Urschler, M., "Age estimation in adolescents and young adults using MRI data of the manubrium." In: *Proceedings of the International Society for Magnetic Resonance in Medicine*. June 2015.

**Neumayer, B.**, Petrovic, A., Widek, T., Boesch, C., Scheurer, E., "Reproducibility of $^{1}$H MR Spectroscopy of Human Lumbar Vertebrae at 3 Tesla." In: *Proceedings of the 30th Annual Scientific Meeting ESMRMB*. Oct. 2013, p. 472.

Storck, C., Hofer, M., **Neumayer, B.**, Stollberger, R., Gogos, B., "The closure of the posterior glottis: true or a geometric condition?" In: *Proceedings of the 10th Pan European Voice Conference PEVOC*. Aug. 2013, p. 18.

**Neumayer, B.**, Hassler, E., Widek, T., Ogris, K., Scheurer, E., "Age Estimation of Soft Tissue Hematomas." In: *Proceedings of the International Society for Magnetic Resonance in Medicine*. Apr. 2013, p. 2499.

Hassler, E., Petrovic, A., Widek, T., Ogris, K., **Neumayer, B.**, Scheurer, E., Yen, K., "Contrast of Artificial Subcutaneous Hematomas in Different MRI Sequences over Time." In: *Radiological Society of North America 2012 Scientific Assembly and Annual Meeting*. Nov. 2012.

**Neumayer, B.**, Hassler, E., Widek, T., Petrovic, A., Scheurer, E., "Modelling of Contrast Changes in Soft Tissue Hematomas." In: *Proceedings of the 29th Annual Scientific Meeting ESMRMB*. Oct. 2012, p. 481.

**Neumayer, B.**, Stollberger, R., "Bound Pool Fraction & $T_{1,free}$ Quantification by Non-Linear Parameter Identification of Composite Echoes." In: *Proceedings of the International Society for Magnetic Resonance in Medicine*. May 2011, p. 2783.

Diwoky, C., Reinisch, A., Knoll, F., **Neumayer, B.**, Strunk, D., Stollberger, R., "On Possible Pitfalls in Working on SPIO Labelled Cells with 2D UTE Sequences." In: *Proceedings of the International Society for Magnetic Resonance in Medicine*. Ed. by Magnetic Resonance in Medicine I. S. for. Stockholm, Apr. 2010, p. 1875.

**Neumayer, B.**, Diwoky, C., Reinisch, A., Strunk, D., Stollberger, R., "Quantification of Cell Density of SPIO-Labelled Cell Populations." In: *Proceedings of the International Society for Magnetic Resonance in Medicine*. Ed. by Magnetic Resonance in Medicine I. S. for. Stockholm, Apr. 2010, p. 4192.

Hofer, M., **Neumayer, B.**, Gugatschka, M., Juergens, P., Stollberger, R., Sorantin, E., Ebner, F., Friedrich, G., Storck, C., "High resolution MRI and CT investigation of laryngeal soft tissues and skeletal structures." In: *Proceedings of the International Society for Magnetic Resonance in Medicine*. Honolulu, Apr. 2009, p. 3509.

**Neumayer, B.**, Fischerauer, E. E., Diwoky, C., Weinberg, A.-M., Stollberger, R., "Examination of the Correlation between Hypervascularity and Physeal Bone Bridge Formation." In: *Proceedings of the International Society for Magnetic Resonance in Medicine*. Hawai'i, USA, Apr. 2009, p. 851.

Fischerauer, E., **Neumayer, B.**, Diwoky, C., Lindtner, R., Stollberger, R., Hoellwarth, M., Weinberg, A.-M., "Transphyseal lesion: Is hypervascularity associated with developing physeal bone bridges?" In: *21. International Symposium on Paediatric Surgical Research: Abstractbook*. Leipzig, Oct. 2008.

Diwoky, C., Reinisch, A., **Neumayer, B.**, Strunk, D., Stollberger, R., "High Sensitivity Positive-Contrast Imaging of Stem Cells in Bone Marrow." In: *Proceedings of World Molecular Imaging Congress (WMIC 2008)*. Sept. 2008.